UNIVERSIDADE D
COIMBRA

Gonçalo Conde Abrantes

Optimization of an Electric Vehicle Wireless Charging System using Artificial Intelligence Techniques

Master Thesis in Electrical and Computer Engineering, specialization in Power Control Systems, supervised by Professor Doctor Sérgio Manuel Ângelo da Cruz and co-supervised by Professor Doctor Marina Mendes Sargento Domingues Perdigão, presented to the Department of Electrical and Computer Engineering of the Faculty of Sciences and Technology of the University of Coimbra.

September 2023

FACULDADE DE
CIÊNCIAS E TECNOLOGIA
UNIVERSIDADE D
COIMBRA

Gonçalo Conde Abrantes

Optimization of an Electric Vehicle Wireless Charging System using Artificial Intelligence Techniques

Master Thesis in Electrical and Computer Engineering, specialization in Power Control Systems, supervised by Professor Doctor Sérgio Manuel Ângelo da Cruz and co-supervised by Professor Doctor Marina Mendes Sargento Domingues Perdigão, presented to the Department of Electrical and Computer Engineering of the Faculty of Sciences and Technology of the University of Coimbra.

September 2023

Acknowledgments

This master thesis represents the end of a long journey. A journey that in the first place, would not have been possible without the contribution and unwavering support of both my parents and my girlfriend, Vanessa Correia, who always believed in me and stood by my side through every moment.

The last five years were filled with many hours of hard work but also many special moments that I will carry with me along with the people that made part of them for the rest of my life. To those people I want to give a special thanks to my colleagues and friends Alexandre Wilson, Artur Oliveira, Bráulio Teles, Daniel Correia, Daniel Ferreira, Daniel Santos, João Silva, João Neves and Luís Maia.

One of the key pillars of my academic journey was undoubtedly my supervisor, Professor Doctor Sérgio Manuel Ângelo da Cruz to who I want to express my sincerest thanks, since without his support, guidance and valuable advice, the development of this research work would not have been concluded successfully.

Additionally, I would like to extend my gratitude to my host institution, DEEC-UC, and to Instituto de Telecomunicações and its members. In particular, I wish to thank Professor Doctor André Manuel dos Santos Mendes and Valter de Sousa Costa for all the given support. These acknowledgments also extend to my co-supervisor Professor Doctor Marina Mendes Sargento Domingues Perdigão who along with other members of the Instituto de Telecomunicações, initiated the project 2022.06192.PTDC funded by FCT, which provided the necessary conditions for carrying out this research work.

To everyone else whom I have not mentioned but who has also been a part of this path, my deepest thanks.

Abstract

The ability to transfer energy efficiently in wireless inductive charging systems hinges on the characterization of the mutual inductance between the transmitter and receiver coils. In the context of the charging of electric vehicles, this parameter is significantly influenced by the relative positioning of the vehicle and the transmitting coil. Hence, the precise determination of the mutual inductance yields various advantages, particularly in terms of optimization of the alignment between the vehicle and the transmitting coil, thereby improving the system efficiency. Within this framework, algorithms grounded in Artificial Intelligence techniques emerge as promising solutions.

This research work revolves around the estimation of the mutual inductance in a wireless inductive power transfer system using a series-series-series topology, implemented in Simulink. The system output represents a typical battery charger, ranging from 500 W to 3000 W, during the initial charging phase,i.e., when the battery is discharged. To estimate this parameter, an artificial neural network was developed and implemented. This document provides a comprehensive account of the entire process involved in the implementation of this artificial intelligence model, with particular focus on feature extraction from the analysed system and data normalization. Given the characteristics of the system, the feature selection process was guided by two essential criteria: significant variation with vehicle misalignment and no variation for different charging power levels.

Through the conducted analysis, it was determined that the most suitable variables for this purpose are the amplitudes of the harmonic components relative to the measured variables on the coil of the receiver side.

In the pursuit of creating a robust artificial intelligence model, efforts were directed at minimizing the size of the training dataset, utilizing only approximately 1% of the available data. The performance of the developed artificial neural network was evaluated in two distinct scenarios, depending on whether the training data was derived from signals with or without white noise. Upon the analysis of the results, it was verified that the largest estimation error observed was approximately 3%, occurring at a charging power of 500 W. Hence, it can be inferred that the proposed artificial neural network exhibits the capability to accurately estimate the value of mutual inductance in this type of system.

Keywords: Power electronics, inductive power transfer system, mutual inductance estimation, artificial intelligence, deep learning, artificial neural networks.

Resumo

A capacidade de transferência de energia nos sistemas de carregamento indutivo sem fios é dependente da indutância mútua medida entre a bobina transmissora e recetora que, por sua vez, no contexto do comportamento indutivo sem fios de veículos elétricos apresentará uma forte dependência da posição relativa entre o veículo e a bobina transmissora. Como tal, a determinação, com rigor, da indutância mútua trará diversos benefícios, nomeadamente no que diz respeito à atuação sobre a referida posição relativa entre o veículo e a bobina transmissora, aumentando deste modo a eficiência do sistema. No âmbito desta temática, os algoritmos baseados em técnicas de inteligência artificial surgem como soluções viáveis.

O trabalho desenvolvido propõe a estimação da indutância mútua de um sistema de transferência de potência indutivo sem fios com a topologia série-série-série, implementado em Simulink. A saída deste sistema representa um carregador típico de baterias, variável entre 500 W e 3000 W, na primeira fase de carregamento, ou seja quando a bateria se encontra descarregada. Para estimar este parâmetro, recorreu-se ao desenvolvimento e implementação de uma rede neural artificial. Deste modo, neste documento é apresentado em detalhe todo o processo relacionado com a implementação de um modelo de inteligência artificial, nomeadamente no que diz respeito à extração de características intrínsecas do sistema em análise, também denominadas de "*features*", e à normalização dos dados. Dadas a natureza do sistema, o processo de seleção das *features* teve em conta dois requisitos essenciais, sendo estes a variação acentuada com o desalinhamento do veículo e a ausência de variação quando a potência de carregamento é alterada.

Através da análise realizada chegou-se à conclusão que as variáveis mais suscetíveis de serem utilizadas para este fim, seria a amplitude dos harmónicos relativos a grandezas medidas do lado da bobina recetora.

Tendo como objetivo o desenvolvimento de um modelo de inteligência artificial robusto e com potencialidades para ser implementado num sistema real, decidiu-se limitar, ao máximo, a quantidade dos dados de treino, tendo sido para tal apenas utilizado cerca de 1% dos dados disponíveis. O desempenho da rede neural artificial desenvolvida foi testado em duas situações distintas, estando estas relacionadas com o facto dos dados de treino terem sido obtidos a partir de sinais com e sem ruído branco. Após a análise dos resultados, verificou-se que o maior erro de estimação da indutância mútua obtido foi de aproximadamente 3% para uma potência de carregamento de 500 W. Posto isto, é possível inferir que a rede neural artificial proposta tem a capacidade de estimar o valor de indutância mútua corretamente.

Palavras-chave: Eletrónica de potência, sistema de transferência de potência indutivo, estimação da indutância mútua, aprendizagem profunda, redes neurais artificiais.

Contents

List of Symbols

σ	Non-linear activation function
$\Theta_i^{(l)}$	weight vector for the i-th neuron in the l-th hidden layer
$b_i^{(l)}$	bias term of the i-th neuron in the l-th hidden layer
C_{out}	Output capacitor
C_p	Capacitor o the resonant tank referred to the primary coil of the first magnetic coupling
C_t	Capacitor of the resonant tank referred to the transmitter pad
C_r	Capacitor of the resonant tank referred to the receiver pad
F_s	Sampling frequency
$\overline{I}_p$	Current that flows in the primary coil of the first magnetic coupling
$\overline{I}_s$	Current that flows in the secondary coil of the first magnetic coupling
i_{sec}^3	Amplitude of the third harmonic of current measured in the receiver pad
$\overline{I}_t$	Current that flows in the transmitter pad
$\overline{I}_r$	Current that flows in the receiver pad
L_p	Self-inductance of the primary coil of the first magnetic coupling
L_s	Self-inductance of the secondary coil of the first magnetic coupling
L_t	Self-inductance of the transmitter pad
L_r	Self-inductance of the receiver pad
M	Mutual inductance
Q^3	Amplitude of the third harmonic of reactive power
R_{eq}	Equivalent resistance of the rectifier together with the batteries and corresponding charger

r_p	Resistance of the primary coil of the first magnetic coupling
r_s	Resistance of the secondary coil of the first magnetic coupling
r_t	Resistance of the transmitter coil
r_r	Resistance of the receiver coil
T_s	Sample time
u_l	Input vector of the l-th layer
v_4^3	Amplitude of the third harmonic of voltage measured in terminals of receiver pad
v_4^5	Amplitude of the fifth harmonic of voltage measured in terminals of receiver pad
v_5^{FC}	Amplitude of the fundamental component of voltage measured in receiver pad after the capacitor of the resonant tank referred to the receiver pad
v_5^3	Amplitude of the third harmonic of voltage measured in receiver pad after the capacitor of the resonant tank referred to the receiver pad
v_5^5	Amplitude of the fifth harmonic of voltage measured in receiver pad after the capacitor of the resonant tank referred to the receiver pad
$\overline{V}_1$	Fundamental component of the output voltage of the high frequency inverter
V_{ak}	Forward voltage of the diodes of the rectifier
$\overline{V}_{Ct}$	Voltage measured at the terminals of the resonant tank of the transmitter pad
$\overline{V}_{Cr}$	Voltage measured at the terminals of the resonant tank of the receiver pad
$\overline{V}_{Lp}$	Voltage measured at the terminals of the primary coil of the first magnetic coupling
$\overline{V}_{Ls}$	Voltage measured at the terminals of the secondary coil of the first magnetic coupling
$\overline{V}_{Lt}$	Voltage measured at the terminals of the transmitter pad
$\overline{V}_{Lr}$	Voltage measured at the terminals of the receiver pad
$\overline{V}_{ps}$	Voltage Source referred to the secondary coil of the first magnetic coupling
$\overline{V}_{rt}$	Voltage Source referred to the transmitter pad

$\overline{V}_{sp}$	Voltage Source referred to the primary coil of the first magnetic coupling
$\overline{V}_{tr}$	Voltage Source referred to the receiver pad
$z_{l,i}$	Output of the i-th neuron in the l-th layer
$\overline{Z}_{rOUT}$	Reflected impedance from the receiver side into the transmitter side
$\overline{Z}_{rIN}$	Reflected impedance of the secondary side of the first magnetic coupling into its primary side

Acronyms

AC Alternating Current

AI Artificial Intelligence

ANN Artificial Neural Network

CNN Convolutional Neural Network

DC Direct Current

DDPG Deep Deterministic Policy Gradient

DIPT Dynamic Inductive Power Transfer

DL Deep Learning

DRL Deep Reinforcement Learning

DT Decision Tree

EV Electric Vehicle

FC Fundamental Component

FFNN Feed Forward Neural Network

IPT Inductive Power Transfer

LSTM Long Short-Term Memory

MAE Mean Absolute Error

MAPE Mean Absolute Percentage Error

ML Machine Learning

MLP Multi-Layer Percepton

MSE Mean Square Error

NN Neural Network

R^2 Coefficient of Determination

RBF Radial Basis Function

RF Random Forest

RFR Random Forest Regression

RMS Root Mean Square

RMSE Root Mean Square Error

SVM Support Vector Machine

SVR Support Vector Regression

SSS Series-Series-Series

WPT Wireless Power Transfer

List of Figures

List of Tables

Chapter 1

Introduction

In the context of electric vehicles (EVs), inductive power transfer (IPT) systems have a significant room for improvement so that in a near future this technology can be implemented in large scale, facilitating the usability of an EV. In this chapter it will be presented a brief contextualization as well as the limitations associated to IPT systems and how the employment of an artificial intelligence (AI) model can actively contribute to the optimization of power transfer capabilities.

1.1 Contextualization of Wireless Charging

IPT is an idea based on wireless power transfer. This concept was discovered in the end of the 19th century, more specifically in 1891, by the famous scientist Nikola Tesla [1–4]. He verified that by connecting an AC current source to a primary coil, it will produce an alternating magnetic field, as expressed by the Ampere law. In these conditions, if a secondary coil is near the primary coil, and so, affected by the alternating magnetic field, a voltage is induced in it, and a current will flow throw it if the circuit is closed, according to the Faraday law [5]. In Figure 1.1 it is possible to see an illustration of the principle that allows inductive power transfer.

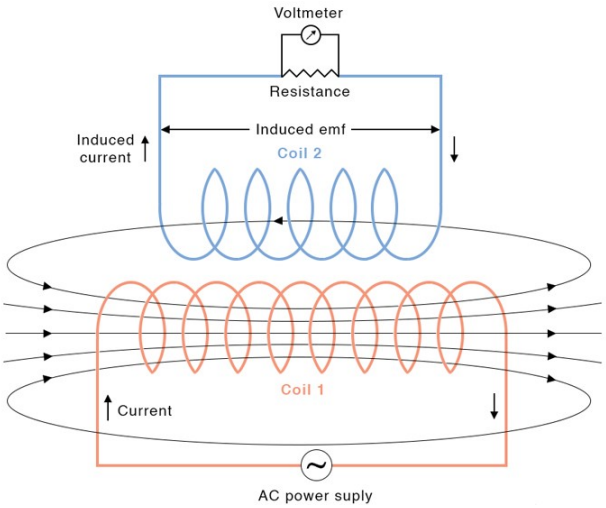

Figure 1.1: Representation of the principle of inductive power transfer [6].

However, the applicability of this new technology was limited due to the large currents measured in the secondary coil. Later on, more precisely in the 1980's,

thanks to various contributions, the interest for inductive power transfer returned with the advent of power electronic switches that worked at high switching frequencies [7]. This opened the door to new possibilities in terms of applications. In recent times, this concept is applied in various ways like in factory automation, lighting, medical devices, security systems among others [8]. Nevertheless, the majority of the interest from the scientific community spread toward a specific area, the automotive industry, mostly in wireless battery charging systems for EVs [9]. The allocation of resources was justified by the significant advantages IPT systems offered. This charging method, since it is capable of providing power transfer without any contact between the coils, offers several associated benefits, including galvanic isolation, absence of user interaction [10] and protection under adverse weather conditions [11], guaranteeing a more convenient way to use the vehicle. Therefore, there are essentially two types of wireless charging systems [1], [9], [12]:

1. Static Wireless Charging Systems
2. Dynamic Wireless Charging Systems.

The working principle of these two types of wireless charging systems is similar, the only difference being, as the names suggest, the way how the charging process is accomplished. Typically, the structure consists of two magnetic couplers, a transmitter pad, commonly known as primary coil, and a receiver pad, also acknowledged as secondary coil. The transmitter pad is placed under the ground, while the receiver pad is installed beneath the EV chassis. A block diagram illustrating this system is shown in figure 1.2.

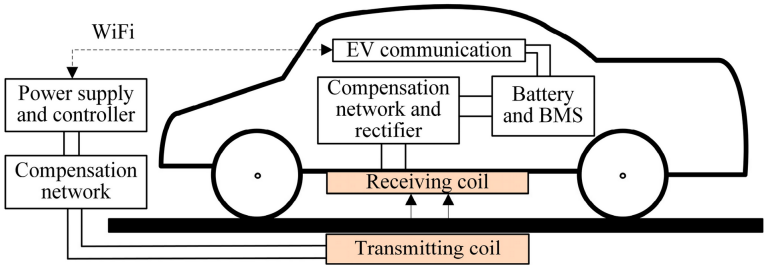

Figure 1.2: Simplified illustration of a wireless charging system for EVs [13].

1.2 Motivations

As a system that enables wireless power transfer, it has its limitations in terms of dependence on the coupling factor of the magnetic couplers. According to the Faraday law of electromagnetic induction, the induced voltage on the receiver pad depends on the rate of change of the magnetic flux that traverses it [14].
Generally, the coupling factor decreases from the nominal operating conditions when a misalignment between the transmitter and receiver pads occurs. This results in a decrease not only of the mutual inductance but also in the output power. Consequently, the overall efficiency of the system will decrease too. Specially in the case of EVs, the misalignments are unavoidable, due to possible horizontal, longitudinal or vertical displacements [15]. In Figure 1.3 is shown a graphic representation of the direction established for the misalignments in this document.

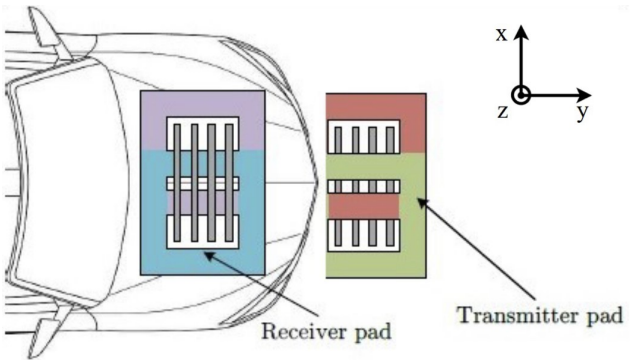

Figure 1.3: IPT system for static charging application - adapted from [10].

Moreover, for contextualization purpose, another characteristic of IPT systems that can influence the behavior of the system is the configuration of the coils. In [9] a comparison was made between an IPT system using two coil configurations, double D pad (DDP) and bipolar pad (BPP). This comparison consisted on observing the results of mutual inductance between the transmitter and receiver pads and also output power of the system. This experiment was done under various of misalignments when a current of 20 A flowed through the transmitter pad. Figure 1.4 displays the power transfer capability of these magnetic couplers under situations of misalignment. In this case in specific it was measured the uncompensated power since it was used coreless structures to reduce costs. Thus it can be concluded that misalignments between the transmitter and receiver pads does indeed imply a reduction of the overall system efficiency.

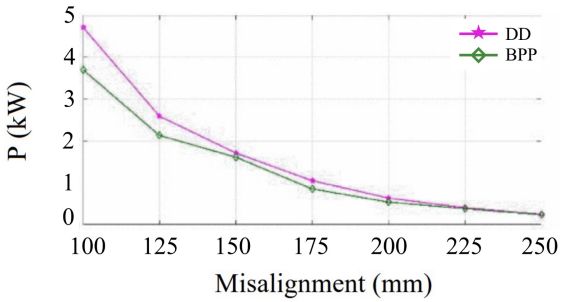

(a) m_z misaligment

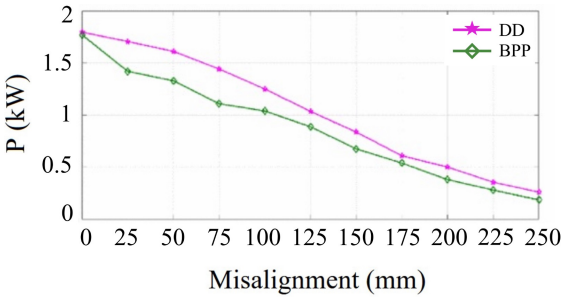

(b) m_y misalignment

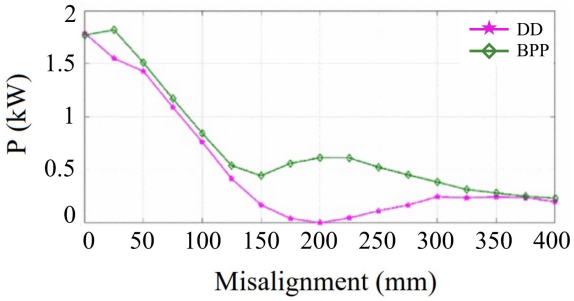

(c) m_x misalignment

Figure 1.4: Uncompensated power for DDP-DDP and DDP-BPP magnetic couplers for different vertical 1.4a, longitudinal 1.4b and horizontal 1.4c misalignments respectively - adapted from [9].

The presented background of IPT systems, regarding the influence of misalignments on the power output of the system and also on the mutual inductance is crucial, since acknowledges the idea that knowing the value of mutual inductance for a given condition of misalignment can directly contribute to the optimization of the charging process. The value of mutual inductance can be obtained through an estimation process, which includes possibilities such as mathematical and AI models. AI models have emerged as a superior solution, therefore, the proposal of an AI model capable of estimating the value of mutual inductance, using data from the receiver side is presented. Furthermore, the access to the output of the AI algorithm information will enable the correction of the position of the vehicle, optimizing the charging process.

Given this brief contextualization of the proposed work, the next section will outline the main objectives to be achieved in this dissertation.

1.3 Objectives

The work developed along this dissertation has been intended to reach the following objectives:

- ◇ Understand the working principle and limitations of IPT systems.
- ◇ Adjust the simulation model to a more realistic approach.
- ◇ Comprehend the advantages associated to the estimation of mutual inductance.
- ◇ Get a contextualization of the coverage that AI has in power electronics field of investigation, more specifically regarding the IPT systems.
- ◇ Select the best suited features to characterize the behavior of the IPT system.
- ◇ Understand the influence of data normalization, feature selection and dataset dimensions in the performance of the AI model.
- ◇ Choose the best suited AI solution for this matter.
- ◇ Develop a robust model that could have the potential to be used in a real-world scenario.

1.4 Structure of the Document

The developed work in this thesis is organized in six chapters, starting by Chapter 1 which introduces the research background, contextualizes the motivations and outlines the objectives intended to be achieved.

Chapter 2 presents a detailed analysis of IPT systems, especially regarding the characteristics attended for the development of this work. Furthermore, it also presents possible mathematical approaches for estimating mutual inductance as well as an overview of AI concerning the algorithms available and the typical tasks in power electronics field of investigation. This chapter also provides a literature review showcasing the possibilities available to implement AI algorithms in IPT systems

for regression purposes. Receiver pad position, mutual inductance between the transmitter and receiver pads, load resistance and coupling coefficient are examples of parameters that can be estimated in IPT systems.

Chapter 3 focuses on presenting in detail the IPT system used for this work. Moreover, it also introduces to the process of feature selection and consequent dataset generation.

Chapter 4 is devoted to unveil the proposed AI model and a careful analysis of the performance of the model under different situations.

At last, Chapter 5 depicts the main conclusions of this work and lists some research topics for future work in this field of investigation.

Chapter 2

AI Algorithms in IPT Systems

This chapter aims to present the theoretical principles that underlie the subjects explored in this work along with a comprehensive literature review on AI algorithms employed within IPT systems. Therefore, in a first instance it will be presented the fundamentals of a conventional IPT system, the existent mathematical methods for estimating mutual inductance, an overview of AI algorithms within the field of power electronics research and also useful concepts for the employment and testing of AI algorithms. At last the literature review will focus on the potential implementations of AI algorithms in IPT systems, particularly in the context of regression tasks.

2.1 Mutual Inductance in IPT Systems

To successfully implement an AI model that is able to predict the mutual inductance of a IPT system it is crucial to first understand the conditions of operation of these systems. Hence, Figure 2.1 shows the circuit associated to a conventional IPT system for EVs, where L_t and L_r correspond to the self inductance of the transmitter and receiver side, respectively, and C_t and C_r are related to the resonant capacitances of the transmitter and receiver sides, respectively. On the other hand, the M symbol refers to the mutual inductance between the transmitter and receiver pads, which depends on the distance between them, the angle of the receiver pad and also the number of turns and permeability of each pad [16].

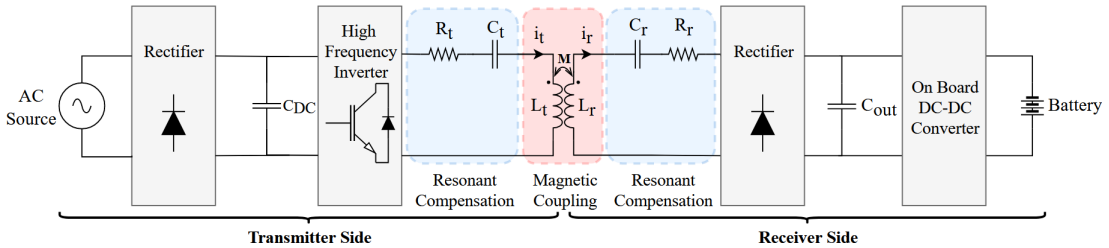

Figure 2.1: Representation of a conventional IPT system circuit.

The output power and consequently the efficiency of an IPT system are dependent on the misalignment between the transmitter and receiver pads and, thus, on the mutual inductance. In a conventional IPT system the output power can be characterized as (2.1):

$$P_{out} = w \cdot \overline{I}_t^2 \cdot k^2 \cdot L_t \cdot Q, \tag{2.1}$$

where w is the angular frequency of the power supply, I_t corresponds to the rms value of the current in the transmitter pad coil, L_t is the self-inductance of the transmitter pad, Q refers to the quality factor of the receiver circuit and k is the coupling factor and it is given by (2.2).

$$k = \frac{M}{\sqrt{L_t \cdot L_s}}, \tag{2.2}$$

where L_s refers to the self-inductance of the receiver pad.

Therefore, considered the formal relationship between these variables, some developments were made to mitigate the decrease of efficiency with the misalignments. These type of circuits are highly non-linear due to the presence of resonant elements in the circuit, so there was the need to ensure the operation at resonance to boost the power transfer capability.

Taking a closer look to the elements of the circuit and their purpose, it can be observed that the transmitter and receiver coils have the corresponding resonant filters where their natural frequency f_0 must be equal to the ac power source frequency f, provided by the high frequency inverter. In these conditions $f_0 = f$ which ensures the operation at resonance. Typically, this is achieved by adding appropriate inductors and capacitors, either in series or in parallel, depending on the circuit that is being analysed, to the circuitry of each magnetic coupler. This way, the input impedance of the circuit will be purely resistive, i.e., the voltage and current will be in phase [4, 5]. These resonant filters can be implemented using different topologies as illustrated in Figure 2.2.

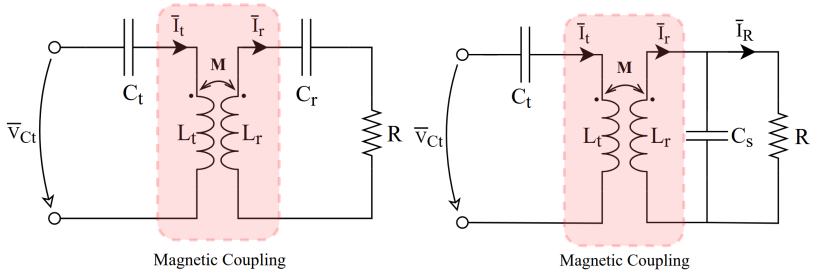

(a) Series-series Topology (b) Series-parallel Topology

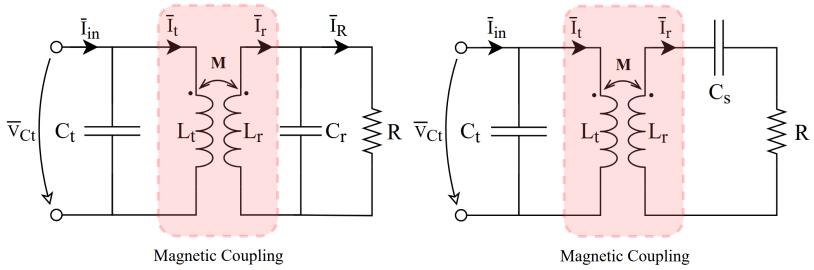

(c) Parallel-parallel Topology (d) Parallel-series Topology

Figure 2.2: Resonant topologies - adapted from [5].

Moreover, working at resonance keeps the switching losses of the IGBTs of the inverter at a minimum, thus, ensuring that the maximum power transfer capability is achieved. Also, to increase the power transfer capabilities, it is recommended that the system operates at high frequency [17], contributing to circuit miniaturization

[9]. In some cases, depending on the power level of the components, the switching frequency can be in the range of hundreds of kHz [18].

Nevertheless, it is also important to note that when analyzing the circuit at resonance, the magnetic couplers are replaced by dependent voltage sources, as displayed in Figure 2.3. This is possible because each coil senses the magnetic flux of both itself and the other coil.

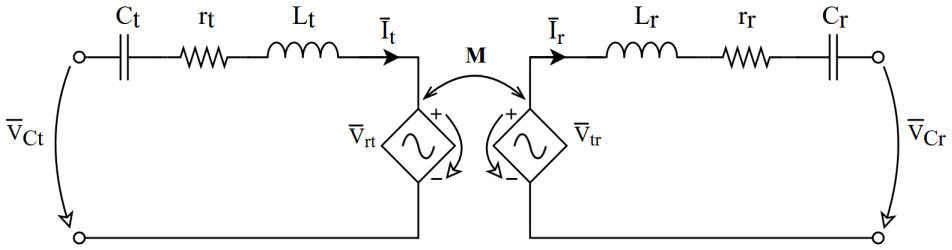

Figure 2.3: Representation of the magnetic couplers with dependent voltage sources.

In this representation:

$$\overline{V}_{rt} = -j \cdot w \cdot M \cdot i_r \tag{2.3}$$

$$\overline{V}_{tr} = j \cdot w \cdot M \cdot i_t, \tag{2.4}$$

where i_t and i_r represent the currents of transmitter and receiver side, respectively.

In addition, regarding the subject of mutual inductance estimation, there are different mathematical approaches possible, including the ones that only need information of the receiver or transmitter sides. Therefore, the estimation of this parameter is highly dependent on the configuration of the circuit. In [19], since the circuit has a DC-DC buck converter included, the number of parameters needed for the calculation of the mutual inductance will increase significantly as demonstrated in (2.5):

$$M = \frac{V_{DC} D_B R_{eq} sin(\frac{\pi}{2} D_i) + \sqrt{D_B^2 V_{DC}^2 R_{eq}^2 sin^2(\frac{\pi}{2} D_i) - 4 V_L r_T (r_r + R_{eq})}}{2 V_L}, \tag{2.5}$$

where V_{DC} corresponds to the output voltage of the rectifier, D_B is the duty ratio of the DC-DC buck converter placed after the rectifier, R_{eq} is the equivalent resistance seen from the rectifier, D_i corresponds to the duty ratio of the high frequency inverter, V_L match the nominal load voltage and finally r_T and r_R relate to the resistance of the transmitter and receiver coils, respectively.

Furthermore, in [20] the mathematical estimation of the mutual inductance has the purpose of being implemented in real-time for a dynamic wireless charging system. Conventionally, the mutual inductance can be estimated by (2.6):

$$M = \frac{V_{1,0} + \sqrt{V_{1,0}^2 - 4 r_t I_r (V_2 + r_r I_r)}}{2 I_r w}, \tag{2.6}$$

where $V_{1,i}$ corresponds to the RMS voltage of the transmitter side and I_r is the fundamental component of the current of the receiver side. Additionally, to reduce the noise effect introduced by the power electronics devices, it was proposed that the

mutual inductance should be estimated by a recursive least square filter. A similar approach was also employed in [21].

In [22], a different strategy is followed with respect to mutual inductance estimation for a dynamic wireless charging system. It is proposed an IPT system with three receiver coils where the estimation of the mutual inductance will be based on the structure parameters of the magnetic couplers and also on the amplitude of the magnetic flux density. As a result the process of mutual inductance estimation is divided in three main steps:

1. Run a simulation program and obtain the amplitude of the magnetic flux density, B_{z-max}, and the shape-parameter, σ.

2. Determine the value of each calculation-coefficient according to the parameters of the receiver.

3. Calculate the mutual inductance value using (2.7).

$$M = \frac{\psi_m}{I_p} = \frac{2\tau}{\pi} \cdot \frac{B_{z-\max}}{I_t} \cdot k_x \cdot k_l \cdot k_w \cdot N_R \cdot k_N \cdot q \cdot k_d \cdot k_c, \tag{2.7}$$

where τ is the distance between each receiver coil, I_t refers to the RMS value of the current in the transmitter coil, k_x, k_l and k_w are coefficients that describe the functional relationships between mutual inductance and the position of the receiver, the length of the receiver coil and the width of the receiver coil, respectively, N_R is the number of turns of the receiver coil, k_N corresponds to the coefficient that describe the functional relationship between mutual inductance and the number of turns of the receiver coil, q, is the number of receiver coils, k_d is relative to the coefficient used to describe the functional relationship between the mutual inductance and the center distance between the receiver coils and finally k_c is referred to the core coefficient.

Furthermore, in [23] it is presented an energy transfer control method based on the estimation of the load and mutual inductance of a segmented dynamic wireless power transfer system with four transmitter pads. Similar to the previous citation, the procedure of mutual inductance estimation can be separated into five main procedures:

1. Measurement of the voltage in each transmitter resonant capacitance, the current in each transmitter coil, the phase between them and the phase difference between the referred current and each inactivated transmitting coil.

2. Calculation of the reflected impedance from each transmitter coil and also the coefficient between the real and imaginary part of the input impedance of the rectifier.

3. Calculation of the input impedance of the rectifier and its normalized value.

4. Calculation of the equivalent impedance of both the receiver and rectifier sides.

5. Calculate the mutual inductance associated to each transmitter pad, according to:

$$M_k = \frac{|Z_r|}{\omega}\sqrt{\frac{R_{f1c}}{\mathrm{Re}(Z_s)}}, \tag{2.8}$$

where k represents the number of the transmitter pad ($1 \leq k \leq 4$), Z_s is the equivalent impedance of the secondary side and R_{fkc} is the reflected impedance from transmitter k.

Thus, by analysing the possibilities of mutual inductance estimation with mathematical approaches it becomes evident that because these models require a substantial amount of information about the IPT systems and the relationships between the parameters are significantly nonlinear, this will lead to a high computational cost and long calculation times. Subsequently, an AI model has the potential to get a better fit concerning the estimation of the mutual inductance owing to the capability of adjustment to different configurations of IPT systems and also the faster delivery of results with less need of computational power.

2.2 Overview of AI Algorithms in Power Electronics

The inception of computing in the 1950s marked a turning point in the development of algorithms with the ability to autonomously and intelligently perform tasks across various domains. These algorithms started to be recognized as AI algorithms [24].

Taking as an example the specific case of power electronics field, as mentioned in [25], AI algorithms have been applied in three particular life-cycle phases of power electronics: control, maintenance and design. Not only it can be implemented in various domains as it can also be applied in diverse ways. Essentially, AI at its simplest form, is a field, which combines computer science and robust datasets, to enable problem-solving [26], therefore, being the ability of a digital computer or computer-controlled robot to perform tasks commonly related with intelligent being [27]. is a vast concept and encompasses two major subcategories [28] as illustrated in Figure 2.4.

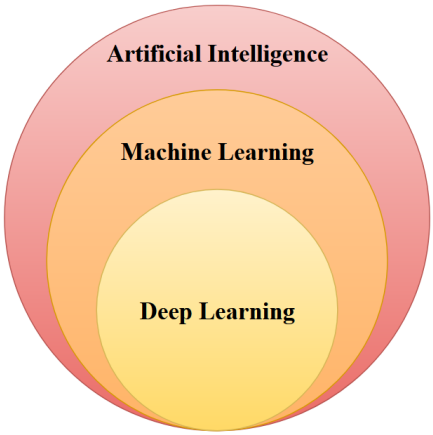

Figure 2.4: Relation between AI, ML and DL.

1. **Machine Learning:** Algorithms with the ability to learn from data and make decisions from it without explicit programming, although it may still be necessary human intervention for some unwanted behaviors. These algorithms can be classified into various ways, as displayed in Figure 2.5.

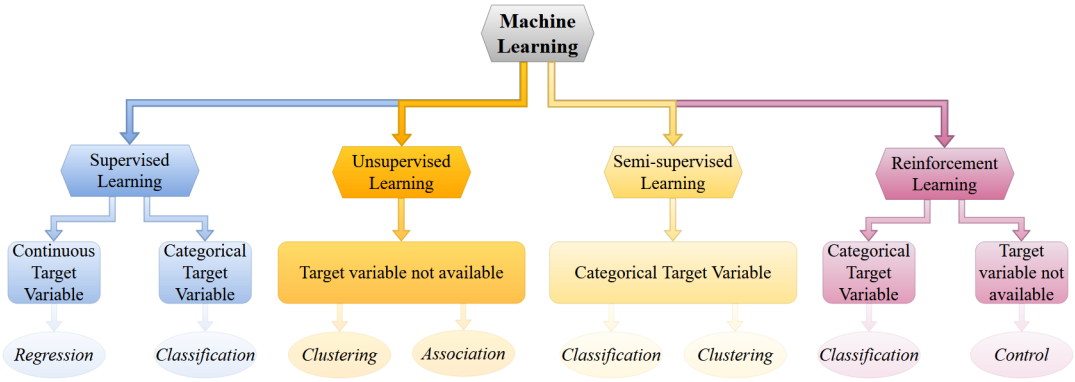

Figure 2.5: Types of machine learning [29].

As it can be observed, there are four major categories of ML. According to [30]:

Supervised Learning: Consists in techniques that rely on training datasets containing labeled data. The training phase allow the ML algorithm to develop an inferred function to foresee the pretended output values. This way, when deployed with a new set of data, it is able to provide results and then compare them with the expected ones so that it can identify errors.

Unsupervised Learning: In this case, the ML algorithms only have the purpose of deducing a function that is capable to find hidden patterns in unlabeled data.

Semi-supervised Learning: These ML techniques lie between the ones presented previously, in a manner that considers two types of data, labeled and unlabeled. The labeled data is provided in a smaller quantity compared to the unlabeled data, thus its goal is to provide the essential characteristics of the data through the labeled data.

Reinforcement Learning: This learning method relies on trial and error, i.e., an agent interacts with the environment thorough actions, receiving, consequently, rewards and penalties. Accordingly, the system can identify the ideal behavior in a specific circumstance.

2. **Deep Learning:** It uses networks to learn, adapt and reach decisions without human intervention. Similar to ML, DL can be segmented into three main categories, supervised learning, unsupervised learning and hybrid learning, also known as semi-supervised learning [31]. The description provided for these learning methods also applies to DL. In Figure 2.6 is displayed the ramification of each type of learning into the different DL techniques commonly used for that purpose.

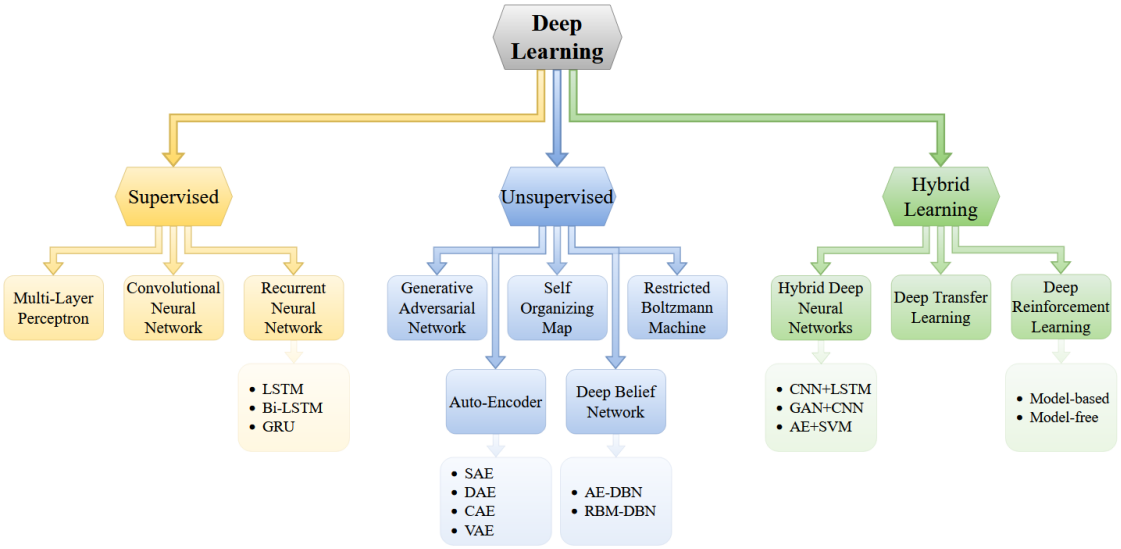

Figure 2.6: Types of deep learning [32].

Nonetheless, due to the fast development of AI algorithms in the past years, these subcategories of AI have extended to various domains, depending on the application [33]:

- ◇ **Natural Language Processing:** Refers to a domain of AI where the algorithm learns to understand and generate human language;
- ◇ **Robotics:** Although it is considered a recent domain of AI, it has been established that it associated with the design and development of machines that can perform tasks without human intervention;
- ◇ **Expert Systems:** An AI algorithm is classified inside the domain of expert systems, when it is developed using a knowledge base and a set of rules to mimic the decision-making process of humans in a particular field, being also capable of providing explanations for its decisions.

Considering that IPT systems are part of the power electronics field and in agreement with [25], there are four tasks where AI is essential in this field of investigation, being them:

1. **Classification:** With this regard, the training set is prepared with labeled input data, i.e., data with the correspondent discrete class. Within this topic, it is associated mainly to maintenance purposes, including anomaly detection and fault diagnosis.
2. **Data Structure Exploration:** This function has the purpose of data clustering, density estimation and data compression. These features have the purpose of, respectively:
   - ◇ discover groups of similar data within the dataset;
   - ◇ determine the distribution of data within the input space;
   - ◇ project high-dimensional data down to low-dimensional data for feature reduction.

3. **Optimization:** In this case, the network is designed to find an optimal solution based on the given objective. This process is done based on different boundaries, equalities or inequalities that the solutions have to fulfill. In power electronics, this function is often used in design tasks, i.e., when it is necessary to find the optimal parameters that satisfy the previous established design constraints.

4. **Regression:** Lastly, the goal of regression is to find a relation between the input and the target values. Thus, the model will be able to predict one or more continuous target variables for a set of input values. In this field of investigation, these models are frequently deployed into intelligent controllers. It is particularly useful in situations like in the analysis of the input electrical signals and estimation of the best fitting output control variable.

In [25], it has also been stated that, according to Figure 2.7, the majority of the tasks of AI in the power electronics field of investigation predominantly involve regression and optimization. More specifically, considering all applications of AI in power electronics, 33.3% correspond to optimization and 58.4% correspond to regression.

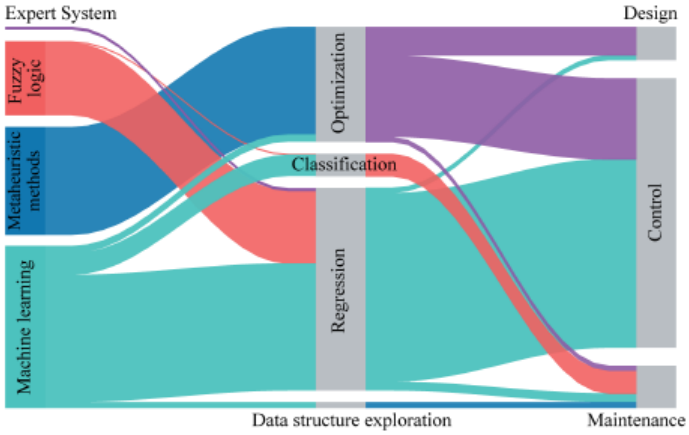

Figure 2.7: Sankey diagram of AI methods and applications in each phase of the life-cycle of power electronic systems [25].

Nevertheless, independently of the AI technique used, when applied to power electronics in general, signal processing emerges as an exceptional tool. In this context, for the specific case of regression tasks, there is a process with three main steps [34] that are recommended to be followed to successfully achieve the best possible results. Figure 2.8 displays a flowchart of the learning process.

In alignment with the flowchart displayed in Figure 2.8, the evaluation of the performance of the model usually is associated with the analysis of metric trends during the testing phase. This approach is preferred as the outcome of the metrics in the training phase can be inconclusive owing to potential overfitting[1] concerns. Essentially, a good metric must provide reliability, sensitivity to sudden changes in data, interpretability and also clear information about the error distribution. In previous works [35][36] it has been pointed out that no isolated metric can outperform

[1]It happens when the model can perform well with the training data but fails to generalize to unseen data.

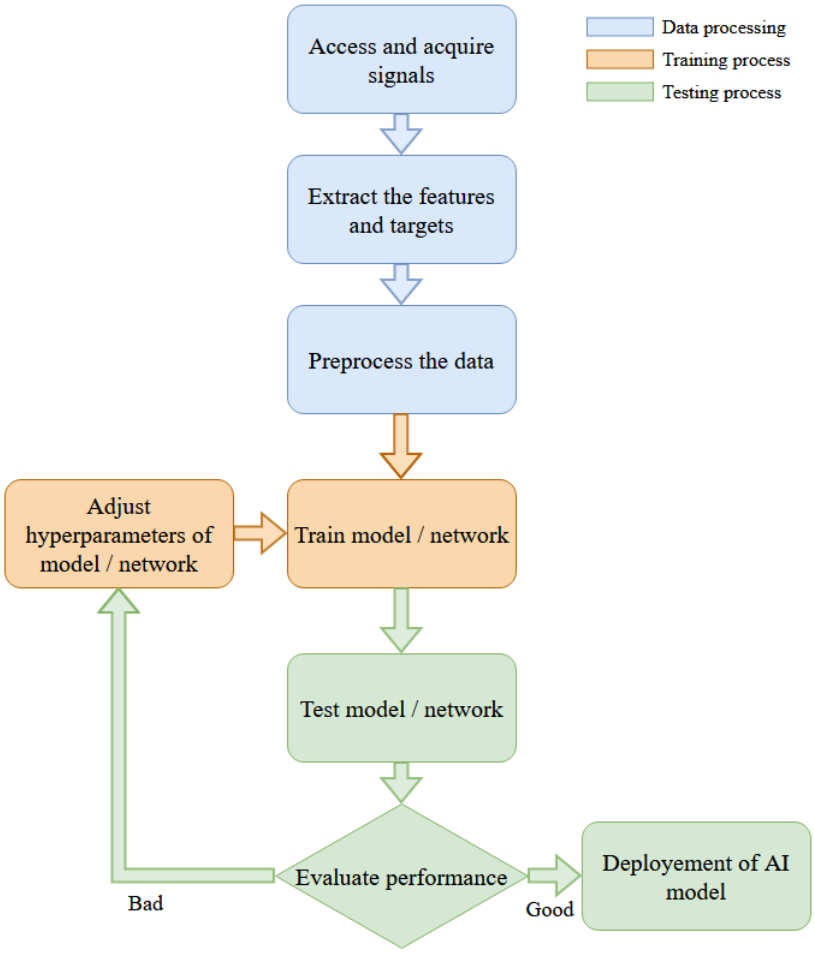

Figure 2.8: Block diagram of the learning process - adapted from [34]

the remaining ones in every category mentioned beforehand, so it is recommended to always use more than one metric to get a better understanding of the performance of the model. Consequently, for regression tasks [37–41], the metrics commonly used are presented next, where y_i corresponds to the real value, $\hat{y}_i$ corresponds to the predicted value, i is the number of the sample and n is the total number of samples.

◇ **Mean Absolute Error (MAE)**

The MAE metric provides a measure of the average absolute prediction error and is useful when the objective relies on reducing the magnitude of the errors. It is considered a more robust metric compared with MSE and RMSE.

$$MAE = \frac{1}{n}\sum_{i=1}^{n}|\hat{y}_i - y_i|. \tag{2.9}$$

◇ **Mean Absolute Percentage Error (MAPE)**

To overcome the lack of sensitivity of MAE to large or small errors, MAPE provides a percentage measure of the average prediction error, making this metric better in terms of interpretability.

$$MAPE = \frac{1}{n}\sum_{i=1}^{n}\frac{|\hat{y}_i - y_i|}{y_i}. \tag{2.10}$$

◇ **Coefficient of Determination (R^2)**

This metric offers a clarification into how the model fits the given data. The higher the R^2 value is, the better fit the model has to the data, so, it can give an idea of the proportion of variation between the target and predicted variables.

$$R^2 = 1 - \frac{\sum_{i=1}^{n}(y_i - \hat{y}_i)^2}{\sum_{i=1}^{n}(y_i - \overline{y})^2}. \tag{2.11}$$

As shown in Figure 2.8, if the performance of the model does not meet the requirements it becomes necessary to tune the hyperparameters. If the model that is being trained is a Neural Network (NN), some of the hyperparameters that can be tuned are:

◇ **Activation Functions:** Influence the ability of the network to approximate target functions [42].

– *Logistic Sigmoid:* It is mostly used in models that work with probabilities [43] or with classifications, because the output value of this function is between 0 and 1. An overview of the output of this function is presented in figure 2.9a.

$$f(x) = \frac{1}{1 + e^{-x}}. \tag{2.12}$$

– *Tanh Sigmoid:* In addition to the *logistic function*, it can map negative values, providing an output that is zero centered. In Figure 2.9b is presented an overview of this function.

$$f(x) = \frac{2}{1 + e^{-2x}} - 1. \tag{2.13}$$

– *ReLu:* This activation function has the particularity of transforming all input values that are negative into zero. In Figure 2.9c is displayed the characteristics of this function.

$$f(x) = \begin{cases} x, x \geq 0 \\ 0, x < 0 \end{cases} \tag{2.14}$$

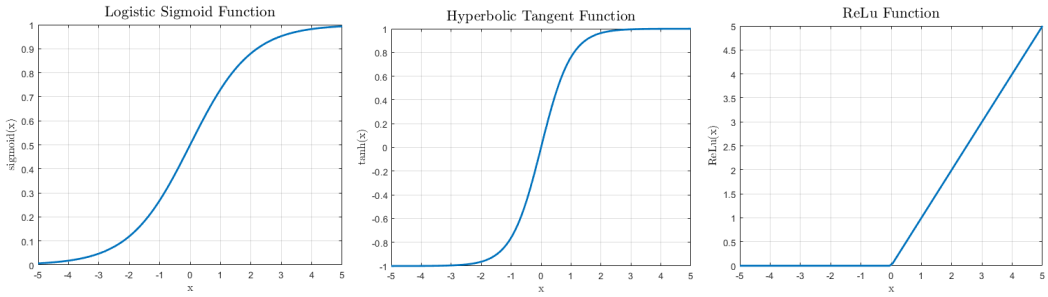

(a) Logistic sigmoid activation function (b) Hiperbolic tangent activation function (c) ReLu activation function

Figure 2.9: Activation functions commonly used.

- ◇ **Epochs:** The number of epochs defines how many times the model will iterate through the entire training set and so, how many times the parameters of the model will be updated [44]. The greater the number of epochs, the greater the risk of leading to overfitting, however a small number of epochs can lead to underfitting.
- ◇ **Learning Rate:** The learning rate is defined as the step size at which the parameters of the model are updated during the training process. Typically the learning rate becomes an issue when numerous training samples are provided and, consequently, the underlying system becomes incapable of valuable generalization [45].

2.3 AI Algorithms for Parameter Estimation in IPT Systems

There is no doubt that over the past years, IPT systems and AI are two hot topics among the research community. The particular reason for such circumstances, is that they have numerous advantages. On one hand, while AI has been applied in systems around us for the past decades [24], in present days there is growing recognition of its utility and value due to the diverse fields it can encompass, especially in power electronics [25]. On the other hand, the IPT systems have garnered increase attention due to the continuous growth of interest in wireless charging for EV batteries [15]. Therefore, this section will provide a concise overview of the key AI methodologies applied in the field of IPT systems. It will also delve into the significant advancements made in leveraging AI in IPT systems and showcase its potential across domains such as design optimization of IPT systems and parameter estimation. Table 2.1 presents an overview of this literature review regarding the parameters estimated and the AI models used for each application.

Table 2.1: Applications of AI algorithms for parameter estimation in IPT systems

References	Parameter Estimation	AI Model
[46]	Mutual inductance	ANN
[47]	Design parameters of IPT structure	ANN
[37]	Self and mutual inductances	ANN
[48]	Quality Factor	ANN
[38]	Mutual inductance, load impedance	RFR
[34]	Load impedance, power transfer, coupling coefficient	RF, DT, SVM, Adabooster with DT, XGboost
[49]	Mutual inductance	RFR
[50]	Load impedance, resonant frequency	RFR
[51]	Position of receiver pad	ANN, SVM
[52]	Position of receiver pad	ANN
[53]	Position of receiver pad	ANN
[54]	Mutual inductance, load impendace, self-inductance	ANN
[55]	Position of receiver pad	ANN
[56]	Power transfer	Not specified
[57]	Ferrite core structures	LSTM
[58]	Ferrite core structures	LSTM

AI models are essentially known for the ease on how they can establish relations between different types of data that, when compared with mathematical solutions, are considerable superior in terms of computational cost and execution time. In [46], the article focused the attention on building a deep learning network as the framework of uncertainty quantification to posteriorly compare its performance with the calculation results of a classic Monte Carlo algorithm. In that work, the objective was to design the WPT system for an EV using a DL network. Firstly, it was verified that the power transfer efficiency, η, is greatly affected by the spatial offset of the coils, meaning horizontal and longitudinal offsets, Δx and Δy, respectively, the angle of the receiver coil, α, and also the height between them d. Additionally, parameters of the compensation circuit can impose strong uncertainty in transfer efficiency as well, such as the equivalent resistance of the primary loop, r_t, the equivalent resistance of the secondary loop, r_s and also the load resistance, R_{eq}. To reach the established goal, the authors decided to divide the NN into three distinct parts where each part was a DNN model. This way, the quantification of the WPT efficiency uncertainty is obtained. The first part of the NN consists of six fully connected layers with 4, 64, 100, 32 and 1 neurons from front to back, respectively, as well as one batch normalization layer where the number of input features is set to 100. It gets as inputs the spatial variables, Δx, Δy, α and d and has the goal of estimating the mutual inductance. The second part of the NN is used to extract the essential feature of r_t, r_s and R_{eq}. It is composed by a single fully-connected layer with 3 neurons. Finally the third part of the NN takes M as well as the extracted features from r_t, r_s and R_{eq} as inputs to obtain as output the transfer efficiency η. It consists of five fully-connected layers with 4, 64, 32 , 16 and 1 neurons from front to back, respectively, and also a dropout layer, that similarly to the batch normalization layer, has the purpose of avoiding overfitting. Additionally, this design optimization of a WPT system was based on an enhanced version of the Aquila Optimization (AO) algorithm, often used to solve many multi-objective optimization problems. The conventional optimization process of the AO algorithm is divided into five phases: initialization of the population, global exploration, local exploration, global exploitation and local exploitation. However, the authors found that there were still some limitations in the stage of population initialization and global exploration phases so it was proposed that the first phase of population initialization would be based on chaos mapping so that the phenomenon of uneven distribution of population was avoided. On the other hand, adaptive inertia weight was implemented to prevent that in the first exploratory stage, the AO algorithm could not balance the global search ability and the local search ability. After experimental analysis, the proposed Deep Neural Network (DNN) model was able to acquire efficient quantification of uncertainty, i.e., by enhancing the WPT structure of the system through the implementation of the improved multi-objective AO algorithm, the range of fluctuation in WPT efficiency was reduced by 65.4%. This optimization approach increased the probability of achieving higher levels of power transfer efficiency, due to the fact that the mean transfer efficiency increased by 25.7% as it can be verified in Figure 2.10. Additionally, compared with the classic Monte Carlo algorithm, the estimation time was reduced by 800%. Although the implementation of this solution was noticeably more complex than other approaches, the results clearly demonstrate the benefits that AI brings to the optimization algorithms.

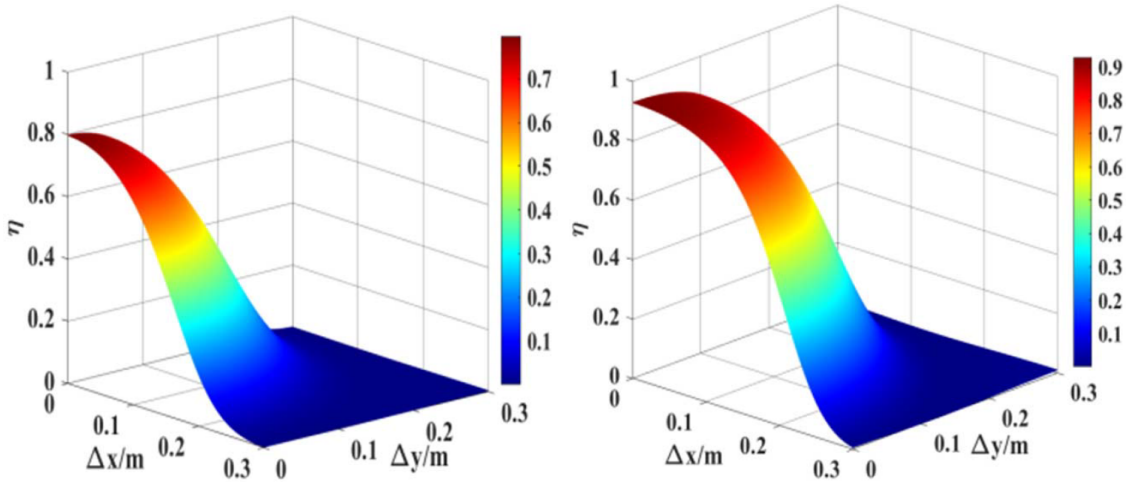

(a) Power transfer efficiency before optimization

(b) Power transfer efficiency after optimization

Figure 2.10: Comparison of the power transfer efficiency under variation of the horizontal and longitudinal offsets before and after 2.10a the optimization 2.10b [46].

Still, considering the field of investigation of WPT systems design optimization, two approaches are introduced in [47], one that allows the reduction of the training time and another that helps improving the input values of the network. The input variables that are taken into consideration are: X-direction length of the transmitter coil, Y-direction length of the transmitter coil, X-direction width of the transmitter coil, Y-direction width of the transmitter coil, length of the edge of the transmitter coil, distance between adjacent transmitter coils, length of the receiver coil winding, number of turns of the transmitter coil and the number of turns of the receiver coil. The approach that contributes to the reduction of training time is related with the reduction of Artificial Neural Network (ANN) training data collection time. This is applied to the estimation of the magnetic flux. The conventional method calculates the value of the magnetic flux when an arbitrary current flows through an arbitrary number of turns of the transmitter and receiver coils. Contrarily, the reduction of training data is possible due to the fact that the calculation of the stray magnetic flux is done separately, with the superposition of the magnetic fluxes created by one-turn receiver coil and one-turn transmitter coil, when a current of 1 A flows throw them. This allows the ANN to predict the value of the magnetic flux for any combination of turns and currents. Thus, it is more efficient to train the ANN in these conditions. In what improving the input values of the network is concerned a method based on the ANN and also on a genetic algorithm (GA) was proposed. The primary objective of this work is to predict the magnetic characteristics of the WPT system by using (randomly) as inputs of the network the ten previous presented design variables. Typically, among a large number of design points, those which satisfy twelve design criteria are chosen. Conventionally this method is challenging because many unnecessary design points, that don't fulfill the requirements, are predicted from random input values. Contrarily, the GA explores the input value space to identify the region that yields the desired design points fulfilling all twelve design criteria. This way, the ANN exhibits superior effectiveness in producing the

desired output values by leveraging this knowledge. Based on the input variables admitted range, the combination of an ANN and the GA was trained to output the twelve design criteria of various parameters. This training process relied on six main steps:

1. Random values are assigned to each design variable and input into the FEM simulator.

2. The FEM simulator utilizes the input design variables to calculate the corresponding magnetic characteristics.

3. The ANN learns the nonlinear relationship between coil dimensions and magnetic characteristics.

4. The fixed trained ANN receives the input design variables.

5. The network generates a large number of design points as outputs.

6. From this extensive set of design points, the optimal design point that satisfies all the predefined design criteria is identified.

Finally, the optimized ANN was composed by eight neurons on the input layer, due to the fact that the number of turns in the transmitter and receiver coils is equal to one, and ninety neurons on the output layer. Then, between these layers there are two hidden layers each with hundred neurons. Each neuron has an activation function that must be chosen according to the purpose of the model. Therefore, both the weights and the bias of each neuron are optimized. Subsequently, after defining a specific design specification for the DIPT system, it was analysed the performance of the network, including the validation error and the training error. It was verified that in a certain point the validation error tends to increase, but the training error continues to decrease. This is tendentially related to the overfitting phenomenon, where the network can only have a good performance with the training data. To prevent this from happening, the authors decided to stop the iterative calculations before the validation error started to increase as observed in Figure 2.11.

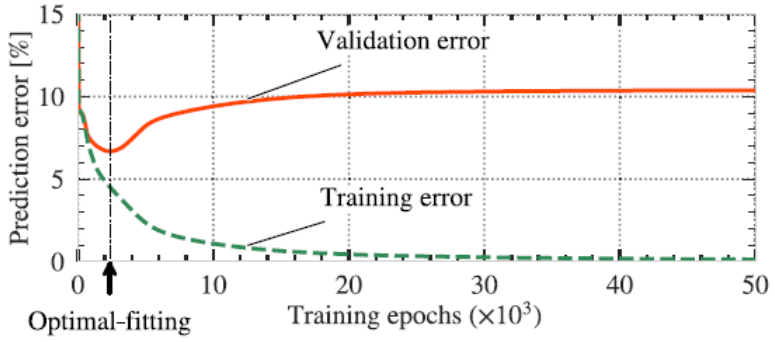

Figure 2.11: Prediction error with respect to the number of iterative calculations [47].

Regarding the verification process, it was demonstrated that the network had a remarkable performance. Comparing the results with the Finite Element Method (FEM) analysis, the error percentage ranged from 0.5% to 7%, corresponding to

the self inductance of the transmitter coil and stray magnetic field, respectively. Considering the results obtained with circuit simulation, the error percentage varied between 0.3% and 10.2% and it was relative to the transmitter coil voltage and the output power, respectively. In terms of experimental results, the error percentage varied from 0.5% to 29.9%, reflecting the self-inductance of the transmitter coil and coil losses, respectively. In Figure 2.12 is shown the predicting performance, in experimental environment, of this network regarding the output power.

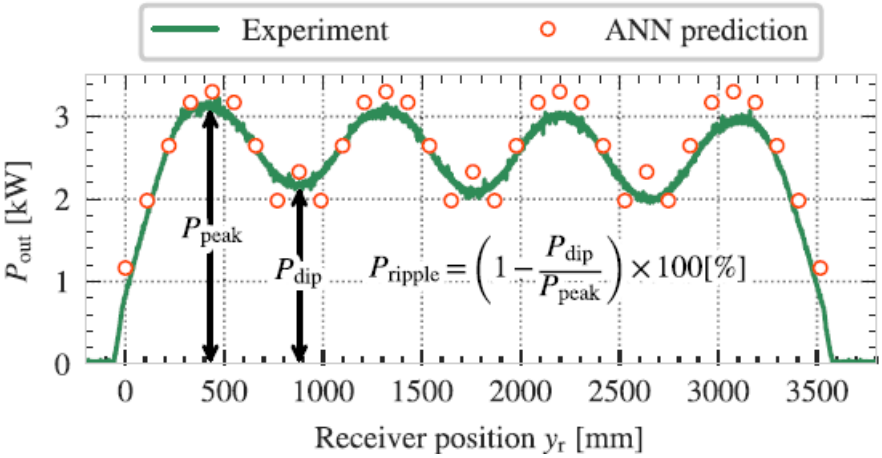

Figure 2.12: Measured and predicted output power with respect to the receiver position (Moving speed: 6 km/h) [47].

On the other hand, AI can be greatly useful in the calculation of certain parameters of the circuit, based on the given structural information of it. Referring to a conventional WPT system design, the self-inductance of both transmitter and receiver coils and also the mutual inductance are the most important electrical parameters since they affect the resonance frequency, quality factor, and power transfer efficiency [37]. The goal is to obtain the inductances for various structures. The data referring to the design parameters is pre-processed and modeled, to be used as training data. To achieve this, a DNN composed of five inputs (coil outer diameter, spacing between coils, coil wire pitch, coil inner diameter and spacing between coil and ferrite) and two outputs (self-inductance and mutual inductance) that were obtained using a field solver was implemented. In terms of model structure, it is composed by two hidden layers with 512 neurons each one activated by a Relu function. To analyse the network performance, it was chosen the mean squared error (MSE) as loss function and the mean absolute error (MAE) as the merit function [2]. Additionally, the chosen optimization algorithm was Adam and the learning rate was equal to 0.0001. The training phase was accomplished in 1000 epochs and the data was shuffled before each trial. The authors decided to divide the data only into train and validation data, excluding the testing data. Similar to what was presented in [47], the authors chose to stop the learning phase if the MSE of the validation data did not decrease a hundred times in a row. This algorithm was implemented in Python using Keras libraries, and the input parameter sets consisted of combinations of 5 coil outer diameters, 4 to 7 spacings between coils, 5 coil wire pitches, 1 to 3 coil inner diameters and 5 spacings between coil and ferrite,

[2]Merit Function: when associated with optimization problems, it has the purpose of analysing if the input data represents a solution to the problem or not, based on the output value [59].

combining in a total of 1735 possible samples of data. The results were promising, obtaining a maximum error for self-inductance and mutual inductance of 7.09% and 9.47%, respectively, and 0.92% and 1.36% for MAEs, concerning the self and mutual inductances, respectively.

Moreover, AI models can also be useful to characterize the quality factor in spiral coil designs for wireless power transfer systems [48]. This charging system operates in the MHz frequency range. Typically the operation in this frequency range can be advantageous due to the absence of requirement of magnetic cores to enhance the magnetic flux of the IPT system, which leads to the elimination of the losses in the magnetic cores and therefore the reduction of system weight [60]. The quality factor of the wireless power transfer system is given by (2.15), where X_{eq} corresponds to the equivalent reactance, R_{eq} is the equivalent resistance, L_t and r_t correspond to the inductance and resistance of the coil, respectively and C_{par} is related to the parasitic capacitance[3].

$$Q = \frac{X_{eq}}{R_{eq}} = \frac{w(L_t - C_{par}r_t^2 - C_{par}L_t^2w^2)}{r_t} \tag{2.15}$$

The spiral coil characteristics used for the training and evaluation phases was collected through the Ansys-Q3D simulator. These characteristics included the outer diameter (D_o), the inner diameter (D_i), the number of turns (N), pitch size (p) and the wire thickness (w_t) and all of them had specific range of values. The collected data was divided into three datasets, where the first dataset was used only in the training phase and the second and third datasets had the purpose of evaluating the model. The first dataset contained a total of 19874 samples, where each samples was inside the range established for each coil characteristic. The second dataset contained a total of 1091 samples that were disjoint from the samples of the first dataset although had the same range, whereas the third dataset was composed of 287 samples that were computed as a 5%-15% difference from the minimum and maximum ranges of the first dataset. The model consisted on a feed forward neural network (FFNN) with three hidden layers with 64, 128 and 32 neurons, respectively, and a ReLu activation function. Additionally, the authors chose the ADAM optimizer, a learning rate of 0.001 and the MSE as the loss function. Before the training phase, the data was preprocessed. Firstly, to ensure that the difference between the features was as even as possible, the data went through a normalization process. Plus, the first dataset was randomly shuffled into eight training datasets, where the first part had 10% of the total samples, the second part 20% and so on. The remaining data was used for validation purposes. It was concluded that the bigger the training set was, the better results would be obtained in terms of quality factor. Finally, when the model was tested with the second and third datasets, it had an accuracy of approximately 93%, which proved the efficiency of the AI model. An illustration of the model performance is presented in Figure 2.13.

[3]The parasitic capacitor is considered in this range of frequencies because it induces a parasitic self-resonance in the coil.

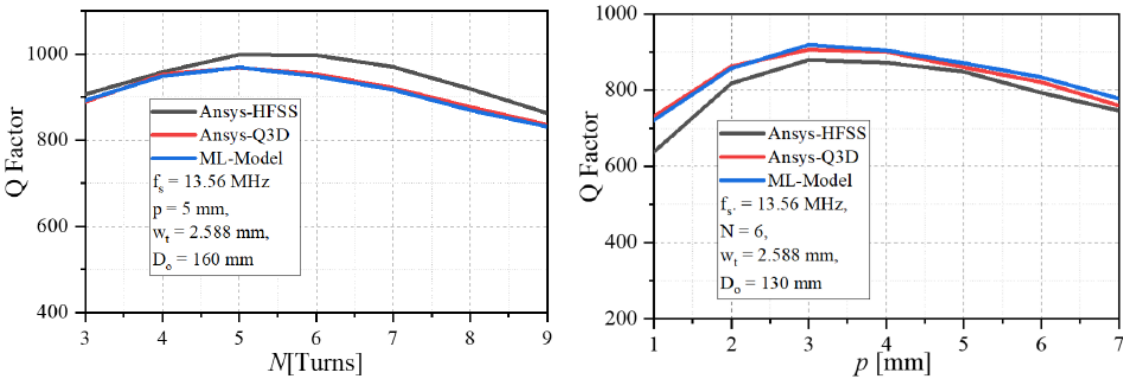

(a) Quality factor of the spiral coil with number of turns variance

(b) Quality factor of the spiral coil with pitch variance

Figure 2.13: Comparison of the quality factor of the spiral coil proposed by Ansys-HFSS, Ansys-Q3D and the ML model under number of turns 2.13a and pitch variance 2.13b [48].

Still concerning the parameter estimation, in [38] AI is employed to estimate not only the mutual inductance between the transmitter and receiver pads, but also the load resistance. Typically, the series-series-compensated IPT system is abundantly used in parameter identification problems, and in this case it is not any different since it enables the estimation of mutual inductance and load resistance at the transmitter side simultaneously. By inspecting the equivalent expressions of the load resistance and also the mutual inductance, it was possible to conclude that they can be acquired from the transmitter side simultaneously. Nevertheless, because the system is operating at a resonant frequency, these expressions will become unreasonable. Therefore, by using a front-end parameter estimation method at sub-resonant frequencies, it has been pointed that parameters of the system like the self inductance, the capacitor and the equivalent series resistance of coil on both the primary and secondary sides, are exceedingly sensitive for the mutual inductance and load resistance estimation near the resonant frequencies. Consequently, from the mutual inductance and the load resistance expressions, when operating at resonant frequencies, it can be concluded that these parameters are interrelated, so they cannot be estimated simultaneously. Moreover, in heavy load conditions, a slight parameter variation will cause high estimation errors. All things considered, the proposed Random Forest Regression is an accurate algorithm to handle a high number of input features, ensuring good estimation performance and also a good generalization error under forest building process. As a result of the target variables being interrelated, the models that estimate them had to be trained separately, one corresponding to mutual inductance estimation and the other to load resistance estimation. The most viable features were the voltage and current harmonics of the transmitter pad, because they were the ones that varied less, considering the operating frequency of the system. Regarding the experimental verification phase, the features were measured using a high-definition oscilloscope. All the data was obtained at the resonant frequency, indicating that this method does not affect the system operation. Cross-validation was the method used in training phase, allowing the evaluation and the adjustment of the model, in light of models performance. Subsequently the data went throw a process of normalization and also elimination

of outliers. Regarding the network tuning performance, $ntree$[4] and $mtry$[5] were two crucial parameters to optimize the model. By evaluating the performance of several combinations, it was concluded that the optimal values of these parameters were $ntree = 60$ and $mtry = 1$. The metrics of the model were analysed in two distinct situations:

1. The input data included higher-order harmonic voltages and currents.

2. The input data only included fundamental harmonics.

It was inferred that the case where the training data included high-order harmonics could improve significantly the models accuracy. The proposed model outperformed the traditional scheme by a significant margin. It achieved an error of 3.11% in mutual inductance estimation, surpassing the 5.05% error rate of the traditional method. Similarly, in load resistance estimation, the proposed model achieved an error of 3.65%, outperforming the 7.76% error of the traditional proposal.

Moreover, in [34] was proposed a ML approach which aims to estimate the power delivered to the receiver pad. It is also proposed a method to identify if the transmitter pad should be turned on or off based on the system efficiency as well as a method to estimate the load resistance and the coupling coefficient. This was accomplished by leveraging only on measurements obtained from the transmitter pad. The paper selected the LCC-S compensation topology to allow the supply of constant current independently of the load. Regarding the procedure on transmitter activation and deactivation, it was assumed that when the receiver is distant from the transmitter, i.e., the load resistance is very high, the efficiency of the system will be low so the transmitter should be turned off. When the opposite happens, the transmitter coil should be activated. In what refers to the ML approach, it is identical to the ones presented before, apart from the fact that the training data is generated using LTspice simulation tool. Nevertheless, it is also worth noting that the input variables corresponded to the first five harmonic current components and the RMS value of the current that flows in the transmitter coil. Regarding the target variables, the output power, the load resistance and the coupling coefficient were the candidates to be estimated individually. To reach the best performance possible ML regression models like random forest, decision tree, support vector machine, adabooster with decision tree and XGboost were tested, because in this particular scenario, the authors found ML models to be more suitable than NNs or DL models, primarily due to the limited information available in the dataset, which posed challenges for training more intricate networks. The training set was composed by measurements of the input variables, concerning the admissible airgap and misalignment distance. The profile between the output power and the input current presents two visible regions, being one of them where the output power is directly proportional to the input current (region where the transmitter pad should be turned on) and the other one where the output power drops drastically with the decreasing of the input current (region where the transmitter pad should be turned off). Referring to the coupling coefficient and load resistance estimation, a frequency domain approach took place.

[4]number of trees in the forest (small value of $ntree$ increases the models error and a large value increases computing time and memory consumption).

[5]minimum sample size of split neurons which it can limit the conditions for further division of sub-trees.

As input data of coupling coefficient estimator model, the amplitude and phase of the fundamental component and third harmonic components of the input current, the RMS value of the input current as well as the estimated output power were considered. Consequently, each feature impact was analysed. To achieve this, three distinct cases were considered, where in each case the skit-learn random forest regression algorithm was used to find the features that had the greater impact in the model training [61]. It was concluded that the estimated output power had the highest importance in all the cases and also that the higher the number of features the best the model will perform. To estimate the load resistance, a similar approach was introduced, however, it was added to the input data a new feature, the estimated coupling coefficient. In this case the amplitude of the third harmonic component of the input current had the greater influence in training of the model. Analysing the results, the random forest algorithm was the best predicting the output power with an average accuracy of 88%. Conversely the adabooster with decision tree was the best performing regression model estimating the load resistance and coupling coefficient, with accuracies of 88% and 92%, respectively. A comparison between the actual and predicted values of these variables is illustrated in figure 2.14. This ML model had also the best estimation performance regarding the position of the receiver.

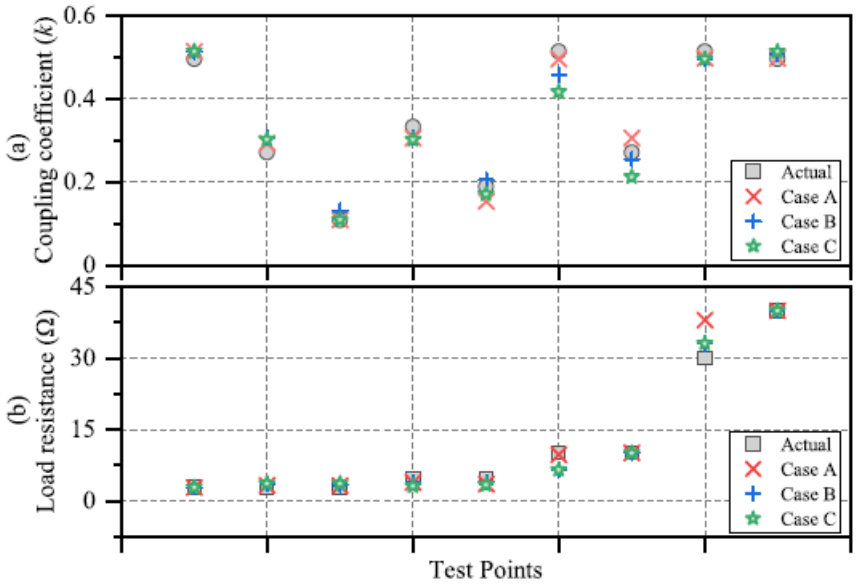

Figure 2.14: Actual and predicted 2.14a coupling coefficient and 2.14b load resistance for different test points from adabooster with decision tree model [34].

Regarding the mutual inductance estimation, in [49] is proposed a random forest regression model, where the input parameters are the amplitude of the fundamental component, third, fifth and seventh harmonics of the current and voltage of the transmitter side, which were measured at the resonant frequencies, which limited the utility of the model to only during the power transfer process. Equally to previous citations, the data went through a preprocessing phase where bad data was eliminated and the remaining was normalized. The quality factor of the model and the RMS errors of the estimated mutual inductance over the average mutual inductance were the metrics chosen by the authors to analyse the model performance. The parameters of the model were tuned regarding its performance. Consequently,

the obtained average estimation error and standard deviation of the estimation error were equal to 2.55% and 4.04%, respectively.

Conversely, in order to maximize the efficiency tracking of a wireless power transfer system due to the existence of situations of low load receiving efficiency, in [50] it is proposed a random forest regression model to predict and stabilize the variable load impedance by also predicting the proper resonant frequency for each situation. Regarding the collection of data phase, the authors implemented a variable load circuit where to change the impedance it was only needed to modify the duty ratio and the reactance of the controller. Typically, when a misalignment between the transmitter and receiver pads occurs, the reflected impedance form the secondary side will affect the parameters of the primary side, resulting in drift of the resonance and natural frequencies. The features chosen by the authors relied on the receiver voltage, input power, output power, coil distance, receiver frequency and the actual impedance change of the circuit, which in the majority of the cases would be difficult to obtain. In what the validation of the model is concerned, the conclusions of the authors were not objective which made the analysis of the results difficult to interpret, although it was observed that the impedance prediction was fairly accurate.

Furthermore, ML models can likewise be implemented with the goal of predicting the receiver position in a system with multi-transmitters in order to control the switching criterion of the transmitter pads [51]. However, due to some punctual limitations like determining the longitudinal displacement of the receiver pad so that the transmitter pad could work as intended, two ML models were proposed to estimate this value and subsequently compared regarding their performance. The input data for both ML models consisted on the distance between the pads, the current of the primary side and also the efficiency of the system. These data was collected through ANSYS and MATLAB simulations, regarding a previously established interval of values for each variable. One ML model was a back propagation (BP) algorithm. The proposed structure was a network containing an input layer, a hidden layer and an output layer, with 3, 11 and 1 neurons, respectively, each of them composed by a *sigmoid* activation function. The second purposed ML algorithm was a support vector regression (SVR), however during the tuning of this model, particular attention was taken to some parameters like the kernel function, in order to avoid problems concerning data calculation. Therefore, a radial basis function (RBF) was chosen. By analysing the performance of these models in simulation environment, the estimation accuracy as well as the relative error presented acceptable results, which meant that all the necessary conditions to the transmitter pads reach the optimal working mode were gathered. Referring to the experimental verification, it was verified the existence of an interval of values where the estimation was not as accurate as pretended, so there was the need to increase the density of the training data. With this modification the obtained results were promising, getting an error reduction of approximately 50%. When the switching control was applied, the efficiency of the system was around $90\pm2\%$, which resulted on an increase of 10% compared with the situation without switching control. Thus, it was demonstrated that the system operates in resonance before and after the switching, validating the analysis made previously.

Further addressing the misalignment estimation in dynamic wireless power transfer systems, in [52] it is proposed a magnetic field-based method to achieve this

objective. It can be asserted that ANNs, although was one of the first conceived AI models, it continues to deliver good performance for a wide range of WPT applications which was the reason why the authors employed it. The proposed system consists in an EV that is equipped with four sensing coils, including the main receiver coil that is attached under the center of the EV. Essentially the three remaining coils are placed under the front bumper and as the EV moves they will measure the magnetic field produced by the transmitter pads and afterwards misalignment is estimated based on the voltage induced in each sensing coil. An illustration of this WPT in particular is presented in Figure 2.15.

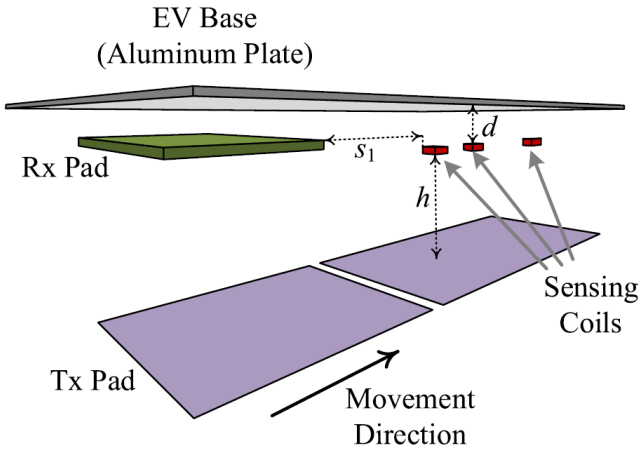

Figure 2.15: Three-dimension view of the relative position between the EV chassis, Rx pad, sensing coils, and transmitter pads [52].

The variation of the three components of the magnetic field regarding the misalignment was tested and it was observed that the B_y field component was the most reliable to generate a more accurate lateral misalignment estimation. In Figure 2.16 is displayed the characteristic of the variation of the B_y field component under misalignments.

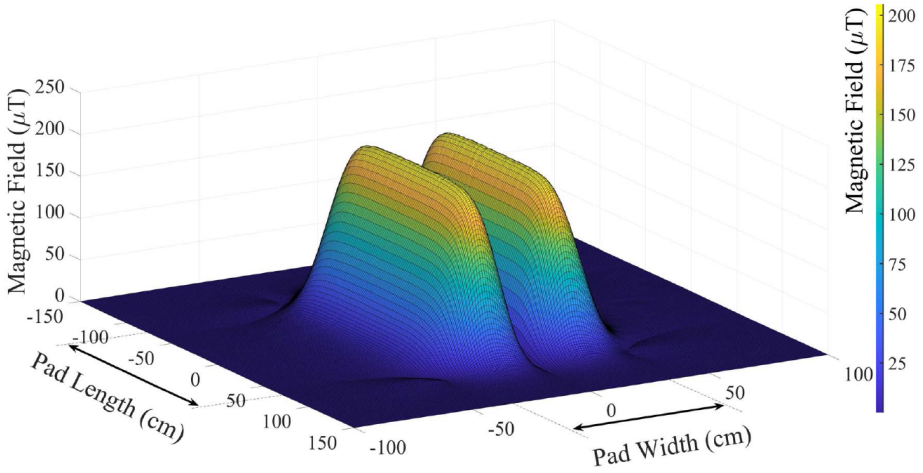

Figure 2.16: Three-dimension view of the magnetic field flux density above a transmitter pad [52].

The proposed approach was divided in to five distinct sections:

1. **Sensing:** Composed by the four sensing coils that measure the magnetic field.
2. **Filtering:** Due to the existence of switching harmonics emitted by the high frequency inverter.
3. **Sampling:** Using a TMS320F28027 microcontroller, the rms values of four signals are sampled.
4. **Processing Communication:** In this section it was chosen to employ a Raspberry Pi to perform the ANN calculations.
5. **Communication:** After the calculation of the misalignments, the communication is established using two-wire CAN communication.

The proposed ANN has three layers, one input layer that corresponds to the signals from the three sensors, a hidden layer with 4 neurons and a output layer that consists on the lateral and vertical misalignment values. It is worth mentioning that the structure of the network is suppose to be simple since it will make predictions in real-time while the EV is moving. The achieved results were promising for the reason that the estimation of the lateral and vertical misalignment had an error of approximately 1.9% and 3.8%, respectively.

It is also possible to estimate the lateral misalignment of the receiver pad via the utilization of the information from the DC-link current. In [53], it was recognized a pattern in a specific region which implied that the lateral misalignment of the receiver pad decreases the profile of the DC-link current. Also, by increasing the current from the transmitter side it was verified that it is possible to compensate the decrease of energy transferred with the misalignment. Therefore a time-series ANN was implemented to estimate the value of the lateral misalignment based on this statement. For implementation purposes, the considered RMS value of the current from the transmitter side was 70 A in a perfectly aligned condition. Additionally, two sensors were placed in the front of the transmitter pad in order to estimate the vehicle speed while enabling the controller to energize the same pad at the right moment with the reference current of 70 A. Basically, the controller has to detect a null-point of current. When this point is passed, the trained ANN starts receiving the data sampled of the DC-link current. Depending on the dimension of the region where the pattern was recognized, the ANN will only have that window margin to output a value of lateral misalignment, which in a real-world scenario where the vehicle is moving at 17 km/h, equals to a window of 40 ms. The network was constituted by three layers. An input layer with the data samples from the DC-link current, the value of its integral and also the speed of the vehicle, a hidden fully-connected layer with 10 neurons and an output layer with the value of the lateral misalignment. It was concluded that the implementation of this model would result in a 32% improvement of transferred energy. Alternatively the authors could have opt to implement a LSTM network, that is a widely implemented DL model when it comes to time series tasks [62].

Concerning the possible applications of ANN in IPT systems, in [54] it is proposed a model that estimates the load, self-inductance of the transmitter and receiver side and mutual inductance between the coils based on the information from the input

current and the transmission distance of the system. This model consists in a five layer fully-connected NN. The first layer is the input layer where the features are fed into the network, the three following layers are hidden layers with 32, 64 and 32 neurons, respectively, and the fifth layer is referred to as the output layer where are produced the final predictions based on the computational operations performed in the hidden layers. To train the network, a random 80% of the extracted data was selected while the test phase was based on the remaining 20%. The results obtained were promising as the maximum identification error for the self-inductance, mutual inductance and load was of 0.08%, 2.66% and 2.45%, respectively.

Moreover, in [55] it is also compared the performance of two ML approaches. One is the random forest (RF) and the other is, like it was also presented in the previous citation, a DNN. Unlike the previous citation, that the charging platform was to be used on static conditions for automated guided vehicles [51], in this case it was studied in simulation environment the performance of the aforementioned ML models with one and two receiver pads, however the goal kept the same, i.e., maximize the power transfer efficiency by configuring the activation pattern of the different transmitter pads. Firstly, the authors opted to create an online receiver position estimator to predict, between a matrix of possibilities, the position of the pad. For this, the performance of the RF and the DNN models was compared. The RF algorithm was based on Scikit-Learn, regarding the input features. The output corresponded to one value from the given input matrix. Conversely, the DNN had the ability of predicting the exact coordinates of the receiver pad. In terms of structure, the best performing DNN was the one with four hidden layers, each with 512, 512, 512 and 256 neurons, respectively. Then, by deploying the generated data to an offline model, it was possible to obtain an activation pattern for the transmitter pads. The results with one receiver showed that both methods have good prediction accuracy, reaching values between 94% and 96%. On the other hand, the results with two receiver pads showed that the RF model fails to predict the receiver position correctly, apart from the DNN model that is able to predict the parameter accurately.

It can also be advantageous to implement AI in IPT systems with the goal of controlling the output power of the WPT system, mitigate the efficiency decline caused by impedance variations when physical displacement of the receiver pad happens [56]. To control the output power, first it was purposed a ML model with multi-nominal classification and softmax classification, with the purpose of estimation the coupling coefficient due to the fact that this is a crucial parameter regarding power variation. The training data for this model was acquired in a simulation environment. Subsequently, the system was implemented experimentally and the model of coupling coefficient estimation was deployed in a Raspberry Pi board. Under displacement situations, when inspecting the behavior of the output voltage, the ML model provided an improvement of 92.5% to stabilize its value in comparison to the typical voltage control.

Alternatively there are also proposals of AI implementation in IPT systems concerning the optimization of the magnetic coupling itself through the design of new structures of ferrite cores [57, 58].

This literature review on the estimation of different parameters of IPT systems revealed that a scientific basis have been established on this behalf. Self and mutual inductance, coupling coefficient, load resistance, position of the receiver pad,

power transfer and quality factor of the coils are examples of parameters that have been estimated through AI models. Typically, the AI implementation relies on ML models or ANNs. Although some authors refer to DNNs as models difficult to understand and hard to train due to the necessity of a large dataset, the capacity to adapt to highly non-linear situations, such as the estimation of mutual inductance, continues to be the reason why DL is considered the best approach. Moreover, to the best of the knowledge acquired, there has not been any approach that utilized harmonic components measured from the secondary side as training data. Normally, the training data relied on measurements from the transmitter side or even on structural parameters of the coils, which would be challenging to acquire in a real-world application. Additionally, the articles that purpose AI models for parameter estimation in a dynamic IPT system configuration are still highly affected by the speed of the EV. As so, this factor constitutes a significant barrier for the scientific community to overcome in order to enhance the performance of these estimation models. Nevertheless, establishing the proposed solution required overcoming various challenges. The initial simulation model was conceived with a resistance as the output. As one of the main objectives of this dissertation was to develop a robust AI model that could have potential to be used in a real-world scenario, it became necessary to modify the output configuration to grant the AI model access to a more realistic system behavior. However, since the objective of this dissertation was not the implementation and adjustment of an additional power electronic converter, it was decided to add a control system able to reproduce the best as possible, the behavior of a battery charger, based on parameters like the output voltage and pretended charging power. Since the results from this approach are not as accurate as those retrieved from a simulation model with a proper DC-DC converter and a battery pack implemented in the output of the system, these adjustments undoubtedly represent future improvements to pursue.

Chapter 3

IPT System under Analysis

The following chapter have the intent of introducing the object system of analysis as well as the AI model that was implemented to fulfill the established objectives. The chapter starts with the presentation of the IPT system configuration in detail, its characterization plus the sizing of the various elements of the circuit and their relationships. Further, in a section dedicated to the dataset generation and feature selection, it will be analysed the behavior of the system under different conditions which will actively contribute to the process of data collection and feature extraction.

3.1 IPT Power System

As the name suggests, this section has the purpose of presenting in detail the IPT system topology, including the equations that rule its electric circuit and also the procedures to collect the necessary data to train the AI model.

3.1.1 Series-Series-Series Topology

Following what was mentioned in Chapter 2, there are different possible configurations for resonant topologies of IPT systems. Thus, it is of great relevance to study of the equations that rule the different topologies available to comprehend the behavior of the IPT system under misalignment conditions. With this reasoning in mind, next it will be presented a detailed explanation why in this work a series-series-series topology was chosen over a simpler series-series topology.

Firstly, it is worth noting that, unlike the topologies presented in Figure 2.2, this configuration has two magnetic couplings instead of just one. By taking a closer look to a series-series topology circuit, presented in Figure 3.1 it is possible to verify that, at the resonance frequency, (3.1) corresponds to the secondary side impedance and (3.2) is referred to the reflected impedance on the primary side, which depends on several parameters like the number of turns of the transmitter and receiver coils, the distance between them and also the angle of the receiver coil.

$$Z_{sec} = j\omega L_r + \frac{1}{j\omega C_r} + R_{eq} \tag{3.1}$$

$$Z_{ref} = \frac{\omega_0^2 M^2}{R_{eq}} + j0. \tag{3.2}$$

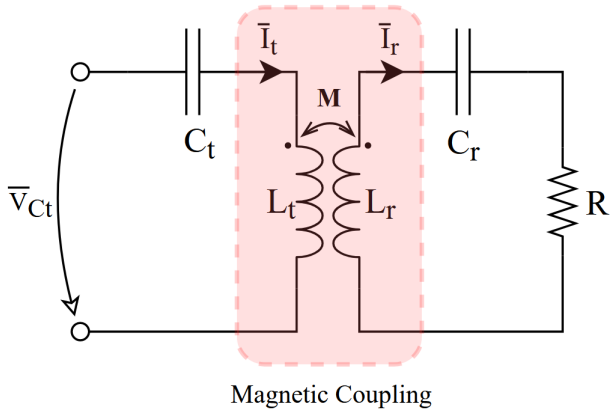

Figure 3.1: Series-Series topology.

In [5], a simulation model was developed to test the behavior of an IPT system with different resonant power converter topologies under misalignments. In Figure 3.2 is displayed the considered simulation circuit.

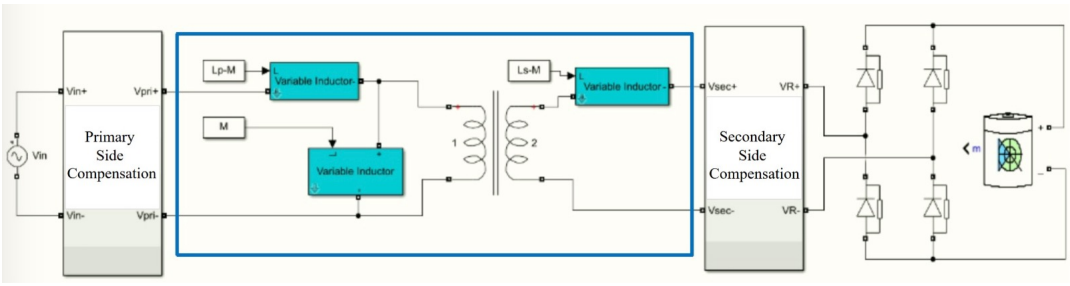

Figure 3.2: Series-series simulation circuit [5].

Moreover, the values of each element of the circuit are shown in Figure 3.3.

Parameter		SS	SP	PS	PP
Magnetic coupler	MC	$L_t = 363uH$; $L_r = 95.2uH$; $M = 100uH$			
	$C_r[nF]$	665.19			
Secondary capacitance	$C_t[nF]$	174.45	245.49	169.5	166.35
Source	$V_{in}[V]$	155.03	262.61	-	-
	$I_{in}[A]$	-	-	3.35	6.66
Output	All	$V_{out} = 250V$; $I_{out} = 10A$; $P_{out} = 2.5kW$			
Switching frequency	All	$f = 20kHz$			

Figure 3.3: Series-series simulation parameters [5].

Furthermore, to evaluate the behavior of the primary-side of the resonant converter in two limit conditions: no-coupling (absence of receiver) and full coupling (transmitter and receiver pads perfectly aligned), considering two different settings, charging and no-charging (fully-charged battery). Thus, three operating regions were selected:

- ◇ **Region 1:** The EV is approaching the transmitter pad, therefore the magnetic coupling is zero, i.e., $M = 0$.

◇ **Region 2:** The EV achieves perfect alignment with the transmitter pad, thus the mutual inductance reaches its maximum value. In this region the battery is in charging state.

◇ **Region 3:** In this case the battery is fully charged meaning that is in a no-charging state.

Focusing on the behavior of the series-series topology, Figure 3.4 it is presented the obtained results for the current that flows in the transmitter-side.

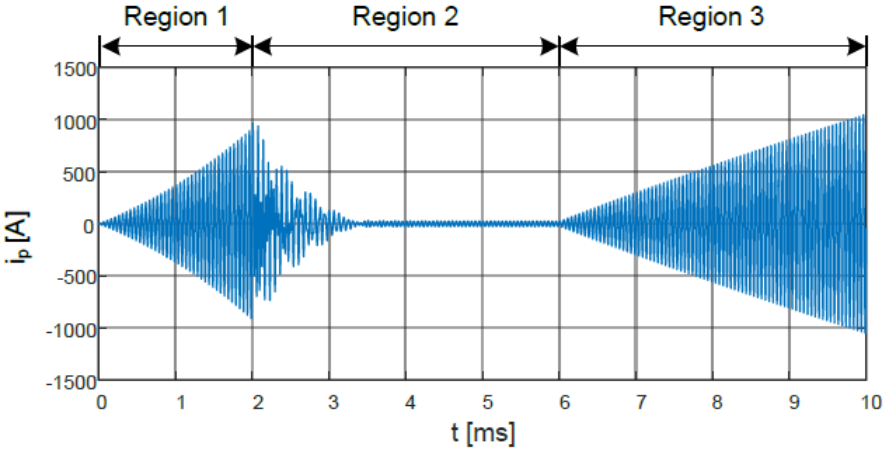

Figure 3.4: Series-series topology transmitter-side current for different operating conditions [5].

By observing Figure 3.4 it is clear that the current in the transmitter-side tends towards infinity when in a no-coupling condition. This phenomenon occurs due to the reflected impedance that approaches zero in this condition. As a result, the input impedance of the circuit becomes very low, since it corresponds to a series between an LC circuit and the resistive component of the inductor wire. Thus, although in a real-world scenario it would contribute to a weight gain, it was necessary to prevent the current of the transmitter-side from increasing without bound, leading to the introduction of an additional magnetic coupling before the transmitter pad.

Subsequently, the series-series-series topology will be presented in detail next [10][63]. To accomplish this, Figure 3.6 presents the equivalent circuit of the topology used.

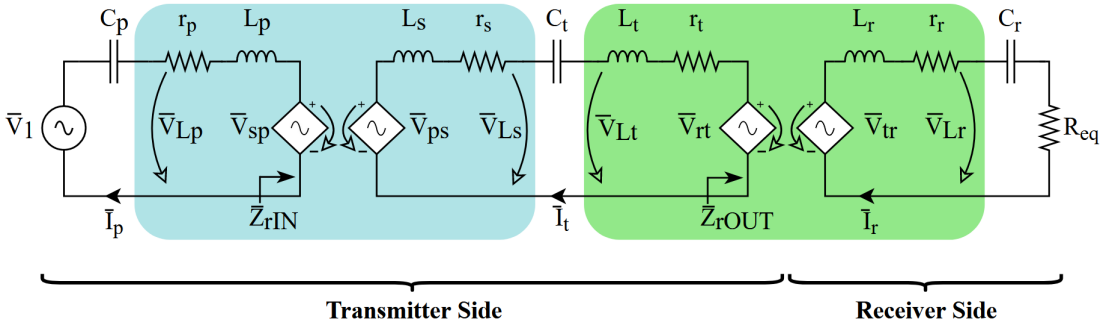

Figure 3.5: Equivalent circuit of a SSS IPT system - adapted from [63].

The letters attributed to each variable intend to indicate the zone of the system it relates to. Letters p and s refer to the first magnetic coupling, including the

associated resonant tanks, whereas letters t and r are related to the second magnetic coupling also including the elements of the resonant compensation. Thus, L_p, L_s, L_t and L_r are referred to the self-inductances of the respective magnetic coupling, the capacitors of each resonant tank are represented as C_p, C_t and C_r. Additionally, r_p, r_s, r_t and r_r denote the equivalent resistance of the inductors of the respective magnetic coupling and R_{eq} represent the equivalent resistance of the rectifier together with the batteries and corresponding charger.

In this configuration, if the on-board converter is operating continuously, the output voltage of the high frequency inverter, represented in Figure 3.6

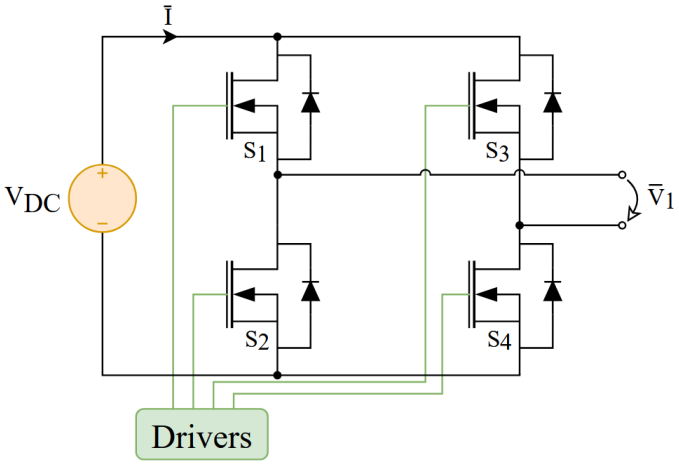

Figure 3.6: H-bridge high frequency inverter - adapted from [10],

can be replaced by its fundamental component (FC), $\overline{V}_1$, where its RMS value can be given by:

$$|\overline{V}_1| = V_{DC}\frac{2\sqrt{2}}{\pi}cos\left(\frac{\alpha}{2}\right), \tag{3.3}$$

where α corresponds to the phase shift control angle established by the drivers and V_{DC} is the average DC link voltage. Alternatively, by applying the Kirchoff laws it can be obtained the voltage equations of each mesh of the IPT circuit:

$$\overline{V}_1 = r_p \cdot \overline{I}_p + j \cdot w\left(\left(L_p - \frac{1}{w^2 \cdot C_p}\right)\overline{I}_p - M_{ps} \cdot \overline{I}_t\right) \tag{3.4}$$

$$0 = (r_s + r_t) \cdot \overline{I}_t + j \cdot w\left(\left(L_s + L_t - \frac{1}{w^2 \cdot C_t}\right) \cdot \overline{I}_t - M_{ps} \cdot \overline{I}_p - M_{tr} \cdot \overline{I}_r\right) \tag{3.5}$$

$$0 = (R_{eq} + r_r) \cdot \overline{I}_r + j \cdot w\left(\left(L_r - \frac{1}{w^2 \cdot C_r}\right) \cdot \overline{I}_r - M_{tr} \cdot \overline{I}_t\right), \tag{3.6}$$

where L_{ps} and L_{tr} correspond to the mutual inductance between the transmitter and receiver of the first and second magnetic coupling, respectively, w_p, w_t and w_r are the natural angular frequencies of the resonant tanks.

To complete the characterization of the circuit, by solving the mathematical expressions previously presented, it is possible to deduce the equations that rule the behavior of the current in each mesh of the circuit.

$$\overline{I}_p = \frac{\overline{V}_1}{Z_p + Z_{rIN}} \tag{3.7}$$

$$\overline{I}_t = \overline{I}_p \frac{j \cdot w \cdot M_{ps}}{Z_t + Z_{rOUT}} \tag{3.8}$$

$$\overline{I}_r = \overline{I}_t \frac{j \cdot w \cdot M_{tr}}{Z_r + R_{eq}}. \tag{3.9}$$

For simplification purposes, the equivalent impedances of each resonant tank, in (3.7), (3.8) and (3.9) were replaced by variables Z_p, Z_t and Z_r, respectively, thus obtaining:

$$Z_p = r_p + j \cdot w \cdot L_p \left(1 - \frac{w_p^2}{w^2}\right) \tag{3.10}$$

$$Z_t = (r_s + r_t) + j \cdot w \cdot (L_s + L_t) \left(1 - \frac{w_t^2}{w^2}\right) \tag{3.11}$$

$$Z_r = r_r + j \cdot w \cdot L_r \left(1 - \frac{w_r^2}{w^2}\right). \tag{3.12}$$

Besides the equivalent impedances of each resonant tank, there is also the reflected impedance of one side of the magnetic coupling referred to the other side. In (3.7), (3.8) and (3.9), these were expressed as Z_{rIN} and Z_{rOUT}, where Z_{rOUT} corresponds to the reflected impedance from the receiver side into the transmitter side, while Z_{rIN} represents the reflected impedance of the secondary side of the first magnetic coupling into its primary side.

$$Z_{rIN} = \frac{\overline{V}_{sp}}{\overline{I}_p} = \frac{w \cdot M_{ps}^2 (Z_r + R_{eq})}{Z_t (Z_r + R_{eq}) + w^2 \cdot M_{tr}^2} \tag{3.13}$$

$$Z_{rOUT} = \frac{\overline{V}_{rt}}{\overline{I}_t} = \frac{w^2 \cdot M_{tr}^2}{Z_r + R_{eq}}. \tag{3.14}$$

3.1.2 Simulation Model

The complete IPT system under analysis was implemented in Simulink. The simulation model is presented in Figure 3.7, where the first magnetic coupling is referred to as an isolation transformer because in reality it isolates the primary side from the effect of the reflected impedance from the secondary-side, as explained in section 3.1.1.

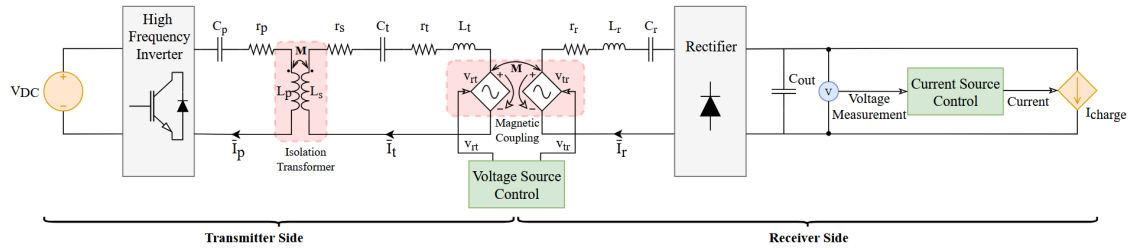

Figure 3.7: Simulation model of the series-series-series IPT system under analysis.

Just like with any other electrical circuit, the parameterization of the elements of a IPT system is crucial as it will be explained subsequently. Therefore, Table 3.1 represents the system specifications of the most relevant elements of this circuit.

The operation of the circuit at the resonance point is dependent on the parameterization of the reactive elements of the circuit. Thus, considering that the

Table 3.1: Simulation Parameters.

Parameter	Value
T_s	0.1 μs
V_{DC}	100 V
f	20 kHz
V_{ak}	0.700 V
L_p	41.780 μH
L_s	42.290 μH
L_t	45.750 μH
L_r	60.200 μH
M_{ps}	30.270 μH
M_{tr}	16.680 μH
C_p	1.516 μF
C_t	0.720 μF
C_r	1.052 μF
C_{out}	6400 μF
$r_{p,s,t,r}$	0.100 Ω

values of the self-inductance of each coil were measured, (3.15) allows to calculate the values of the capacitors and guarantees the operation of the circuit in this condition [11][63, 64].

$$f = \frac{1}{2 \cdot \pi \sqrt{L_p \cdot C_p}} = \frac{1}{2 \cdot \pi \sqrt{(L_s + L_t) \cdot C_t}} = \frac{1}{2 \cdot \pi \sqrt{L_r \cdot C_r}}. \tag{3.15}$$

Additionally, the value of the capacitor, C_{out}, was increased until the overshoot of the output voltage did not surpass 2-3% of the value in steady state.

Another essential topic that needs coverage is the method through which was possible, in simulation environment, to define the variation of the mutual inductance of the second magnetic coupling, based on real-world measurements. The first magnetic coupling, based on its purpose, is referenced to as an isolation transformer, so the mutual inductance is kept constant. As represented in Figure 3.7, the magnetic coupling between the transmitter and receiver coils was replaced by two controlled voltage sources. In Simulink, these blocks can generate a voltage that is driven by an input signal. Considering v_{rt} and v_{tr} as the imposed voltage to the primary and secondary side, respectively, the control inside the subsystem "Voltage Source Control" has the function of guaranteeing the following conditions:

$$v_{rt} = -L_{tr} \cdot \frac{di_r}{dt} \tag{3.16}$$

$$v_{tr} = L_{tr} \cdot \frac{di_t}{dt}, \tag{3.17}$$

which entails knowing the mutual inductance value.

In the pursuit of acquiring the needed data, ensuring a reliable source, i.e., a realistic representation of the IPT system in a simulation environment, an existing prototype of the system was used. It is constituted by a medium density fiberboard (MDF) structure, a stepper motor, and a screw thread shaft connected to the motor, which enables the movement of a platform housing the receiver pad. The stepper motor was controlled by Mach 3 software which was developed by Newfangled Solutions LLC. This allowed to define, with increments of 10mm, the longitudinal position of the receiver pad within an interval spanning from -250 mm and 250 mm from the center of the transmitter pad. The horizontal position of the platform of the transmitter pad was adjusted manually, between 0 mm and 175 mm, with increments of 25 mm. There was also the possibility of adjusting the airgap between the transmitter and receiver pads within the range of 48 mm and 108 mm with increments of 20 mm. Additional information about the prototype and its components is depicted in Appendix A.

Thus, by using an LCR meter, i.e., an electronic device designed for measuring inductance (L), capacitance (C) and resistance (R), the self-inductance of the transmitter pad (L_t), the self-inductance of the receiver pad (L_r), as well as the total inductance obtained through the series (L_{T+}) and anti-series (L_{T-}) connections, were measured. Figure 3.8 illustrates the connections established for measuring these parameters.

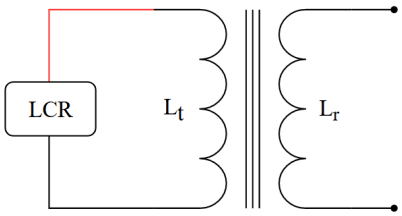

(a) L_3 measurement connections

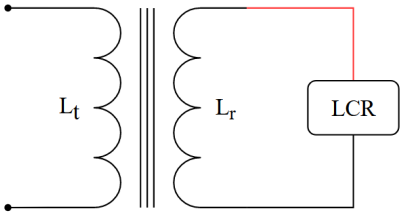

(b) L_4 measurement connections

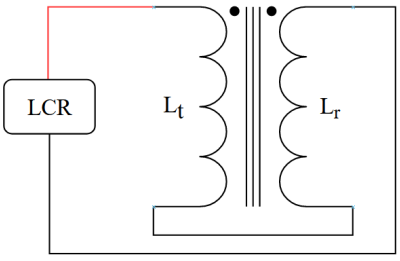

(c) L_{T+} measurement connections

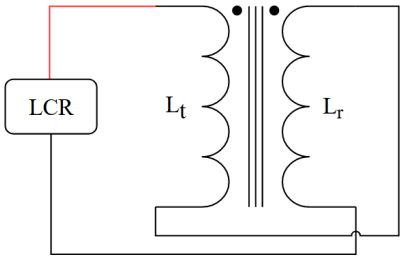

(d) L_{T-} measurement connections

Figure 3.8: Self inductance and total inductance measurement connections.

Consequently, by employing (3.18) and (3.19), it was possible to obtain the values of the mutual inductances, M_+ and M_-, which were calculated through different associations of the coils for each chosen position of the pads [9].

$$M_+ = \frac{L_{T+} - L_t - L_r}{2} \tag{3.18}$$

$$M_- = \frac{L_t + L_r - L_{T-}}{2}. \tag{3.19}$$

Theoretically, the values of M_+ and M_- are expected to be identical. However due to potential imprecisions from the measurement device, or slight variations in the positioning during the measurements, there were some discrepancies in the experimental results. As such, the determining factor for choosing one curve over the other was based on selecting the curve with fewer negative values at its extremity.

Consequently, upon gathering all the measurements within the regions of interest, a comprehensive three-dimensional table was constructed, encompassing the values of mutual inductance which resulted in the plot observed in Figure 3.9.

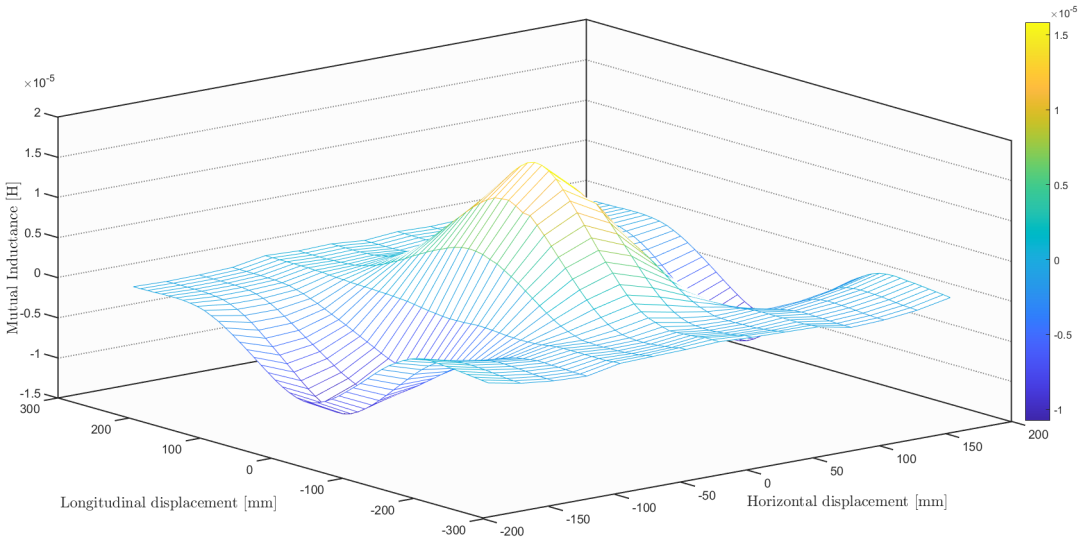

Figure 3.9: Mutual inductance for an airgap of 48 mm.

This data was subsequently given as input to a Simulink lookup table block, enabling the possibility of extracting the mutual inductance value for any given point of interest, considering the range of values available. This block performs n-dimensional interpolation using one of various algorithms available. Considering the characteristic of the curve presented in figure 3.9, notably, there are zones where it is suppose to exhibit a sine pattern, however due to the chosen increments it can be observed a flattening effect. Consequently, the cubic spline algorithm demonstrated a more subtle variation of mutual inductance between points so it was deemed the suitable choice for this work.

Finally, in order to emulate the output of a conventional battery charger, a controlled current source was integrated into the system. A block diagram of this control system is displayed in Figure 3.10.

The imposed current consider as a factor the power output of the charger. This allows the output current to adapt according to the power demand, guaranteeing that the output of the system aligns with the characteristics of a standard battery charger in a current control stage, which is the first stage when charging a discharged battery.

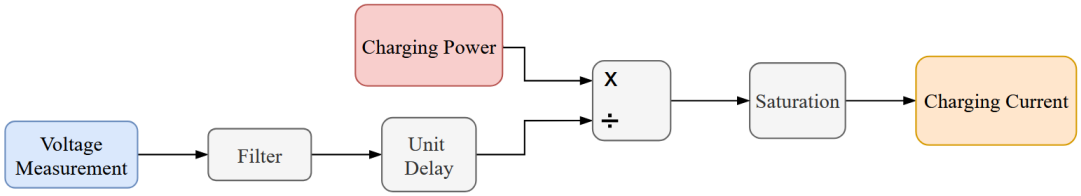

Figure 3.10: Block diagram of the control system of the "current source control" block.

3.2 Dataset Generation and Feature Selection

Considering the process of dataset generation and feature selection a careful analysis of the IPT system was carried out in this section. This analysis encompassed the verification of both the operation limits of the IPT system and the measured variables that fulfilled the requirements for successfully estimate the value of mutual inductance. Given the characteristics of the simulation circuit, the AI model must be capable of estimating accurately the value of mutual inductance under misalignment and charging power variations. Furthermore, it will be presented the normalization process of the acquired data.

3.2.1 Dataset Generation

The transmitter and receiver coils were assembled with the same 280 mm of width and 195 mm of length. Recapping what was stated in subsection 3.1.2 regarding the operation of the system, the output current is dependent on the output voltage and the charging power defined by the user. Hence, to set up the group of the admitted misalignment positions, referred in this document as grid of misalignments, two criteria must be met:

1. Ensuring a higher number of misalignment positions in regions where the mutual inductance has a non linear characteristic in order to accurately test the performance of the AI model.

2. The boundaries of the grid are based on the operation limits of the IPT system.

The control system of the output current was developed to emulate the behavior of a back-end DC-DC converter where the value of charging power established by the user is maintained constant independently of the level of misalignment. Therefore, the referred boundaries were established based on the behavior of the output current, since this parameter is dependent on the charging power chosen by the user and output voltage that will be directly proportional to the mutual inductance between the magnetic couplers [15]. This means that, when the transmitter and receiver pads are misaligned a decrease on the output voltage will be verified. Thus, in conditions where it is required a high value of charging power and the vehicle is considerably misaligned the system may not operate properly. Subsequently, it was determined that, since the output voltage was the only parameter that could be constrained in order to guarantee a minimum of 500 W of charging power at the position of greater misalignment, the limit positions would need to be selected accordingly. Besides, an additional criteria to have in account is the fact that, theoretically, the behavior of the mutual inductance is symmetrical, regarding the direction of the misalignment

[15], thus it is only necessary to extract measurements from misalignment positions in one quadrant. Considering that m_x is the horizontal misalignment and m_y is the longitudinal misalignment, the grid was formed by:

- $m_x = [0, 2, 4, 6, 8, 10, 12.5, 15, 20, 30, 40, 50]$;
- $m_y = [0, 5, 10, 15, 20, 25, 30, 35, 40]$;

The considered misalignment positions are illustrated in Figure 3.11 where in the positions of perfect alignment and greater misalignment it was measured a mutual inductance of 15.83 μH and 5.5 μH, respectively.

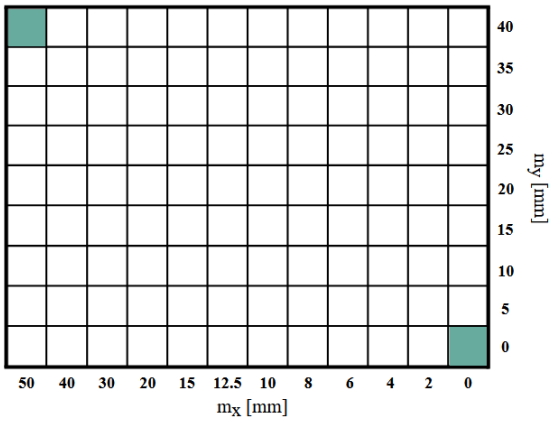

Figure 3.11: Grid of misalignment positions.

3.2.2 Feature Selection

Feature extraction, also called Feature Engineering [65], is certainly one of the most important procedures to achieve high performance AI models, since essentially, consists on extract relevant information from raw data [66]. Since this work consists on the development of an AI model to predict the value of mutual inductance, the goal is to find the most suitable parameters, i.e., features, for training the AI model and, consequently, predict the target variable (mutual inductance). Therefore, there are some criteria to have in account. Firstly, the chosen features must have a pronounced variation when a misalignment occur and secondly the opposite must happen when the charging power varies. This means that this model must be able to predict the mutual inductance value as accurately as possible for all the misalignments within the grid and also under all the allowed charging powers.

On account of being in a simulation environment, it is simple to include measuring sensors in the circuit. Figure 3.12 shows the points on the circuit where voltages and currents were measured.

With this information settled, one of two procedures was possible:

1. Use waveform data, i.e., the waveforms of signals to extract relevant features to train the AI model.

2. Use data from the harmonic components of voltages and currents, since there are various reactive components in the circuit.

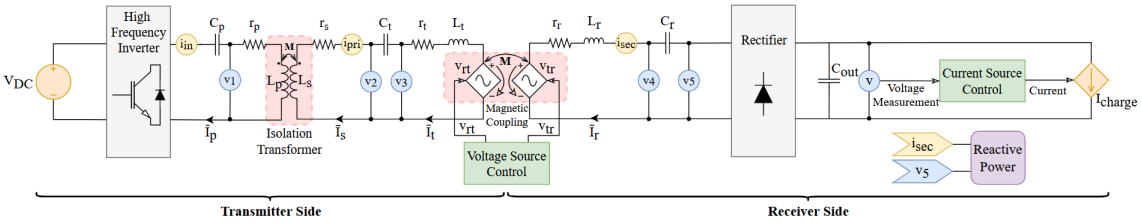

Figure 3.12: Measuring points in the simulation model implemented.

The method applied for features analysis consisted essentially on extract data from different positions of misalignment and under different charging powers. All the data management was done using MATLAB.

Waveform Analysis

To examine potential features from the waveforms of the measured signals in the circuit, data was extracted under the following conditions:

◇ Misalignment positions:

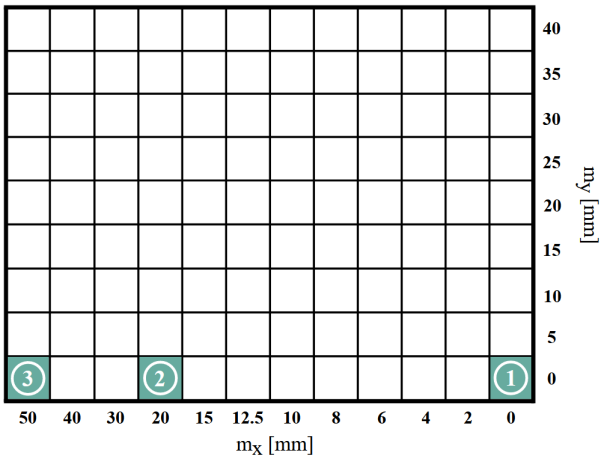

Figure 3.13: Considered misalignment positions.

From the available grid of misalignments, the three positions illustrated in figure 3.13 were selected. The choice was based on the fact that horizontal misalignments can provide a more pronounced insight into the variation of mutual inductance when compared to longitudinal misalignments, which do not induce as significant variations.

◇ Charging Power: 100 W, 200 W, 300 W, 400 W, 500 W.

The analysis of the waveforms took place in a incipient phase of the work, as such, a lower set of charging powers was initially tested.

After extracting the data, an analysis of the waveforms referred to the variables measured in the circuit was conducted. With the information retrieved from these possibilities it was possible to formulate an idea of the operation of the system under low and high charging powers due to the reproducibility of behavior of the system. The transmitter side measurements indicated one of two possibilities. On one side, the amplitude of the waveform increased with both misalignment and charging power, as observed in case of voltage v_1. On the contrary, although this phenomenon was anticipated due to the operation conditions of the SSS topology, the amplitude of the waveform of current i_{pri} remained constant despite the misalignment and charging power variations, which is not the intended behavior for the required features. In Figure 3.14 and Figure 3.15 this can be verified by observing the waveform of voltage v_1 and current i_{pri} under misalignment and charging power variations, respectively.

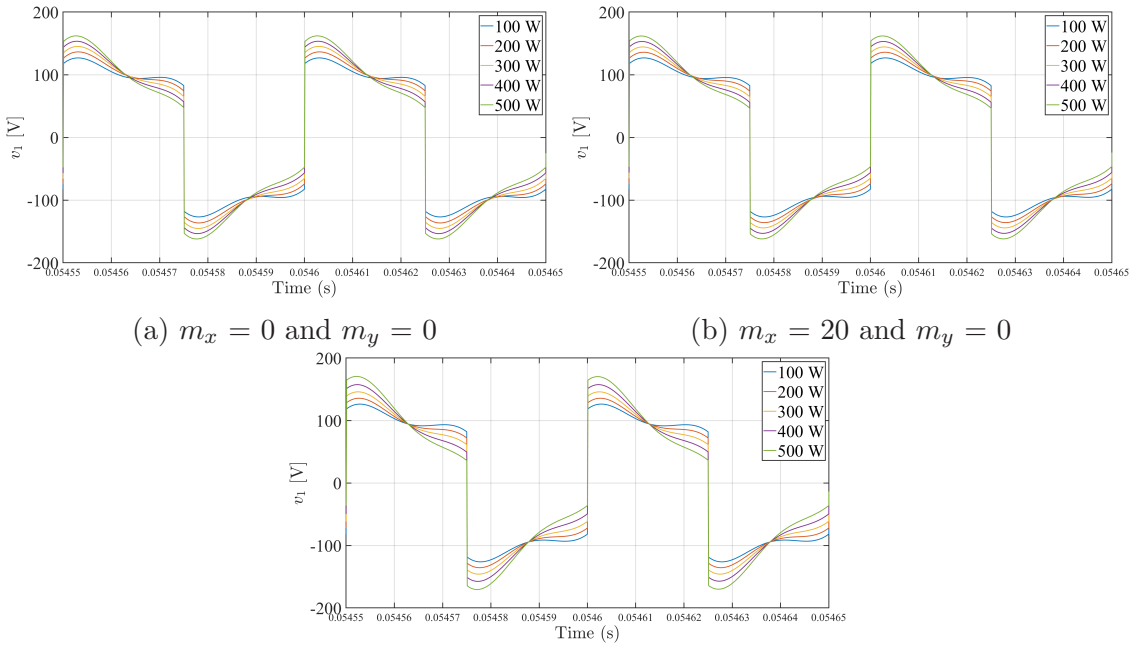

(a) $m_x = 0$ and $m_y = 0$

(b) $m_x = 20$ and $m_y = 0$

(c) $m_x = 50$ and $m_y = 0$

Figure 3.14: v_1 waveforms under charging power variations in position 1 (3.14a), 2 (3.14b) and 3 (3.14c).

The measurements of the secondary side demonstrated an identical behavior in the way that all waveforms changed its amplitude with both misalignment and charging power variation. Figure 3.16 illustrates the waveform of the voltage v_5 under misalignment and charging power variations.

Observing figure 3.16a and 3.16b in detail it can be verified that for low charging powers, namely, 100 W, 200 W and 300 W there is some voltage drops. Therefore, these results contributed to reach the conclusion that the waveforms are not reliable as features of this IPT system.

As an enlightenment, since the AI models that are more frequently used and offer the best results when analysing waveforms patterns are the LSTM networks, its choice is not suitable for this work. In what wireless charging is concerned, this type of networks have been applied mostly to detect foreign objects [67, 68].

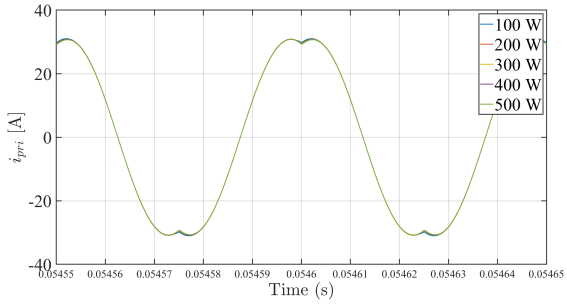

(a) $m_x = 0$ and $m_y = 0$

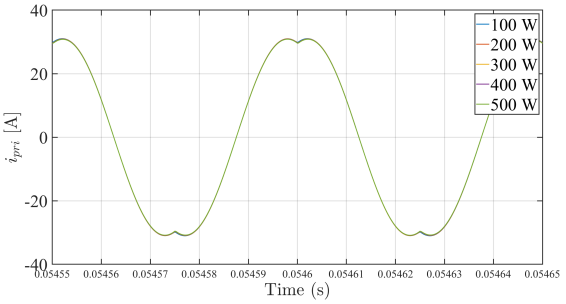

(b) $m_x = 20$ and $m_y = 0$

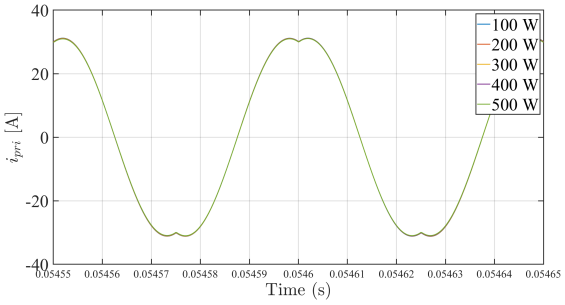

(c) $m_x = 50$ and $m_y = 0$

Figure 3.15: i_{pri} waveform representation under charging power variations in position 1 (3.15a), 2 (3.15b) and 3 (3.15c).

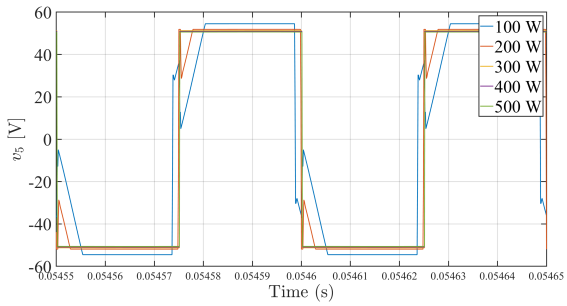

(a) $m_x = 0$ and $m_y = 0$

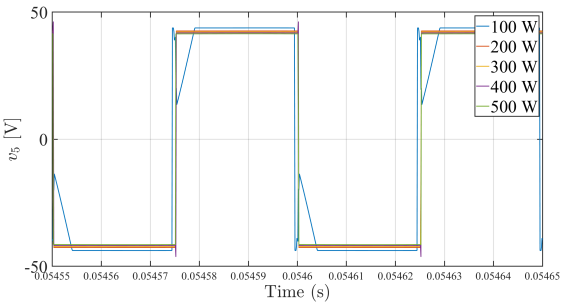

(b) $m_x = 20$ and $m_y = 0$

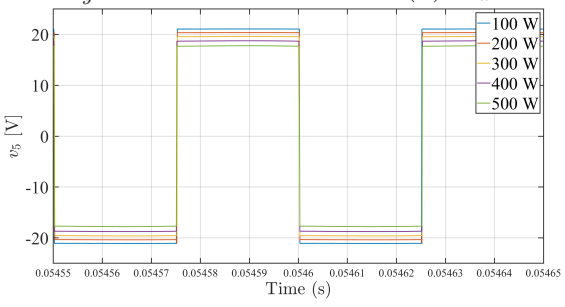

(c) $m_x = 50$ and $m_y = 0$

Figure 3.16: v_5 waveform representation under charging power variations in position 1 (3.16a), 2 (3.16b) and 3 (3.16c).

Amplitude of Harmonics

To make this analysis as succinct as possible, the data was extracted under the following conditions:

- ◇ Misalignment: The same positions as displayed in Figure 3.13.
- ◇ Charging Power: 500 W, 1000 W, 1500 W, 2000 W, 2500 W, 3000 W.

The amplitude of the harmonics was obtained through a function implemented in MATLAB, that has as inputs the vector of the signal to be analysed and the time vector. With this information, the function outputs one vector with the frequency, one with the amplitude and other with the phase of the different components of the signal. Since the input signal do not have any imaginary component, the frequency vector that the function returns is comprehended between 0 and $F_s/2$ Hz, where F_s is the sampling frequency. To find the amplitude of the harmonics it was decided to use the flat top window, the particular reason that among all the windowing functions, it is the one that gives the real amplitude of the signal [69].

Moreover, it was decided to go up to 3000 W of charging power, since when the pads are approximately aligned, the system is able to deliver this power. Nonetheless, under these conditions, the process of selecting the most suitable harmonics as features for the AI model was divided in three main steps:

1. Compare the amplitude of the different harmonics, including the fundamental component, for the chosen charging powers;
2. Select the harmonic components that presented similar amplitude for all charging powers and had the greater influence, in terms of amplitude, in the signal under analysis;
3. Verify if the selected harmonic components exhibit a noticeable variation in a event of a misalignment occurrence and opt for those that demonstrate such variations. However, although the amplitude of some harmonic components is not the same across different charging power levels, the percentage variation for each charging power under misalignment variations exhibits a similar pattern.

In first place, it will be taken a closer look to the signals measured in the transmitter side followed by the signals measured in the receiver side. The conducted analysis revealed that the variations of the amplitude of the harmonics of some parameters is similar. Therefore, next it will be presented the variation of the amplitude of both fundamental and harmonic components under different charging power and misalignment values. Regarding the measurements of the transmitter side, it will be showcased the analysis referred to voltage v_3. Since for the transmitter side measurements, the results were similar, Appendix B.2 contains the analysis of the remaining parameters of the circuit.

Voltage - v_3

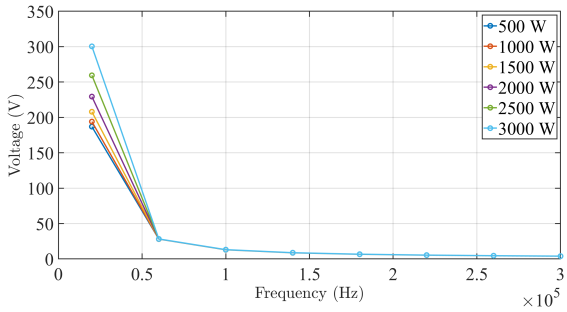

(a) $m_x = 0$ and $m_y = 0$

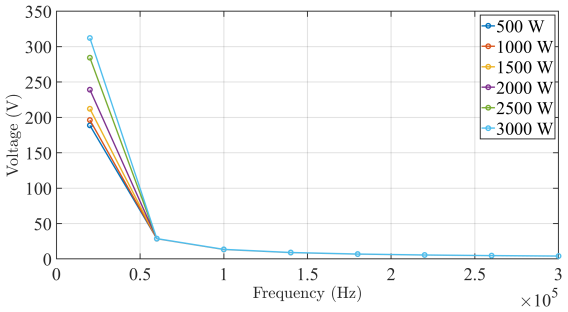

(b) $m_x = 20$ and $m_y = 0$

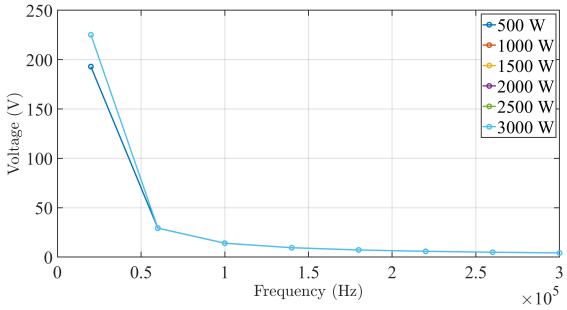

(c) $m_x = 50$ and $m_y = 0$

Figure 3.17: Representation of the amplitude of the fundamental component and higher-order harmonics components of voltage v_3 in positions 1 (3.17a), 2 (3.17b) and 3 (3.17c), respectively, under charging power variations.

From figures 3.17a, 3.17b and 3.17c, it can be observed a pronounced discrepancy of amplitudes regarding the fundamental component, which indicates that these parameter is not a good feature. Moreover, it was decided to analyse the behavior of the amplitude of the third and fifth harmonics, since the amplitude of the remaining higher-order harmonics is noticeably low.

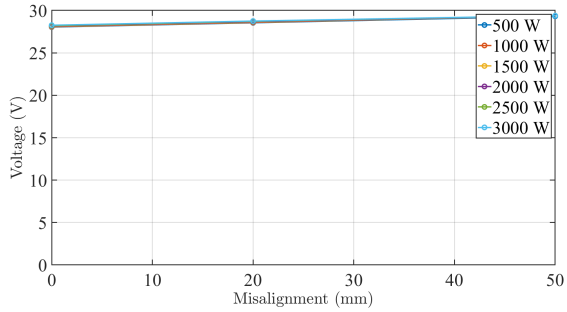

(a) Amplitude of the third harmonic

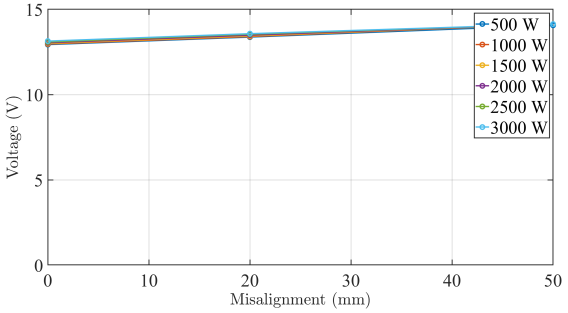

(b) Amplitude of the fifth harmonic

Figure 3.18: Representation of the amplitude of the third 3.18a and fifth 3.18b harmonics components of voltage v_3 under misalignment and charging power variations.

Figures 3.18a and 3.18b demonstrate that these parameters are also not potential features, due to the fact that they have a minor variation under misalignment situations. Therefore, the next step will involve an analysis of the signals referred to the receiver pad.

Voltage - v_4

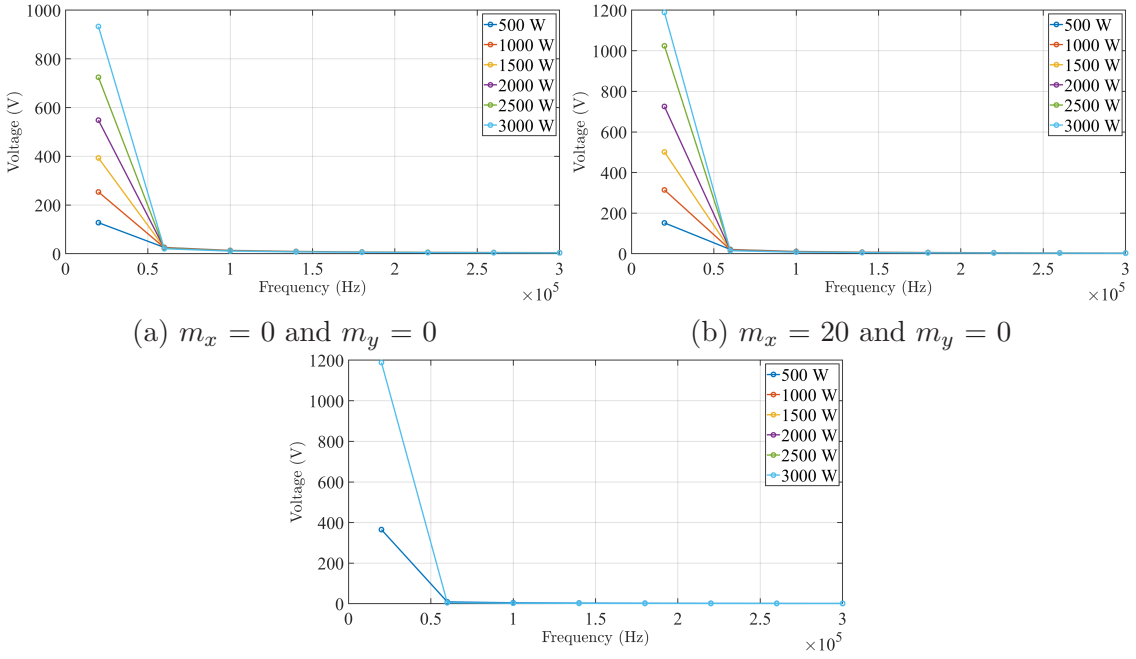

(a) $m_x = 0$ and $m_y = 0$

(b) $m_x = 20$ and $m_y = 0$

(c) $m_x = 50$ and $m_y = 0$

Figure 3.19: Representation of the amplitude of the fundamental component and higher-order harmonics components of voltage v_4 in positions 1 (3.19a), 2 (3.19b) and 3 (3.19c), respectively, under charging power variations.

Applying a similar analysis as the one made previously conduct to the fact that, considering the characteristic of the amplitude of the fundamental and higher-order harmonic components under charging power variations, the most suitable parameters are the amplitude of the third and fifth harmonics. Furthermore, figure 3.20 serves the purpose of depicting how these parameters react under situations of misalignment.

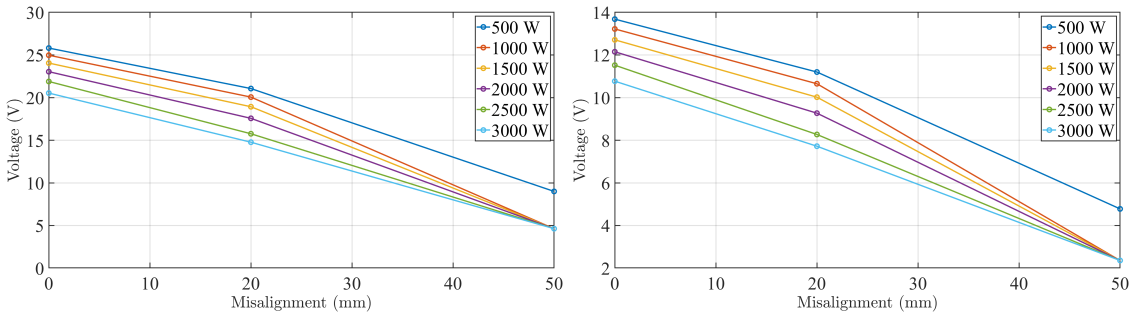

(a) Amplitude of the third harmonic

(b) Amplitude of the fifth harmonic

Figure 3.20: Amplitude of the third 3.20a and fifth 3.20b harmonic components of voltage v_4 under misalignment and charging power variations.

Figures 3.20a and 3.20b confirm that the amplitude of the third and fifth harmonics of the voltage v_4 meet the necessary conditions to be features.

Voltage - v_5

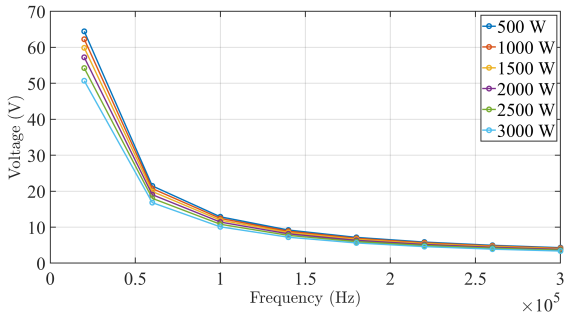

(a) $m_x = 0$ and $m_y = 0$

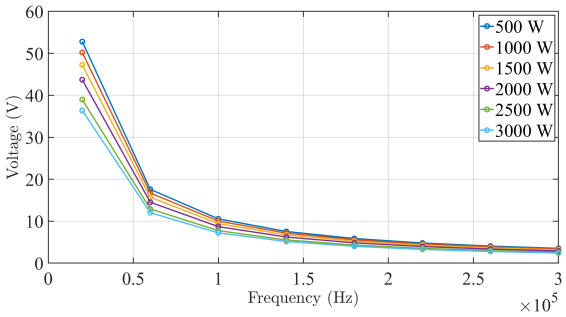

(b) $m_x = 20$ and $m_y = 0$

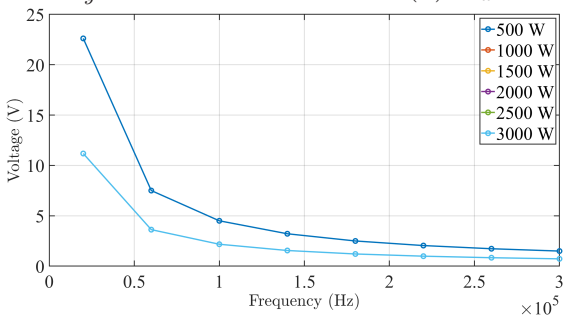

(c) $m_x = 50$ and $m_y = 0$

Figure 3.21: Amplitude of fundamental and higher-order harmonic components of the voltage v_5 in position 1 (3.21a), 2 (3.21b) and 3 (3.21c), respectively, under charging power variations.

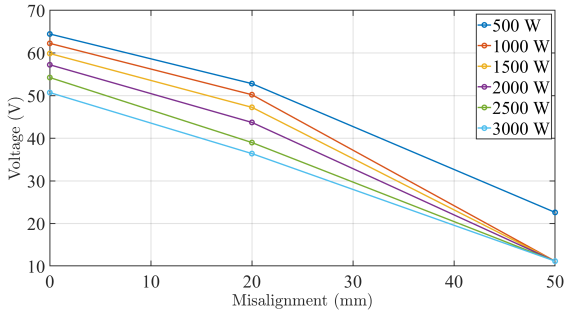

(a) Amplitude of the FC

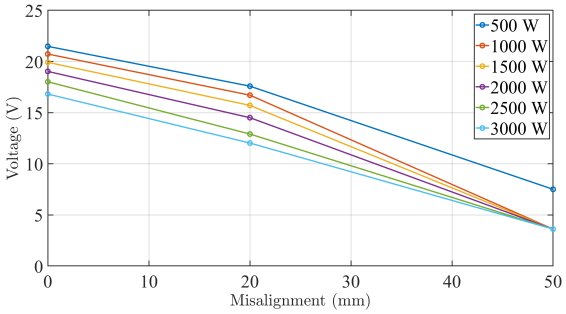

(b) Amplitude of the third harmonic

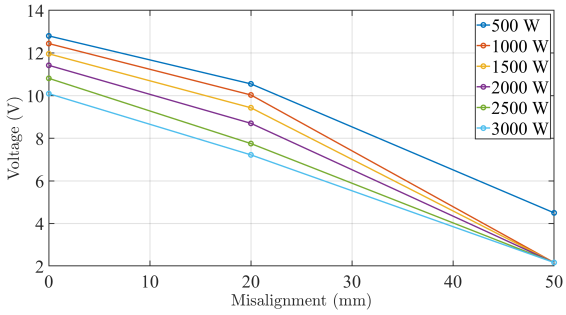

(c) Amplitude of the fifth harmonic

Figure 3.22: Amplitude of fundamental component 3.22a, third 3.22b and fifth 3.22c harmonics of the voltage v_5 under misalignment and charging power variations.

In the case of the amplitude of the fundamental and higher-order harmonics components of voltage v_5 it is needed to refer to Table B.22 where it can be observed objectively the values of the amplitudes. Table B.22 shows that the discrepancy is only verified for a situation of 500 W, which indicates that these parameters fulfill the first requirement.

Figures 3.22a, 3.22b and 3.22c confirm that these parameters satisfy the last requirement for feature selection.

Current - i_{sec}

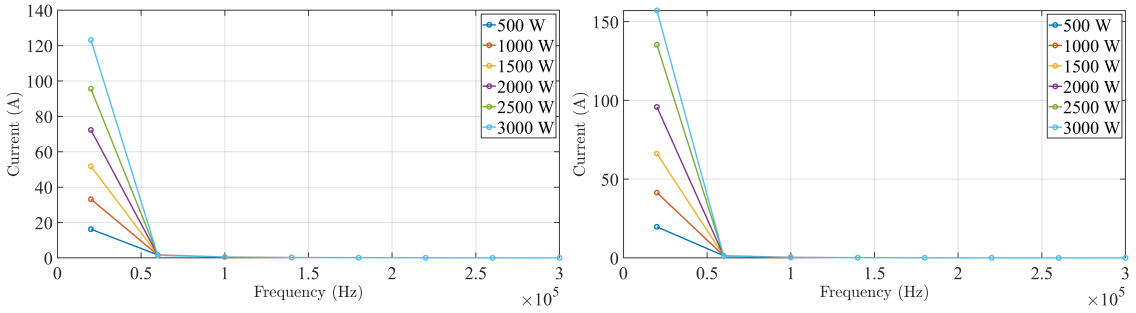

(a) $m_x = 0$ and $m_y = 0$ (b) $m_x = 20$ and $m_y = 0$

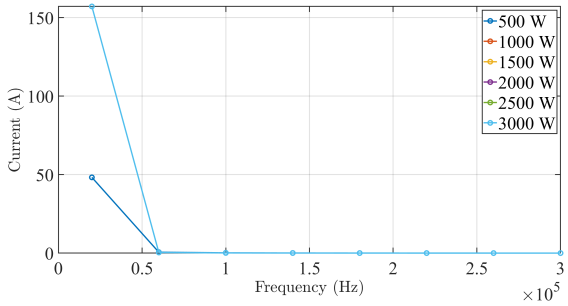

(c) $m_x = 50$ and $m_y = 0$

Figure 3.23: Amplitude of fundamental and higher-order harmonics component of the current i_{sec} in position 1 (3.23a), 2 (3.23b)and 3 (3.23c), respectively, under charging power variations.

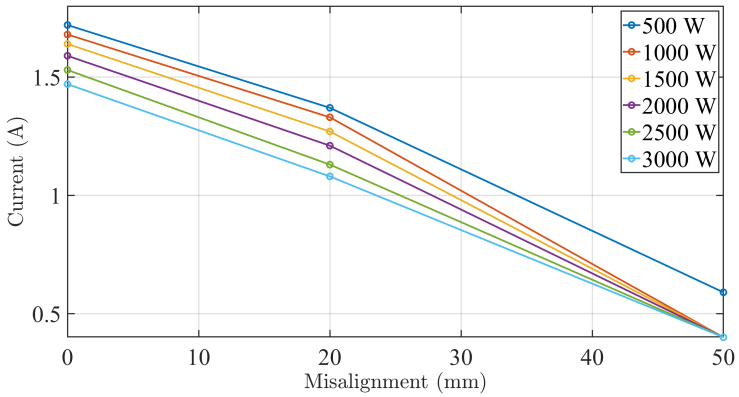

Figure 3.24: Amplitude of the third harmonic of the current i_{sec} under misalignment and charging power variations.

A discrepancy on the amplitude of the fundamental component of the current i_{sec} is identified which as previously stated is not intended. Therefore, the amplitude of

the third harmonic is the only parameter chosen, due to the fact that the amplitude of the fifth harmonic and beyond are considerably low.

Given the characteristic observed in figure 3.24 it can be concluded that this parameter also fulfills the requirements of the feature selection.

Reactive Power

In figure 3.12 it is referenced that through the voltage v_5 and the current i_{sec} the reactive power was calculated. In what the calculation of the amplitude of the harmonic components is concerned, equations 3.20 and 3.21 were implemented:

$$S_f = \frac{v_{5f}}{\sqrt{2}} * \frac{i_{secf}}{\sqrt{2}} \tag{3.20}$$

$$Q_f = S_f * sin(\theta_v - \theta_i), \tag{3.21}$$

where f is the frequency of the harmonics, S_f is the amplitude of the harmonics of the apparent power, v_{5f} and i_{secf} are the amplitudes of the harmonics of the voltage $v_5 f$ and current i_{secf}, respectively, θ_v and θ_i are the phases of the harmonics of the signals v_5 and i_{sec}, respectively, and Q_f is the amplitude of the harmonics of the reactive power.

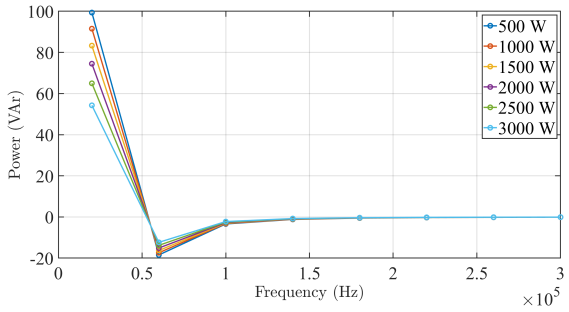

(a) $m_x = 0$ and $m_y = 0$

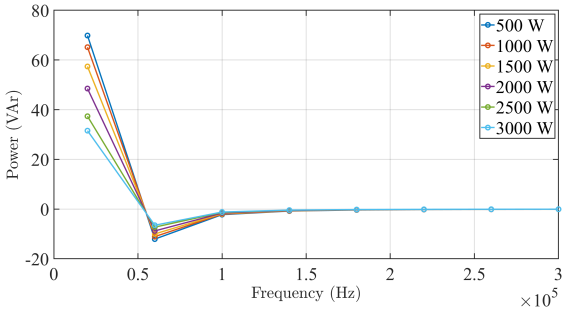

(b) $m_x = 20$ and $m_y = 0$

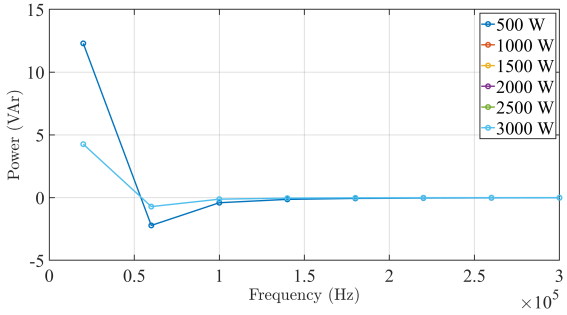

(c) $m_x = 50$ and $m_y = 0$

Figure 3.25: Amplitude of the fundamental and higher-order harmonic components of the reactive power in position 1 (3.25a), 2 (3.25b)and 3 (3.25c), respectively, under charging power variations.

Identically to the parameter priorly analysed, the fundamental component of the reactive power does not fulfill the first requirement of the feature selection due to the high discrepancy under charging power variations. Hence, it was only chosen the amplitude of third harmonic to be further analysed.

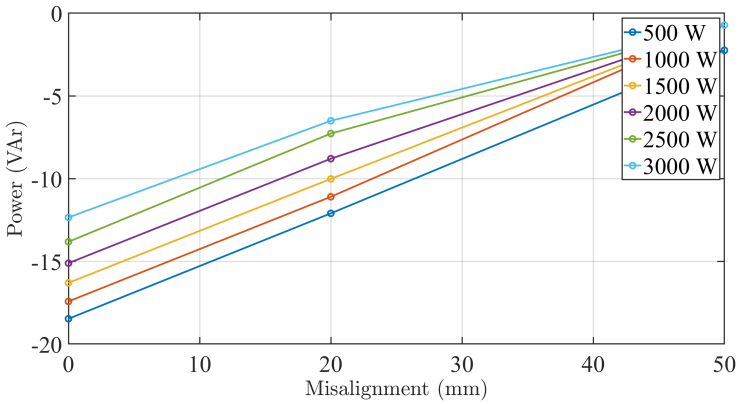

Figure 3.26: Amplitude of the third harmonic of the reactive power under misalignment and charging power variations.

Synthesizing the information from this detailed analysis, the features that are more suitable for the purpose of this work are:

- ◇ Amplitude of the 3^{rd} harmonic of voltage v_4;
- ◇ Amplitude of the 5^{th} harmonic of voltage v_4;
- ◇ Amplitude of the fundamental component of voltage v_5;
- ◇ Amplitude of the 3^{rd} harmonic of voltage v_5;
- ◇ Amplitude of the 5^{th} harmonic of voltage v_5;
- ◇ Amplitude of the 3^{rd} harmonic of current i_{sec};
- ◇ Amplitude of the 3^{rd} harmonic of the reactive power.

3.2.3 Data Normalization

A crucial step before training any AI model is without doubt the pre-processing of data, which includes removing outliers and normalization procedures, which helps improving the nature of the information [70]. Normalization by itself, is the process where the attributes of the dataset are categorized to increase the bond between them, making the dataset more flexible [71].

For this application in particular, the data was extracted for different values of charging power and misalignments. Since the AI model to be implemented must be able to predict the value of mutual inductance for various misalignments independently of the charging power value, the data must be normalized for a specific value of charging power. The objective of the developed AI model is to operate in a wide range of charging powers without the need for training for each charging power in particular. Hence, joining the fact that, in a real-world scenario, it is preferable for the AI model to estimate the value of mutual inductance correctly in systems that operate at a higher charging power, it was decided to normalize the data for 2000 W.

Thus, the procedure of normalization consisted on collecting the maximum value of each feature when the charging power of the system was 2000 W. Consequently, by employing (3.22) all the values of each feature were normalized. In this equation

$n_{f,c,p}$ refers to the normalized value for a given feature f, charging power c and misalignment position p, $max(v_{f,2000})$ corresponds to the maximum value among all misalignment positions of a given feature when the system works at 2000 W of charging power and $v_{f,c,p}$ is the real value of a given feature for a specific charging power and misalignment position.

$$n_{f,c,p} = \frac{max(v_{f,2000}) - v_{f,c,p}}{max(v_{f,2000})}. \tag{3.22}$$

Furthermore, it was necessary to multiply the value of mutual inductance by a factor of 10^6 to ensure the proper functioning of the AI model.

Chapter 4

Implemented AI Model and Results

This chapter will focus mainly on the presentation of the chosen AI model along with the obtained results across different scenarios as well as with the improvements applied to the algorithm during testing phase.

4.1 AI Model

The estimation of mutual inductance is a highly non linear and complex task to attain with mathematical models. As presented in section 2.2 there are plenty AI models available for regression tasks, however as cited in [48] ML models are reliable as long as the data samples available appropriately represent the end-to-end relationship, whereas the DL networks yield exceptional performance in classification and regression tasks [72] without the constraints of ML models [28] since it has the ability of adaptation.

With that said, it was decided to implement Multi-Layer-Percepton that is basically a fully connected multi-layer neural network [73]. This AI model has been widely employed in IPT systems [37, 48, 51–55, 57, 74–77] due to its high reliability and performance on fulfilling regression tasks.

Figure 4.1 illustrates the structure of the ANN implemented in this work. To reach this configuration, the performance of the network was tested under different combinations. In a first instance it was evaluated with a lower number of neurons and subsequently with a higher number of hidden layers and neurons.

The inputs of the ANN represent the values of each feature that were selected according to the requirements identified in section 3.2.2. The output corresponds to the predicted mutual inductance value. The NN to be able to compute an output value with the information available by the features needs to be composed of multiple layers. These layers are usually known as fully-connected layers since each layer has a defined number of neurons that are fully-connected between the layers of the network, i.e., each node of one layer of the neural network is connected to every node of the next layer [57].

Essentially, this connection between neurons can be formally expressed as presented in (4.1)[48], where $z_{l,i}$ denote the output of the i-th neuron in the l-th layer, $\sigma(\cdot)$ is a non-linear activation function, $\langle \cdot, \cdot \rangle$ represents the inner product, $\Theta_i^{(l)}$ is the weight vector for the i-th neuron in the l-ih hidden layer, u_l refers to the input

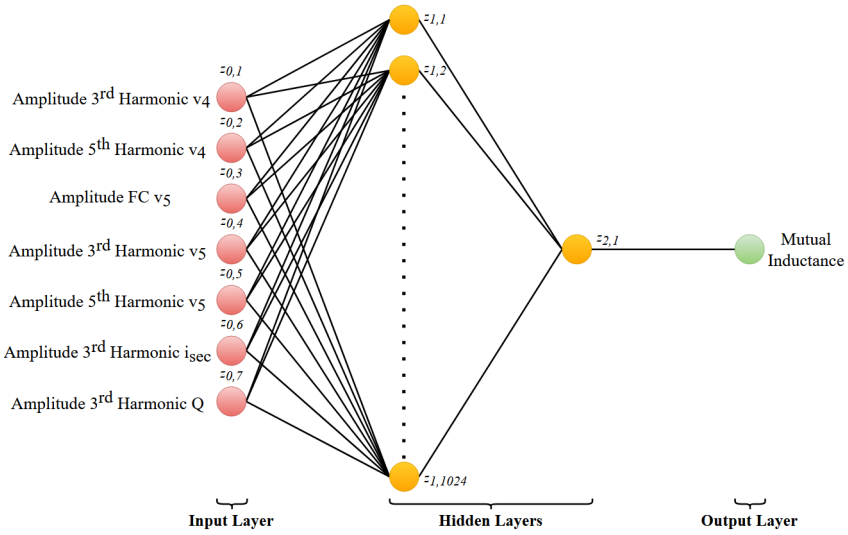

Figure 4.1: Graphic representation of the implemented ANN structure.

vector of the l-th layer and finally $b_i^{(l)}$ denotes the bias term.

$$z_{l,i} = \sigma\left(\left\langle \Theta_i^{(l)}, u_l \right\rangle + b_i^{(l)}\right). \tag{4.1}$$

Briefly, (4.1) characterizes the transition of knowledge between the fully-connected layers. However the main objective of a ANN is to minimize the error between its output and the target output. For this purpose there are various loss functions that can be implemented including, RMSE, MSE, among others. This is accomplished by giving a defined number of inputs and outputs to the network and consecutively along the course of the training phase the weights and biases of each neuron are adjusted until a predefined condition is met [57, 73], which depends on the optimizer [1] that is being used.

The NN was implemented in MATLAB software, using the *fitrnet* function that allows to implement a FFNN. This function was employed with the following parameters:

- ◇ **Predictor Data:** Refers to the data used for training. The network was parameterized with the objective of achieving a good performance while requiring minimal training data, that in this case refers to the positions of misalignment.
- ◇ **Response Data** Refers to the target variable related to the training data.
- ◇ **Layer Sizes:** Allows to define the size (number of neurons) and the quantity of fully-connected layers. The implemented network consisted of four layers: an input layer, two fully-connected layers, one with 1024 neurons and another with a single output and finally the output layer that corresponds to the predicted response values.
- ◇ **Activations:** The activation function can be defined, which in this case was the *logistic sigmoid* shown in section 2.2.

[1] Optimizers are algorithms used to modify weights and biases in order to reduce the value of the loss function [78].

- ◇ **Validation Patience:** It affects the duration of training. The training stops if the validation loss is greater than or equal to the minimum validation loss computed so far, a defined number of consecutive occurrences. This parameter was set to 100.

These parameters were attributed by trial and error, depending on the performance of the network.

4.2 Analysis of Results

The performance of the ANN is going to be tested under different conditions:

- ◇ The training data is extracted from simulations where signals are devoid of interference.
- ◇ The amplitude of the fundamental and harmonic components are obtained from signals with white noise.

The primary objective of the implemented model is to predict the mutual inductance value with minimal training requirements. In simpler terms, it aims to achieve this with as few information from misalignment positions as possible, simulating a real-world scenario where network training can be more straightforward, thus bolstering the robustness of the model. To analyse the performance of the ANN the tests presented in table 4.1 where conducted.

To analyse the performance of the network through all the test situations three metrics were selected: MAE, MAPE and R^2. Table 4.2 presents the performance of the network when trained with information from the two positions of misalignment illustrated in Figure 4.2.

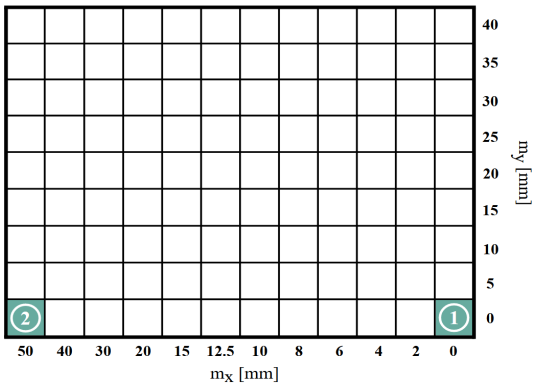

Figure 4.2: Misalignment positions considered for training the network.

The results presented clearly indicate a significant decline in the performance of the network for charging powers exceeding 2000 W and falling below 1500 W. To overcome this, the performance of the network was tested for different configurations, however the results did not improve. Consequently, it was necessary to take a different approach. Despite the metrics selected in section 3.2 appeared as optimal solutions, it is important to acknowledge that each feature contributes uniquely to the training process of the network. This implies that some features could potentially have counterproductive effects on the performance of the network. In a

Table 4.1: Conducted tests and respective descriptions.

Test Order	**Description**	
1^{st} **Test**	Normalization:	2000 W
	Features:	- v_4^3, v_4^5 - v_5^{FC}, v_5^3, v_5^5 - i_{sec}^3 - Q^3
	Number of positions:	2
	Noise:	No
2^{nd} **Test**	Normalization:	2000 W
	Features:	- v_4^3, v_4^5 - v_5^{FC}, v_5^3, v_5^5 - i_{sec}^3
	Number of positions:	2
	Noise:	No
3^{rd} **Test**	Normalization:	2000 W
	Features:	- v_4^3, v_4^5 - v_5^{FC}, v_5^3, v_5^5 - i_{sec}^3
	Number of positions:	8
	Noise:	No
4^{th} **Test**	Normalization:	2000 W
	Features:	- v_4^3, v_4^5 - v_5^{FC}, v_5^3, v_5^5 - i_{sec}^3
	Number of positions:	9
	Noise:	Yes

practical situation one sensor can measure all the harmonic components of one signal, therefore it is beneficial to analyze the performance of the network when it is trained recurring to the information of one signal at a time. Since the metric R^2 is conclusive enough about the accuracy of the network, Table 4.3 presents the performance of the network under the different conditions of training.

Table 4.2: Metrics of ANN when trained with data normalized for a 2000 W charging power from the misalignment positions illustrated in Figure 4.2.

Charging	**Metrics**		
Power (W)	MAE	MAPE (%)	R^2
500	1.7500	15.0166	0.6086
1000	1.0825	8.5072	0.8388
1500	0.4960	3.9510	0.9651
2000	0.3014	2.8317	0.9769
2500	0.9784	7.7771	0.8585
3000	1.5186	11.5341	0.6615

Table 4.3: R^2 Metric - Contribution of each signal when the ANN is trained with data normalized for a 2000 W charging power from the misalignment positions illustrated in Figure 4.2.

Charging	R^2			
Power (W)	v_4	v_5	i^3_{sec}	Q^3
500	0.6066	0.4609	0.8436	0.2277
1000	0.8465	0.7612	0.9478	0.6228
1500	0.9643	0.9273	0.9898	0.9105
2000	0.9866	0.9893	0.9854	0.9328
2500	0.9041	0.9399	0.9296	0.6417
3000	0.7564	0.8125	0.8463	0.1551

The results in Table 4.3 prove a the poor performance of the network when it relies only on the amplitude of the 3^{rd} harmonic of the reactive power. This implies that it is not beneficial to define this parameter as a feature. As a result, its removal translated into an improvement in the performance of the network as it can be verified in Table 4.4.

Despite the advancements made towards the best possible performance there is still one parameter that can be modified, the positions of misalignment used for the training of the network. Therefore, a more precise analysis is required.

In Figure 4.3, it can be observed the performance of the network in a different perspective. It allows a clear comparison between the predicted values of mutual inductance and the true value of the mutual inductance for each situation of misalignment. Essentially, points on the reference line indicate correct predictions.

By inspecting the behavior of the network it can be concluded that from 8 μH onwards there is a clear divergence between the predicted mutual inductance and the real mutual inductance value, which suggests that the network needs more in-

Table 4.4: Metrics - Without the contribution of the amplitude of the 3^{rd} harmonic of reactive power.

Charging Power (W)	**Metrics**		
	MAE	MAPE (%)	R^2
500	1.6917	15.0094	0.6299
1000	1.0166	8.0878	0.8569
1500	0.4859	3.8393	0.9672
2000	0.1968	1.9191	0.9867
2500	0.7903	6.2707	0.9066
3000	1.2618	9.5551	0.7650

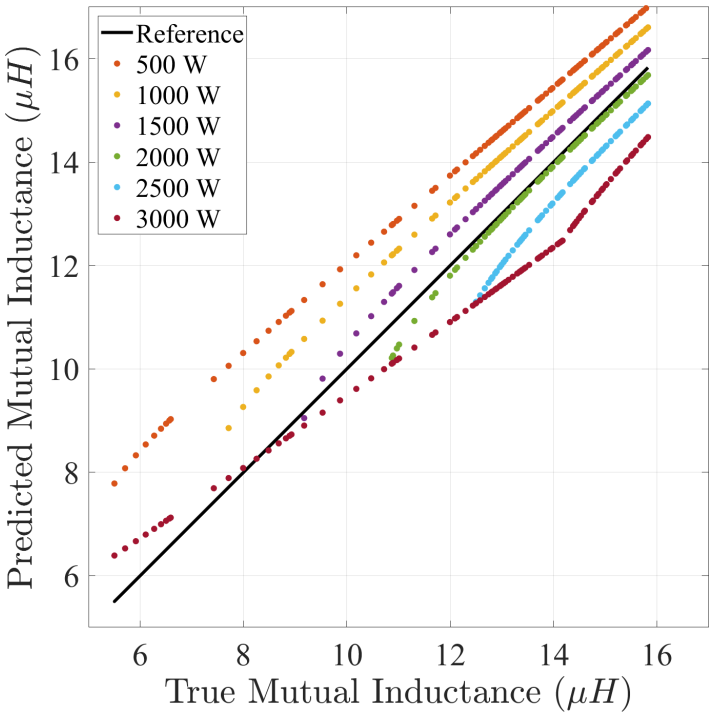

Figure 4.3: Comparison between predicted and real values of mutual inductance - data normalized for a 2000 W charging power from the misalignment positions illustrated in Figure 4.2.

formation to achieve a better performance. Thus, it was decided to provide to the network with the information obtained for the misalignment positions illustrated in Figure 4.4. The positions are identified with numbers between 1 and 5, where:

- ◇ Number 1: Position of maximum value of the mutual inductance (aligned position).
- ◇ Number 2: Positions where it was measured a value of mutual inductance between 15 μH and 15.5 μH.

◇ Number 3: Positions where was measured a value of mutual inductance between 12 μH and 12.5 μH.

◇ Number 4: Positions where was measured a value of mutual inductance between 8 μH and 8.5 μH.

◇ Number 5: Position of minimum value of the mutual inductance.

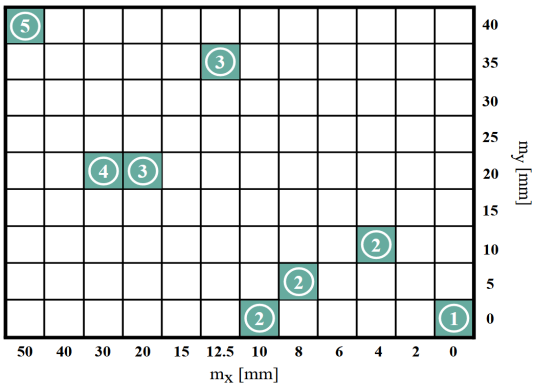

Figure 4.4: Misalignment positions used for ANN training.

This resulted in a training data of 8 out of 108 possible samples. The metrics and the concrete comparison between the predicted mutual inductance and the real mutual inductance are presented in Table 4.5 and Figure 4.5, respectively.

Table 4.5: Metrics - 2000 W Normalization and 8 misalignment positions for the train dataset.

Charging Power (W)	**Metrics**		
	MAE	MAPE (%)	R^2
500	0.2575	2.5675	0.9886
1000	0.1421	1.1794	0.9966
1500	0.0660	0.5118	0.9992
2000	0.0227	0.1820	0.9999
2500	0.0370	0.2762	0.9997
3000	0.0536	0.3835	0.9993

Given that the results obtained translated into an error inferior to 1%, it is fair to infer that the performance of the network is acceptable, accomplishing this way one of the predetermined objectives.

4.2.1 Influence of Noise

In this section it is intended to test the robustness of the network against noisy signals. In other words, previously the training and testing data was obtained through clean data, i.e., signals without any interference, from the simulation environment, while now the training data was acquired thorough signals with noise. It

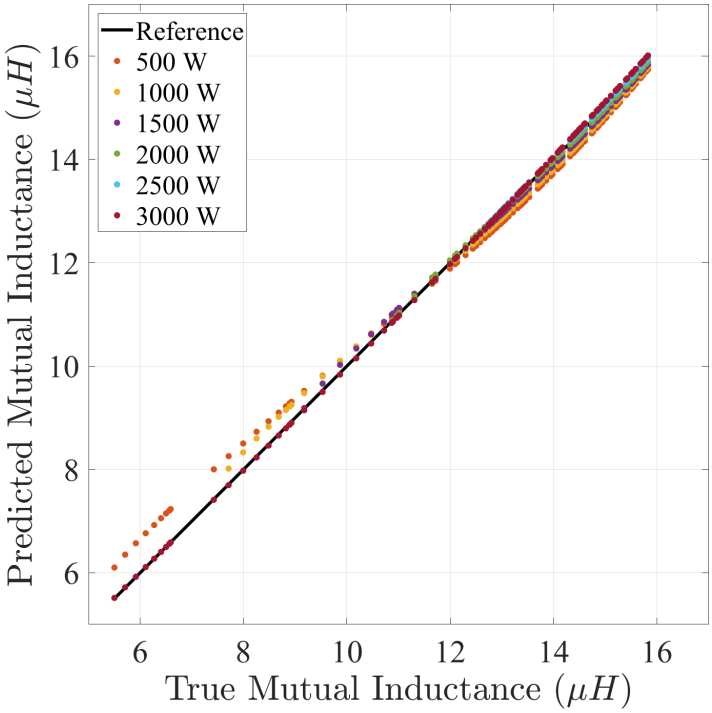

Figure 4.5: Test phase performance - 2000 W Normalization and eight misalignment positions for train data.

was added to each signal extracted from the simulations white noise with 5% of the amplitude of the respective signal. The obtained data is referred in this document as noisy data. To obtain similar results to the ones presented with no noise, it was necessary to add to the training data an additional misalignment position where the value of mutual inductance stood in a range between 15 μH and 15.5 μH.

Hence, the metrics and the comparison between the real and predicted values of mutual inductance are presented in table 4.6 and in Figure 4.6, respectively.

Table 4.6: Metrics of ANN when trained with noisy data normalized for a 2000 W charging power from the nine misalignment positions.

Charging	**Metrics**		
Power (W)	MAE	MAPE (%)	R^2
500	0.2921	2.6821	0.9873
1000	0.1652	1.3152	0.9958
1500	0.0760	0.5763	0.9990
2000	0.0186	0.1539	0.9999
2500	0.0370	0.2745	0.9997
3000	0.0551	0.3923	0.9992

Table 4.6 demonstrates that similarly to the previous situation, the estimation capability of the presented network is accurate with an error percentage also inferior

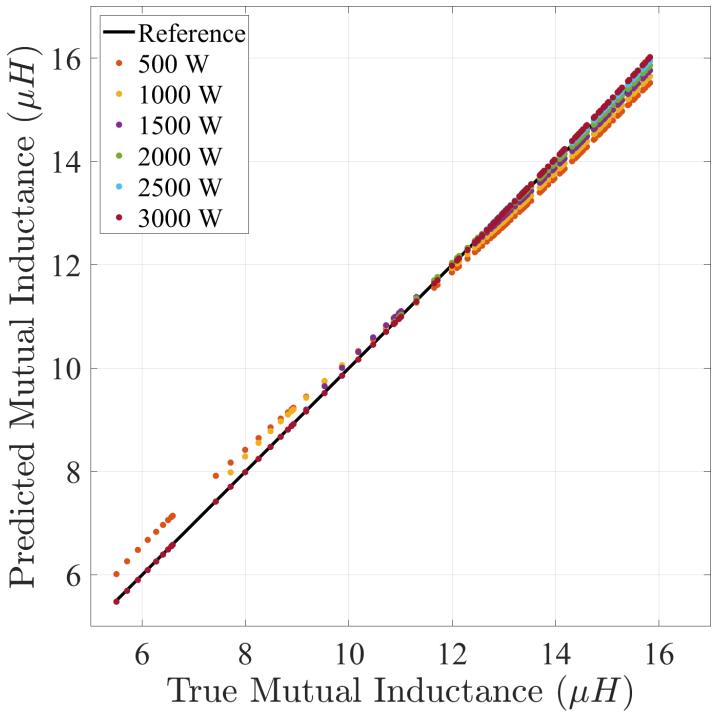

Figure 4.6: Predicted Mutual Inductance value VS Real Mutual Inductance value for all charging powers situations with noise introduction.

to 1%. This is only reasonable to affirm considering the tests conducted in this work. An additional possibility was to test the performance of the network in misalignment positions out of the boundaries established in the misalignments grid.

Additionally, it is important to note that the research was carried out in a computer equipped with an Intel Core i7-8750H, 16 GB of RAM memory and an NVIDIA GeForce RTX 1050 Ti graphics card. The training phase with clean and noisy data was completed after approximately 200 epochs for each dataset, resulting in a process that lasted around 2 seconds.

Chapter 5

Conclusion and Future Work

5.1 Conclusions

Given the several advantages of using wireless charging systems in EVs, such as the ability to provide power transfer without physical contact between the coils, galvanic isolation, absence of user interaction and protection under adverse weather conditions, it guarantees a more convenient way to use the vehicle. Therefore, it is of true relevance embark on the path that allows the optimization and improvement of IPT systems. To this end, after understanding the benefits of AI and with the aim of contributing to this evolution, this dissertation proposed the implementation of an AI model to estimate the mutual inductance under misalignment conditions between the transmitter and receiver pads. This is a crucial parameter with the capability of maximizing the power transfer, therefore the importance to be estimated accurately.

As analyzed in the literature review, there are various AI models that could be implemented to this end, such as random forest regression, support vector machines, decision trees, ANNs, among others. Nonetheless, in the development of this work, it was only tested the performance of an ANN.

The parameterization of the network along with the selection of features more suitable for this application, was determined through a trial and error phases, based on the performance of the network. Considering the charging powers admitted by the IPT system, it is recognized that in a real-world wireless charging scenario, optimal AI model performance at higher charging powers is preferable. Nevertheless, the proposed configuration manages to deliver good estimation performance across the entire range of charging powers. To accomplish this, it was chosen as features the variables that have a pronounced variation during misalignment occurrences while maintaining minimal variation when the charging power varies. Consequently, the chosen features include the amplitude of the harmonic components of three signals: the amplitude of the third and fifth harmonic of the voltage measured in terminals of receiver pad, the amplitude of the fundamental component, as well as, of the third and fifth harmonic of the voltage measured in receiver pad after the capacitor of the resonant tank referred to the receiver pad and finally the amplitude of the third harmonic of the current measured in the receiver pad.

Upon analyzing the results, it was concluded that a high number of features is not a necessary condition for achieving an improved performance of the network. There are cases where additional features can worsen the accuracy of the neural network. In this work, the addition of the amplitude of the third harmonic of the

reactive power is a clear example of this statement, since without its contribution the accuracy of the model increased by approximately 15%, 6%, 1%, 1%, 6% and 18% for charging power levels of 500 W, 1000 W, 1500 W, 2000 W, 2500 W and 3000 W, respectively.

To further verify the robustness of the network, training data was derived from clean and noisy signals. In the first case, the highest observed error was 2.57% occurring at a charging power of 500 W. Similarly, the highest error for the second situation was 2.68% also at a charging power of 500 W. It is also worth to mention that the training phase was concluded in approximately 2 seconds, which is primarily due to the fact that the neural network only contains two hidden layers and the training dataset is noticeably reduced. Therefore its implementation does not entail a high computational cost.

Thus, these results clearly imply that the proposed model can effectively estimate the value of the mutual inductance under misalignment and charging power variations, subsequently contributing to the maximization of the power transfer. Furthermore, it can be concluded that given the circumstances of the training phase, especially regarding the dimension of the dataset, the proposed ANN is a well suited solution for this purpose, even when comparing with other ML models.

5.2 Future Work

Considering the conducted research and the diverse applications of AI, the following suggestions are presented to further expand and optimize IPT systems through AI:

- ◇ Incorporate a buck-boost converter and a battery in the output of the simulation model. Train and verify the performance of the AI model under various state-of-charge conditions of the battery.
- ◇ Deploy the developed network in an identical experimental setup to validate its performance under real-world conditions.
- ◇ Extend the implementation of the network to dynamic IPT systems under diverse resonant topologies.
- ◇ Broaden the capabilities of the network by training it to predict other relevant circuit parameters beyond mutual inductance such as the exact position of the receiver pad.

References

[1] Md. Hasin Mahtab Moon et al. "Static and Dynamic Charging System for a Four-Wheeler Electric Vehicle by Inductive Coupling Wireless Power Transmission System". *2021 International Conference on Green Energy, Computing and Sustainable Technology (GECOST)*. 2021, pp. 1–6. DOI: 10.1109/GECOST52368.2021.9538752.

[2] Emanuel G. Marques et al. "Design Methodology of a Three Coil IPT System With Parameters Identification for EVs". *IEEE Transactions on Vehicular Technology* 70.8 (2021), pp. 7509–7521. DOI: 10.1109/TVT.2021.3089419.

[3] Alina Sekretaryova. "Chapter 4 - Powering wearable bioelectronic devices". *Wearable Bioelectronics*. Ed. by Onur Parlak, Alberto Salleo, and Anthony Turner. Materials Today. Elsevier, 2020, pp. 89–132. ISBN: 978-0-08-102407-2. DOI: https://doi.org/10.1016/B978-0-08-102407-2.00005-9. URL: https://www.sciencedirect.com/science/article/pii/B9780081024072000059.

[4] Mohammad Zamani et al. "A review of inductive power transfer for electric vehicles". *2019 International Conference on Electrical Engineering Research & Practice (ICEERP)*. 2019, pp. 1–5. DOI: 10.1109/ICEERP49088.2019.8956971.

[5] Valter S. Costa et al. "Resonant converter topology impact on a Dynamic IPT application". *2021 Telecoms Conference (ConfTELE)*. 2021, pp. 1–6. DOI: 10.1109/ConfTELE50222.2021.9435578.

[6] Satyam Bhuyan. *Mutual inductance: Definition, formula, symbol, and unit*. Feb. 2023. URL: https://www.sciencefacts.net/mutual-inductance.html.

[7] Immanuel N. Jiya and Rupert Gouws. "Overview of Power Electronic Switches: A Summary of the Past, State-of-the-Art and Illumination of the Future". *Micromachines* 11.12 (2020). ISSN: 2072-666X. DOI: 10.3390/mi11121116. URL: https://www.mdpi.com/2072-666X/11/12/1116.

[8] Grant A. Covic and John T. Boys. "Inductive Power Transfer". *Proceedings of the IEEE* 101.6 (2013), pp. 1276–1289. DOI: 10.1109/JPROC.2013.2244536.

[9] Valter S. Costa et al. "Magnetic Couplers for Dynamic IPT Systems". *2019 IEEE Vehicle Power and Propulsion Conference (VPPC)*. 2019, pp. 1–6. DOI: 10.1109/VPPC46532.2019.8952176.

[10] Emanuel G. Marques et al. "Double Coupling IPT Systems for EV Charging Applications". *2021 IEEE Vehicle Power and Propulsion Conference (VPPC)*. 2021, pp. 1–6. DOI: 10.1109/VPPC53923.2021.9699261.

[11] Emanuel G. Marques et al. “A new IPT transmitter configuration tolerant to magnetic coupler displacements”. *IECON 2017 - 43rd Annual Conference of the IEEE Industrial Electronics Society*. 2017, pp. 5307–5312. DOI: 10.1109/IECON.2017.8216919.

[12] Aganti Mahesh, Bharatiraja Chokkalingam, and Lucian Mihet-Popa. “Inductive Wireless Power Transfer Charging for Electric Vehicles–A Review”. *IEEE Access* 9 (2021), pp. 137667–137713. DOI: 10.1109/ACCESS.2021.3116678.

[13] Lingbing Gong et al. “Adaptive Smart Control Method for Electric Vehicle Wireless Charging System”. *Energies* 11.10 (2018). ISSN: 1996-1073. DOI: 10.3390/en11102685. URL: https://www.mdpi.com/1996-1073/11/10/2685.

[14] Alicia Triviño-Cabrera, Zhengyu Lin, and José A. Aguado. “Impact of Coil Misalignment in Data Transmission over the Inductive Link of an EV Wireless Charger”. *Energies* 11.3 (2018). ISSN: 1996-1073. URL: https://www.mdpi.com/1996-1073/11/3/538.

[15] Van-Binh Vu et al. “Operation of Inductive Charging Systems Under Misalignment Conditions: A Review for Electric Vehicles”. *IEEE Transactions on Transportation Electrification* 9.1 (2023), pp. 1857–1887. DOI: 10.1109/TTE.2022.3165465.

[16] Ainur Rakhymbay et al. “Precise Analysis on Mutual Inductance Variation in Dynamic Wireless Charging of Electric Vehicle”. *Energies* 11.3 (2018). ISSN: 1996-1073. DOI: 10.3390/en11030624. URL: https://www.mdpi.com/1996-1073/11/3/624.

[17] Mohammad Kamar Uddin et al. “A review on high frequency resonant inverter technologies for wireless power transfer using magnetic resonance coupling”. *2014 IEEE Conference on Energy Conversion (CENCON)*. 2014, pp. 412–417. DOI: 10.1109/CENCON.2014.6967539.

[18] Aaron Cai et al. “A high frequency, high efficiency GaN HFET based inductive power transfer system”. *2015 IEEE Applied Power Electronics Conference and Exposition (APEC)*. 2015, pp. 3094–3100. DOI: 10.1109/APEC.2015.7104793.

[19] Ali Zakerian, Sadegh Vaez-Zadeh, and Amir Babaki. “Efficiency Maximization Control and Voltage Regulation for Dynamic Wireless EV Charging Systems with Mutual Induction Estimation”. *IECON 2019 - 45th Annual Conference of the IEEE Industrial Electronics Society*. Vol. 1. 2019, pp. 4298–4303. DOI: 10.1109/IECON.2019.8926940.

[20] Giorgio Lovison, Takehiro Imura, and Yoichi Hori. “Secondary-side-only simultaneous power and efficiency control by online mutual inductance estimation for dynamic wireless power transfer”. *IECON 2016 - 42nd Annual Conference of the IEEE Industrial Electronics Society*. 2016, pp. 4553–4558. DOI: 10.1109/IECON.2016.7793790.

[21] Songcen Wang et al. “Research on Mutual Inductance Prediction of Resonant Magnetic Coupling Wireless Power Transmission System Based on Recursive Least Square Method”. *IOP Conference Series: Materials Science and Engineering* 719.1 (Jan. 2020), p. 012039. DOI: 10.1088/1757-899X/719/1/012039. URL: https://dx.doi.org/10.1088/1757-899X/719/1/012039.

[22] Beibei Song et al. "A Fast and General Method to Calculate Mutual Inductance for EV Dynamic Wireless Charging System". *IEEE Transactions on Power Electronics* 36.3 (2021), pp. 2696–2709. DOI: 10.1109/TPEL.2020.3015100.

[23] Shufan Li et al. "Flexible Energy-Transfer Control of Dynamic Wireless Power Transfer System Based On Estimation of Load and Mutual Inductance". *IEEE Transactions on Industry Applications* 58.1 (2022), pp. 1157–1167. DOI: 10.1109/TIA.2021.3096173.

[24] E. S. Brunette, R. C. Flemmer, and C. L. Flemmer. "A review of artificial intelligence". *2009 4th International Conference on Autonomous Robots and Agents*. 2009, pp. 385–392. DOI: 10.1109/ICARA.2000.4804025.

[25] Shuai Zhao, Frede Blaabjerg, and Huai Wang. "An Overview of Artificial Intelligence Applications for Power Electronics". *IEEE Transactions on Power Electronics* 36.4 (2021), pp. 4633–4658. DOI: 10.1109/TPEL.2020.3024914.

[26] *What is Artificial Intelligence (AI) ?* URL: https://www.ibm.com/topics/artificial-intelligence.

[27] Jack Copeland. *Artificial Intelligence*. Aug. 2023. URL: https://www.britannica.com/technology/artificial-intelligence.

[28] Seng Chee Tan, Alwyn Vwen Yen Lee, and Min Lee. "A systematic review of artificial intelligence techniques for collaborative learning over the past two decades". *Computers and Education: Artificial Intelligence* 3 (2022), p. 100097. ISSN: 2666-920X. DOI: https://doi.org/10.1016/j.caeai.2022.100097. URL: https://www.sciencedirect.com/science/article/pii/S2666920X22000522.

[29] Abhijit Ghatak. *Machine Learning with R*. en. Singapore: Springer Singapore, 2017. ISBN: 978-981-10-6807-2 978-981-10-6808-9. DOI: 10.1007/978-981-10-6808-9. URL: http://link.springer.com/10.1007/978-981-10-6808-9 (visited on 08/01/2023).

[30] R. Saravanan and Pothula Sujatha. "A State of Art Techniques on Machine Learning Algorithms: A Perspective of Supervised Learning Approaches in Data Classification". *2018 Second International Conference on Intelligent Computing and Control Systems (ICICCS)*. 2018, pp. 945–949. DOI: 10.1109/ICCONS.2018.8663155.

[31] Ajay Shrestha and Ausif Mahmood. "Review of Deep Learning Algorithms and Architectures". *IEEE Access* 7 (2019), pp. 53040–53065. DOI: 10.1109/ACCESS.2019.2912200.

[32] Iqbal H. Sarker. "Deep Learning: A Comprehensive Overview on Techniques, Taxonomy, Applications and Research Directions". en. *SN Computer Science* 2.6 (Nov. 2021), p. 420. ISSN: 2662-995X, 2661-8907. DOI: 10.1007/s42979-021-00815-1. URL: https://link.springer.com/10.1007/s42979-021-00815-1.

[33] *AI: What are the different Domains/Subsets of Artificial Intelligence?* Feb. 2023. URL: https://medium.com/@a.sale/ai-what-are-the-different-domains-subsets-of-artificial-intelligence-4cfd5477584.

[34] Shamsul Arefeen Al Mahmud, Prasad Jayathurathnage, and Sergei A. Tretyakov. "Machine Learning Assisted Characteristics Prediction for Wireless Power Transfer Systems". *IEEE Access* 10 (2022), pp. 40496–40505. DOI: 10.1109/ACCESS.2022.3167162.

[35] Spyros Makridakis. "Accuracy measures: theoretical and practical concerns". *International Journal of Forecasting* 9.4 (1993), pp. 527–529. ISSN: 0169-2070. DOI: https://doi.org/10.1016/0169-2070(93)90079-3. URL: https://www.sciencedirect.com/science/article/pii/0169207093900793.

[36] J. Scott Armstrong and Robert Fildes. "Correspondence on the selection of error measures for comparisons among forecasting methods". en. *Journal of Forecasting* 14.1 (Jan. 1995), pp. 67–71. ISSN: 02776693, 1099131X. DOI: 10.1002/for.3980140106. URL: https://onlinelibrary.wiley.com/doi/10.1002/for.3980140106 (visited on 08/03/2023).

[37] Kai Sato et al. "Deep Neural Network Based Inductance Calculations of Wireless Power Transfer Systems". *2022 IEEE 11th Global Conference on Consumer Electronics (GCCE)*. 2022, pp. 222–223. DOI: 10.1109/GCCE56475.2022.10014111.

[38] Kaiyuan Wang, Yun Yang, and Xun Zhang. "Advanced Front-end Monitoring Scheme for Inductive Power Transfer Systems Based on Random Forest Regression". *2023 IEEE Applied Power Electronics Conference and Exposition (APEC)*. 2023, pp. 2901–2907. DOI: 10.1109/APEC43580.2023.10131513.

[39] Kyle J. Goodrick et al. "Machine Learning Estimators for Power Electronics Design and Optimization". *2021 IEEE Design Methodologies Conference (DMC)*. 2021, pp. 1–8. DOI: 10.1109/DMC51747.2021.9529937.

[40] Lingxin Lan et al. "A Reflected Impedance Estimation Technique for Inductive Power Transfer". *2019 IEEE PELS Workshop on Emerging Technologies: Wireless Power Transfer (WoW)*. 2019, pp. 45–48. DOI: 10.1109/WoW45936.2019.9030654.

[41] Lahiru Aththanayake et al. "Performance Analysis of Regression and Artificial Neural Network Schemes for Dynamic Model Reduction of Power Systems". *2021 3rd International Conference on Smart Power & Internet Energy Systems (SPIES)*. 2021, pp. 358–363. DOI: 10.1109/SPIES52282.2021.9633912.

[42] Johannes Lederer. *Activation Functions in Artificial Neural Networks: A Systematic Overview*. en. arXiv:2101.09957 [cs, stat]. Jan. 2021. URL: http://arxiv.org/abs/2101.09957 (visited on 08/03/2023).

[43] Sagar Sharma. *Activation functions in neural networks*. Nov. 2022. URL: https://towardsdatascience.com/activation-functions-neural-networks-1cbd9f8d91d6.

[44] Laith Alzubaidi et al. "Review of deep learning: concepts, CNN architectures, challenges, applications, future directions". en. *Journal of Big Data* 8.1 (Mar. 2021), p. 53. ISSN: 2196-1115. DOI: 10.1186/s40537-021-00444-8. URL: https://journalofbigdata.springeropen.com/articles/10.1186/s40537-021-00444-8 (visited on 08/03/2023).

[45] Chinwe Igiri, Anyama Uzoma, and Abasiama Silas. "Effect of Learning Rate on Artificial Neural Network in Machine Learning". *International Journal of Engineering Research* 4 (June 2021).

[46] Tianhao Wang et al. "Design of Electric Vehicle's Wireless Power Transfer System Based on Deep Learning Combined With Multi-Objective Optimization". *IEEE Transactions on Components, Packaging and Manufacturing Technology* 12.12 (2022), pp. 1983–1994. DOI: 10.1109/TCPMT.2022.32228419200511.

[47] Shuntaro Inoue et al. "Fast Design Optimization Method Utilizing a Combination of Artificial Neural Networks and Genetic Algorithms for Dynamic Inductive Power Transfer Systems". *IEEE Open Journal of Power Electronics* 3 (2022), pp. 915–929. DOI: 10.1109/OJPEL.2022.3224422.

[48] Minki Kim et al. "Characterization of the Quality Factor in Spiral Coil Designs for High-Frequency Wireless Power Transfer Systems using Machine Learning". *2022 IEEE 23rd Workshop on Control and Modeling for Power Electronics (COMPEL)*. 2022, pp. 1–8. DOI: 10.1109/COMPEL53829.2022.9830005.

[49] Yun Yang, Xun Zhang, and Kaiyuan Wang. "Robust Random Forest Regressor-Based Mutual Inductance Monitoring Scheme for Inductive Power Transfer Systems". *2022 IEEE International Power Electronics and Application Conference and Exposition (PEAC)*. 2022, pp. 171–176. DOI: 10.1109/PEAC56338.2022.9959485.

[50] Zhiyong Huang et al. "Maximum efficiency tracking design of wireless power transmission system based on machine learning". *Energy Reports* 8 (2022). 2022 The 5th International Conference on Renewable Energy and Environment Engineering, pp. 447–455. ISSN: 2352-4847. DOI: https://doi.org/10.1016/j.egyr.2022.10.139. URL: https://www.sciencedirect.com/science/article/pii/S2352484722020753.

[51] Hang Shen et al. "Receiver Position Estimation Method for Multitransmitter WPT System Based on Machine Learning". *IEEE Transactions on Industry Applications* 58.1 (2022), pp. 1231–1241. DOI: 10.1109/TIA.2021.3103489.

[52] Reza Tavakoli et al. "EV Misalignment Estimation in DWPT Systems Utilizing the Roadside Charging Pads". *IEEE Transactions on Transportation Electrification* 8.1 (2022), pp. 752–766. DOI: 10.1109/TTE.2021.3091969.

[53] Reza Tavakoli and Zeljko Pantic. "ANN-based algorithm for estimation and compensation of lateral misalignment in dynamic wireless power transfer systems for EV charging". *2017 IEEE Energy Conversion Congress and Exposition (ECCE)*. 2017, pp. 2602–2609. DOI: 10.1109/ECCE.2017.8096493.

[54] Siying He et al. "Load and Self/Mutual Inductance Identification Method of LCC-S WPT System Based on PyTorch". *2022 IEEE 9th International Conference on Power Electronics Systems and Applications (PESA)*. 2022, pp. 1–5. DOI: 10.1109/PESA55501.2022.10038339.

[55] Tianhao Bai et al. "Machine Learning-Assisted Wireless Power Transfer Based on Magnetic Resonance". *IEEE Access* 7 (2019), pp. 109454–109459. DOI: 10.1109/ACCESS.2019.2933679.

[56] Kyungmin Na, Jieun Kim, and Young-Jin Park. "Machine Learning-based Power Control Technique for Wireless Power Transfer". *2020 IEEE Wireless Power Transfer Conference (WPTC)*. 2020, pp. 443–446. DOI: 10.1109/WPTC48563.2020.9295544.

[57] Byeong-Guk Choi and Yun-Su Kim. "New Structure Design of Ferrite Cores for Wireless Electric Vehicle Charging by Machine Learning". *IEEE Transactions on Industrial Electronics* 68.12 (2021), pp. 12162–12172. DOI: 10.1109/TIE.2020.3047041.

[58] Byeong-Guk Choi, Eun S. Lee, and Yun-Su Kim. "Optimal Structure Design of Ferromagnetic Cores in Wireless Power Transfer by Reinforcement Learning". *IEEE Access* 8 (2020), pp. 179295–179306. DOI: 10.1109/ACCESS.2020.3027765.

[59] Hiroki Tanabe, Ellen H. Fukuda, and Nobuo Yamashita. *New merit functions for multiobjective optimization and their properties*. 2023. arXiv: 2010.09333 [math.OC].

[60] Juan M. Arteaga et al. "Multi-MHz IPT Systems for Variable Coupling". *IEEE Transactions on Power Electronics* 33.9 (2018), pp. 7744–7758. DOI: 10.1109/TPEL.2017.2768244.

[61] Fabian Pedregosa et al. "Scikit-learn: Machine Learning in Python". *Journal of Machine Learning Research* 12.85 (2011), pp. 2825–2830. URL: http://jmlr.org/papers/v12/pedregosa11a.html.

[62] Jazmin P. Tan et al. "A Performance Review of Recurrent Neural Networks Long Short-Term Memory (LSTM)". *2022 3rd International Conference for Emerging Technology (INCET)*. 2022, pp. 1–5. DOI: 10.1109/INCET54531.2022.9824567.

[63] Emanuel G. Marques et al. "Double Coupling In-Wheel IPT System for Electric Vehicles". *IEEE Transactions on Vehicular Technology* (2023), pp. 1–13. DOI: 10.1109/TVT.2023.3271814.

[64] Amr Mostafa et al. "Output Power Control of an S-S IPT System Based on Voltage and Frequency Tuning for EV Charging". *2021 IEEE PELS Workshop on Emerging Technologies: Wireless Power Transfer (WoW)*. 2021, pp. 1–5. DOI: 10.1109/WoW51332.2021.9462886.

[65] Masafumi Oyamada. "Extracting Feature Engineering Knowledge from Data Science Notebooks". *2019 IEEE International Conference on Big Data (Big Data)*. 2019, pp. 6172–6173. DOI: 10.1109/BigData47090.2019.9006522.

[66] Ayodeji Olalekan Salau and Shruti Jain. "Feature Extraction: A Survey of the Types, Techniques, Applications". *2019 International Conference on Signal Processing and Communication (ICSC)*. 2019, pp. 158–164. DOI: 10.1109/ICSC45622.2019.8938371.

[67] Masaya Ote, Soyeon Jeong, and Manos M Tentzeris. "Foreign Object Detection for Wireless Power Transfer Based on Machine Learning". *2020 IEEE Wireless Power Transfer Conference (WPTC)*. 2020, pp. 476–479. DOI: 10.1109/WPTC48563.2020.9295641.

[68] Sheng Li et al. “Foreign Object Detection for LCC-S Wireless Power Transfer System Based on LSTM”. *2021 IEEE International Conference on Emergency Science and Information Technology (ICESIT)*. 2021, pp. 165–169. DOI: 10.1109/ICESIT53460.2021.9696918.

[69] URL: https://download.ni.com/evaluation/pxi/Understanding%20FFTs%20and%20Windowing.pdf.

[70] Jesmeen M. Z. H et al. “A Survey on Cleaning Dirty Data Using Machine Learning Paradigm for Big Data Analytics”. en. *Indonesian Journal of Electrical Engineering and Computer Science* 10.3 (June 2018), p. 1234. ISSN: 2502-4760, 2502-4752. DOI: 10.11591/ijeecs.v10.i3.pp1234-1243. URL: http://ijeecs.iaescore.com/index.php/IJEECS/article/view/12097.

[71] V N Ganapathi Raju et al. “Study the Influence of Normalization/Transformation process on the Accuracy of Supervised Classification”. *2020 Third International Conference on Smart Systems and Inventive Technology (ICSSIT)*. 2020, pp. 729–735. DOI: 10.1109/ICSSIT48917.2020.9214160.

[72] Ian Goodfellow, Yoshua Bengio, and Aaron Courville. *Deep Learning*. MIT Press, Nov. 2016.

[73] Hosameldin Ahmed and Asoke K. Nandi. “Artificial Neural Networks (ANNs)”. *Condition Monitoring with Vibration Signals: Compressive Sampling and Learning Algorithms for Rotating Machines*. 2019, pp. 239–258. DOI: 10.1002/9781119544678.ch12.

[74] Muhammad Enagi Bima et al. “Neural Network Based Mutual Inductance Estimation for Maximum Power Point Tracking in Wireless Power Transfer Array”. *2021 IEEE Vehicle Power and Propulsion Conference (VPPC)*. 2021, pp. 1–5. DOI: 10.1109/VPPC53923.2021.9699144.

[75] M. Y. El-Sharkh, Daniela Wolter Ferreira Touma, and Yousef Dawoud. “Artificial Neural Network Based Wireless Power Transfer Behavior Estimation”. *2019 SoutheastCon*. 2019, pp. 1–6. DOI: 10.1109/SoutheastCon42311.2019.9020422.

[76] Yang Li et al. “An Automatic Impedance Matching Method Based on the Feedforward-Backpropagation Neural Network for a WPT System”. *IEEE Transactions on Industrial Electronics* 66.5 (2019), pp. 3963–3972. DOI: 10.1109/TIE.2018.2835410.

[77] Sungryul Huh et al. “Design to Minimize Coupling Coefficient between Transmitter Coils based on Deep Learning for Wireless Power Transfer with Multi-Transmitter”. *2022 Wireless Power Week (WPW)*. 2022, pp. 443–447. DOI: 10.1109/WPW54272.2022.9853954.

[78] *Various Optimization Algorithms For Training Neural Network*. Jan. 2019. URL: https://towardsdatascience.com/optimizers-for-training-neural-network-59450d71caf6.

Appendix A

SSS IPT System details

This appendix presents in greater detail the IPT system used for the measurements of the mutual inductance. An overview of the used prototype is displayed in Figure A.1.

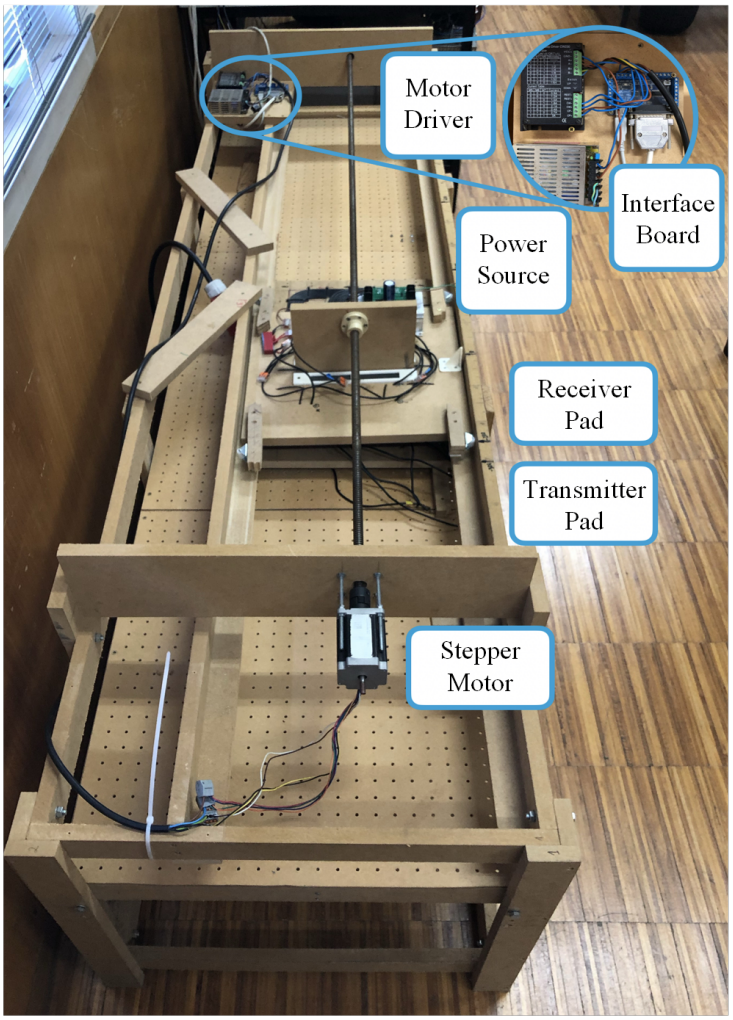

Figure A.1: Overview of the IPT prototype.

The transmitter and receiver pads were installed into the prototype with the same dimensions and shared the same bipolar topology. Each coil within the pad has 10 turns. Figure A.2 provides a visual representation of the transmitter pad.

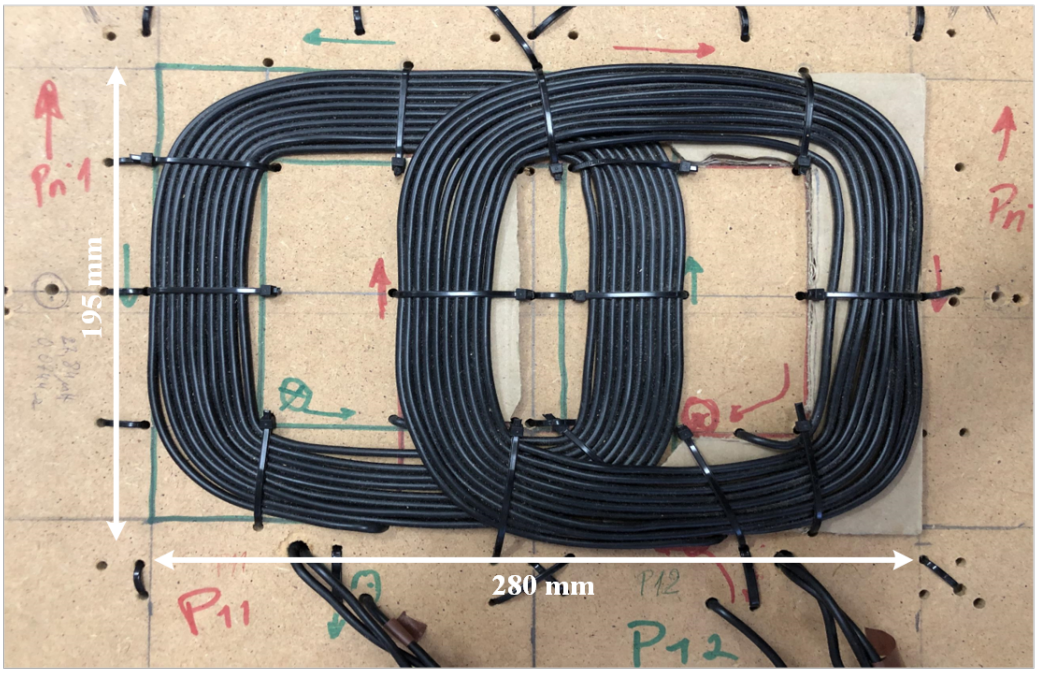

Figure A.2: Transmitter pad.

As referred in Section 3.1.2 the values of self and mutual inductances were measured by an LCR meter. This particular device is displayed in Figure A.3.

Figure A.3: LCR BK PRECISION 889A.

Appendix B

Feature Extraction

This appendix reveals the remaining detailed data that served as a foundation to derive the conclusions mentioned in section 3.2.

B.1 Waveform Analysis

This section serves the purpose of supporting the analysis carried out, with waveforms of the remaining signals from transmitter and receiver sides.

B.1.1 Voltage v_2

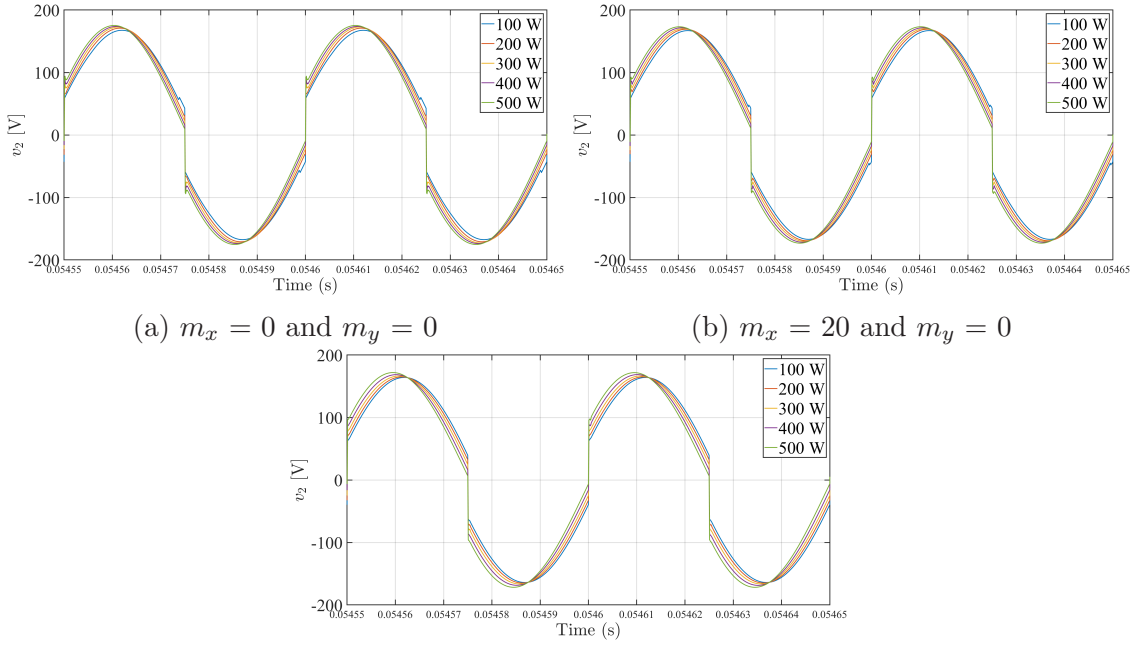

(a) $m_x = 0$ and $m_y = 0$

(b) $m_x = 20$ and $m_y = 0$

(c) $m_x = 50$ and $m_y = 0$

Figure B.1: v_2 waveform representation under charging power variations.

B.1.2 Voltage v_3

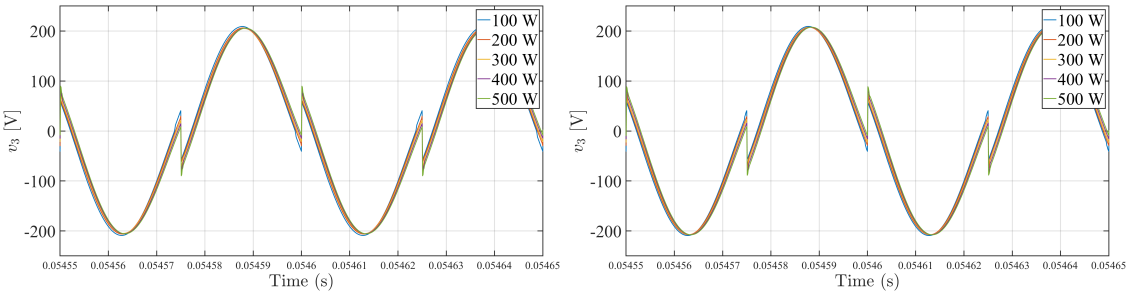

(a) $m_x = 0$ and $m_y = 0$ (b) $m_x = 20$ and $m_y = 0$

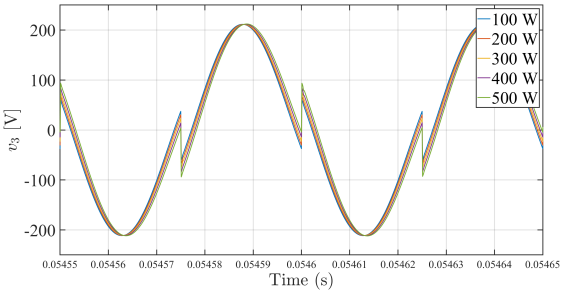

(c) $m_x = 50$ and $m_y = 0$

Figure B.2: v_3 waveform representation under charging power variations.

B.1.3 Current i_{in}

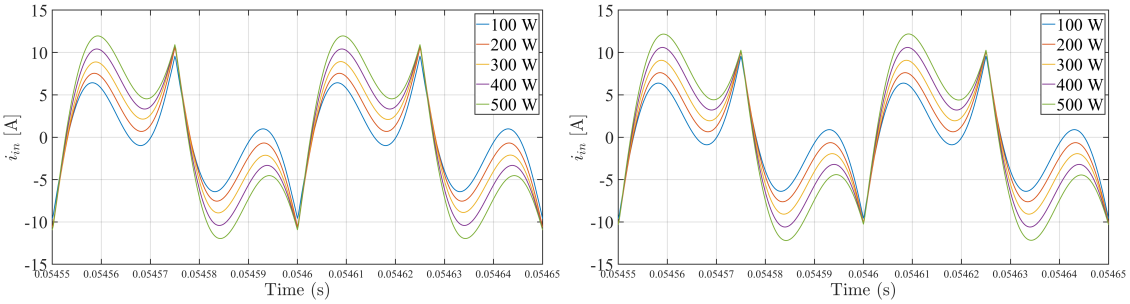

(a) $m_x = 0$ and $m_y = 0$ (b) $m_x = 20$ and $m_y = 0$

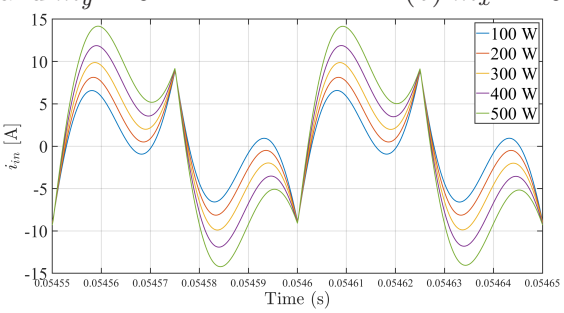

(c) $m_x = 50$ and $m_y = 0$

Figure B.3: i_{in} waveform representation under charging power variations.

B.1.4 Voltage v_4

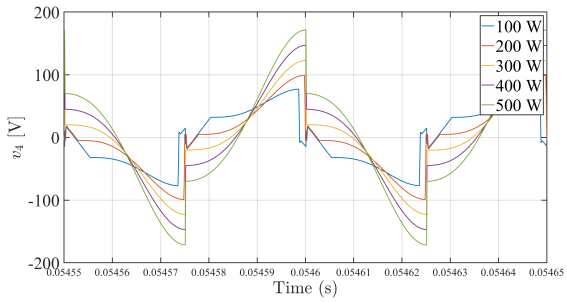

(a) $m_x = 0$ and $m_y = 0$

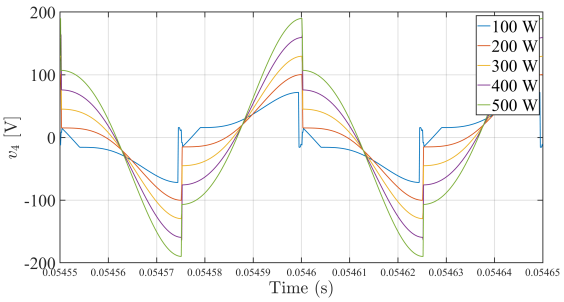

(b) $m_x = 20$ and $m_y = 0$

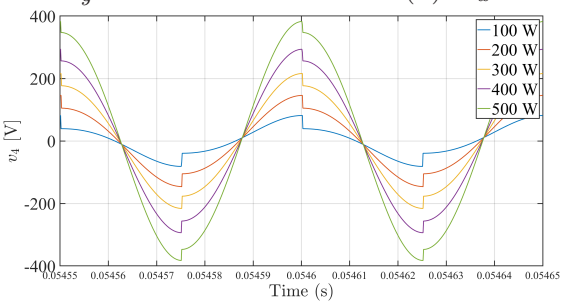

(c) $m_x = 50$ and $m_y = 0$

Figure B.4: v_4 waveform representation under charging power variations.

B.1.5 Current i_{sec}

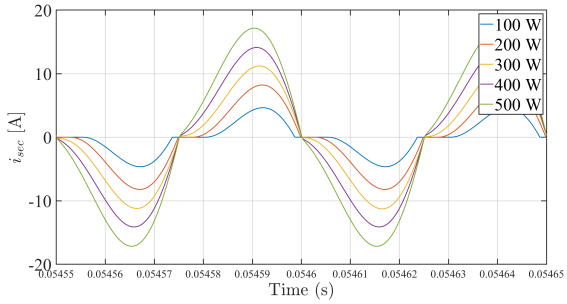

(a) $m_x = 0$ and $m_y = 0$

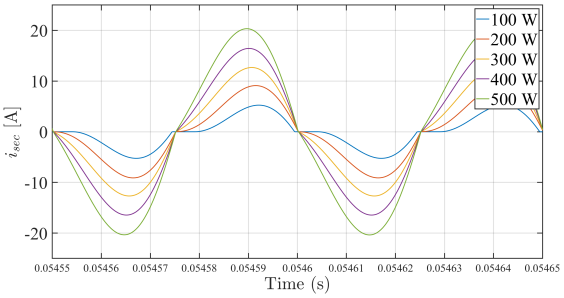

(b) $m_x = 20$ and $m_y = 0$

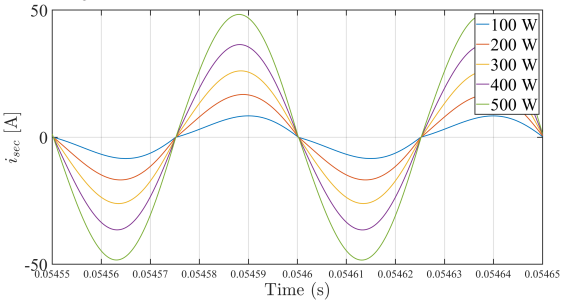

(c) $m_x = 50$ and $m_y = 0$

Figure B.5: i_{sec} waveform representation under charging power variations.

B.2 Amplitude of harmonic components under charging power variations

Moreover, this appendix section will objectively present the tables and respective graphs that referred to both chosen and remain variables.

B.2.1 Voltage v_1

Table B.1: Amplitude (in volt) of the fundamental and higher-order harmonic components of voltage v_1 under charging power variations: $m_x = 0$ and $m_y = 0$

Frequency (Hz)	**500 W**	**1000 W**	**1500 W**	**2000 W**	**2500 W**	**3000 W**
20000	146.90	170.41	205.32	250.44	306.14	375.45
40000	50.91	50.89	50.87	50.85	50.83	50.80
60000	27.03	27.02	27.02	27.02	27.01	27.01
80000	18.74	18.74	18.74	18.74	18.74	18.73
100000	14.41	14.41	14.41	14.40	14.40	14.40
120000	11.72	11.72	11.72	11.72	11.72	11.72
140000	9.89	9.89	9.89	9.89	9.89	9.89
160000	8.55	8.55	8.55	8.55	8.55	8.55

Table B.2: Amplitude (in volt) of the fundamental and higher-order harmonic components of voltage v_1 under charging power variations: $m_x = 20$ and $m_y = 0$

Frequency (Hz)	**500 W**	**1000 W**	**1500 W**	**2000 W**	**2500 W**	**3000 W**
20000	145.02	170.76	210.60	266.23	346.92	392.94
40000	50.66	50.65	50.63	50.61	50.58	50.56
60000	26.99	26.99	26.99	26.98	26.98	26.97
80000	18.73	18.73	18.73	18.72	18.72	18.72
100000	14.40	14.40	14.40	14.40	14.40	14.40
120000	11.72	11.72	11.72	11.72	11.72	11.72
140000	9.89	9.89	9.88	9.88	9.88	9.88
160000	8.55	8.55	8.55	8.55	8.55	8.55

Table B.3: Amplitude (in volt) of the fundamental and higher-order harmonic components of voltage v_1 under charging power variations : $m_x = 50$ and $m_y = 0$

Frequency (Hz)	**500 W**	**1000 W**	**1500 W**	**2000 W**	**2500 W**	**3000 W**
20000	145.62	231.40	231.40	231.40	231.40	231.40
40000	50.29	50.25	50.25	50.25	50.25	50.25
60000	26.94	26.93	26.93	26.93	26.93	26.93
80000	18.71	18.71	18.71	18.71	18.71	18.71
100000	14.39	14.39	14.39	14.39	14.39	14.39
120000	11.71	11.71	11.71	11.71	11.71	11.71
140000	9.88	9.88	9.88	9.88	9.88	9.88
160000	8.55	8.55	8.55	8.55	8.55	8.55

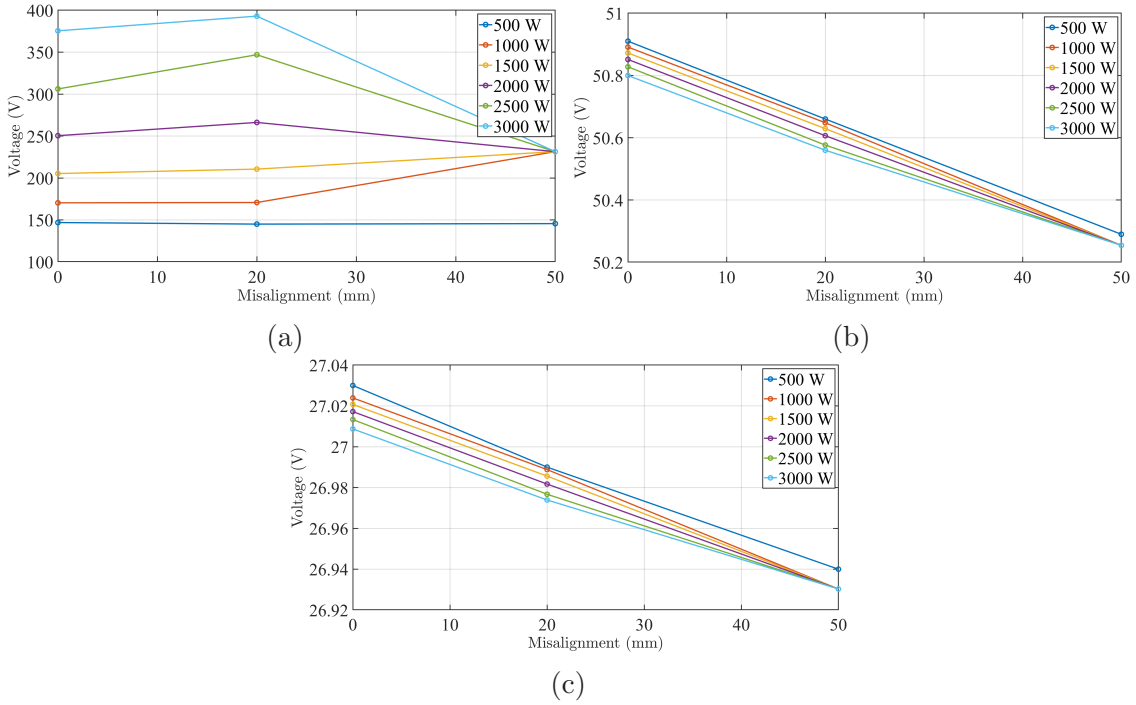

Figure B.6: Amplitude of the fundamental component, third and fifth harmonics of the voltage v_1 under misalignment and charging power variations.

B.2.2 Voltage v_2

Table B.4: Amplitude (in volt) of the fundamental and higher-order harmonic components of voltage v_2 under charging power variations : $m_x = 0$ and $m_y = 0$

Frequency (Hz)	**500 W**	**1000 W**	**1500 W**	**2000 W**	**2500 W**	**3000 W**
20000	186.90	195.74	211.25	234.09	265.28	307.19
40000	19.87	19.95	20.03	20.13	20.23	20.36
60000	11.54	11.58	11.63	11.67	11.73	11.79
80000	8.19	8.21	8.24	8.28	8.31	8.36
100000	6.36	6.38	6.41	6.43	6.46	6.49
120000	5.22	5.23	5.25	5.27	5.29	5.32
140000	4.43	4.45	4.46	4.48	4.49	4.51
160000	3.86	3.87	3.88	3.90	3.91	3.93

Table B.5: Amplitude (in volt) of the fundamental and higher-order harmonic components of voltage v_2 under charging power variations : $m_x = 20$ and $m_y = 0$

Frequency (Hz)	**500 W**	**1000 W**	**1500 W**	**2000 W**	**2500 W**	**3000 W**
20000	185.30	195.13	213.15	242.14	289.23	317.83
40000	21.00	21.07	21.16	21.26	21.40	21.47
60000	12.08	12.12	12.16	12.22	12.29	12.33
80000	8.54	8.57	8.60	8.63	8.68	8.71
100000	6.63	6.65	6.67	6.69	6.73	6.75
120000	5.42	5.44	5.46	5.48	5.51	5.52
140000	4.60	4.61	4.62	4.64	4.66	4.68
160000	3.99	4.00	4.02	4.03	4.05	4.06

Table B.6: Amplitude (in volt) of the fundamental and higher-order harmonic components of voltage v_2 under charging power variations : $m_x = 50$ and $m_y = 0$

Frequency (Hz)	**500 W**	**1000 W**	**1500 W**	**2000 W**	**2500 W**	**3000 W**
20000	183.78	222.39	222.39	222.39	222.39	222.39
40000	22.74	22.89	22.89	22.89	22.89	22.89
60000	12.93	13.01	13.01	13.01	13.01	13.01
80000	9.10	9.16	9.16	9.16	9.16	9.16
100000	7.04	7.09	7.09	7.09	7.09	7.09
120000	5.75	5.78	5.78	5.78	5.78	5.78
140000	4.86	4.89	4.89	4.89	4.89	4.89
160000	4.21	4.24	4.24	4.24	4.24	4.24

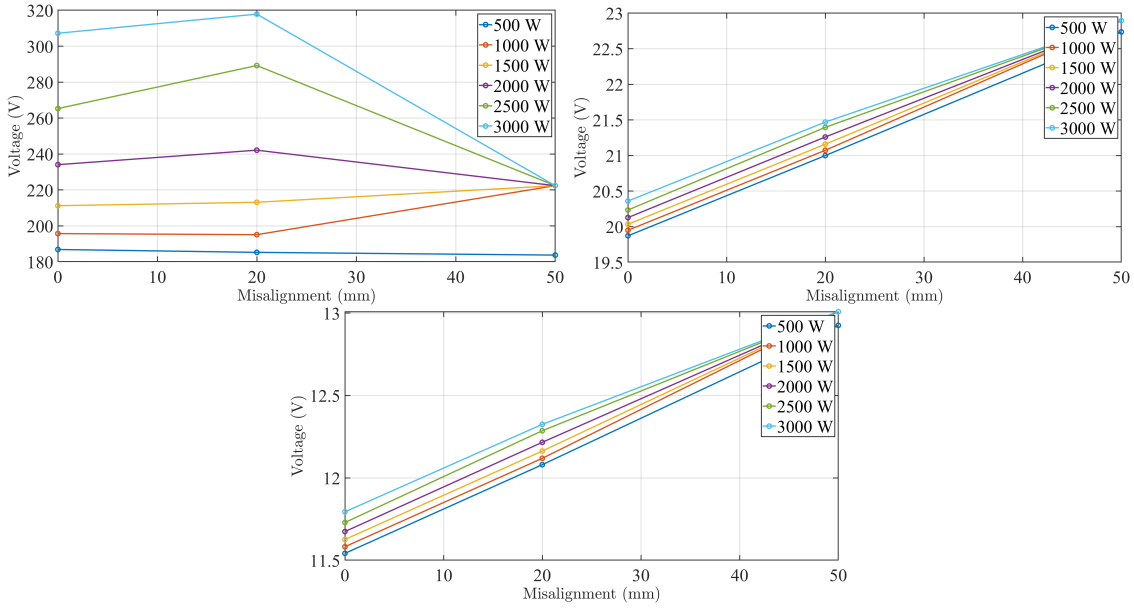

Figure B.7: Amplitude (in volt) of fundamental component, third and fifth harmonics of the voltage v_2 under misalignment and charging power variations.

B.2.3 Voltage v_3

Table B.7: Amplitude (in volt) of the fundamental and higher-order harmonic components of voltage v_3 under charging power variations : $m_x = 0$ and $m_y = 0$

Frequency (Hz)	**500 W**	**1000 W**	**1500 W**	**2000 W**	**2500 W**	**3000 W**
20000	186.98	194.11	208.01	229.44	259.47	300.42
40000	28.04	28.08	28.12	28.16	28.20	28.26
60000	12.93	12.96	13.00	13.04	13.09	13.14
80000	8.66	8.69	8.71	8.74	8.78	8.82
100000	6.58	6.60	6.62	6.643	6.67	6.70
120000	5.34	5.35	5.37	5.39	5.41	5.43
140000	4.50	4.52	4.529	4.544	4.56	4.58
160000	3.91	3.92	3.928	3.940	3.95	3.97

Table B.8: Amplitude (in volt) of the fundamental and higher-order harmonic components of voltage v_3 under charging power variations : $m_x = 20$ and $m_y = 0$

Frequency (Hz)	**500 W**	**1000 W**	**1500 W**	**2000 W**	**2500 W**	**3000 W**
20000	188.78	196.30	212.21	239.18	284.38	312.23
40000	28.54	28.58	28.61	28.66	28.72	28.75
60000	13.37	13.40	13.44	13.48	13.54	13.57
80000	8.98	9.01	9.04	9.07	9.11	9.14
100000	6.83	6.85	6.87	6.89	6.93	6.95
120000	5.53	5.55	5.56	5.58	5.61	5.63
140000	4.66	4.67	4.69	4.70	4.73	4.74
160000	4.04	4.05	4.06	4.07	4.09	4.10

Table B.9: Amplitude (in volt) of the fundamental and higher-order harmonic components of voltage v_3 under charging power variations : $m_x = 50$ and $m_y = 0$

Frequency (Hz)	**500 W**	**1000 W**	**1500 W**	**2000 W**	**2500 W**	**3000 W**
20000	192.94	225.21	225.21	225.21	225.21	225.21
40000	29.32	29.38	29.38	29.38	29.38	29.38
60000	14.06	14.13	14.13	14.13	14.13	14.13
80000	9.50	9.55	9.55	9.55	9.55	9.55
100000	7.22	7.27	7.27	7.27	7.27	7.27
120000	5.85	5.88	5.88	5.88	5.88	5.88
140000	4.92	4.95	4.95	4.95	4.95	4.95
160000	4.25	4.27	4.27	4.27	4.27	4.27

B.2.4 Current i_{in}

Table B.10: Amplitude (in ampere) of the fundamental and higher-order harmonic components of current i_{in} under charging power variations : $m_x = 0$ and $m_y = 0$

Frequency (Hz)	**500 W**	**1000 W**	**1500 W**	**2000 W**	**2500 W**	**3000 W**
20000	10.21	19.10	28.81	39.55	51.72	66.13
40000	4.84	4.83	4.82	4.81	4.79	4.78
60000	1.48	1.48	1.48	1.48	1.47	1.47
80000	0.73	0.73	0.72	0.72	0.72	0.72
100000	0.43	0.43	0.43	0.43	0.43	0.43
120000	0.29	0.29	0.28	0.28	0.28	0.28
140000	0.20	0.20	0.20	0.20	0.20	0.20
160000	0.15	0.15	0.15	0.15	0.15	0.15

Table B.11: Amplitude (in ampere) of the fundamental and higher-order harmonic components of current i_{in} under charging power variations : $m_x = 20$ and $m_y = 0$

Frequency (Hz)	**500 W**	**1000 W**	**1500 W**	**2000 W**	**2500 W**	**3000 W**
20000	10.31	19.70	30.43	43.28	60.39	69.79
40000	4.70	4.69	4.68	4.67	4.65	4.64
60000	1.45	1.45	1.44	1.44	1.44	1.43
80000	0.71	0.71	0.71	0.71	0.71	0.70
100000	0.42	0.42	0.42	0.42	0.42	0.42
120000	0.28	0.28	0.28	0.28	0.28	0.28
140000	0.20	0.20	0.20	0.20	0.20	0.20
160000	0.15	0.15	0.15	0.15	0.15	0.15

Table B.12: Amplitude (in ampere) of the fundamental and higher-order harmonic components of current i_{in} under charging power variations : $m_x = 50$ and $m_y = 0$

Frequency (Hz)	**500 W**	**1000 W**	**1500 W**	**2000 W**	**2500 W**	**3000 W**
20000	12.25	35.91	35.91	35.91	35.91	35.91
40000	4.48	4.46	4.46	4.46	4.46	4.46
60000	1.40	1.39	1.39	1.39	1.39	1.39
80000	0.69	0.69	0.69	0.69	0.69	0.69
100000	0.41	0.41	0.41	0.41	0.41	0.41
120000	0.27	0.27	0.27	0.27	0.27	0.27
140000	0.19	0.19	0.19	0.19	0.19	0.19
160000	0.14	0.14	0.14	0.14	0.14	0.14

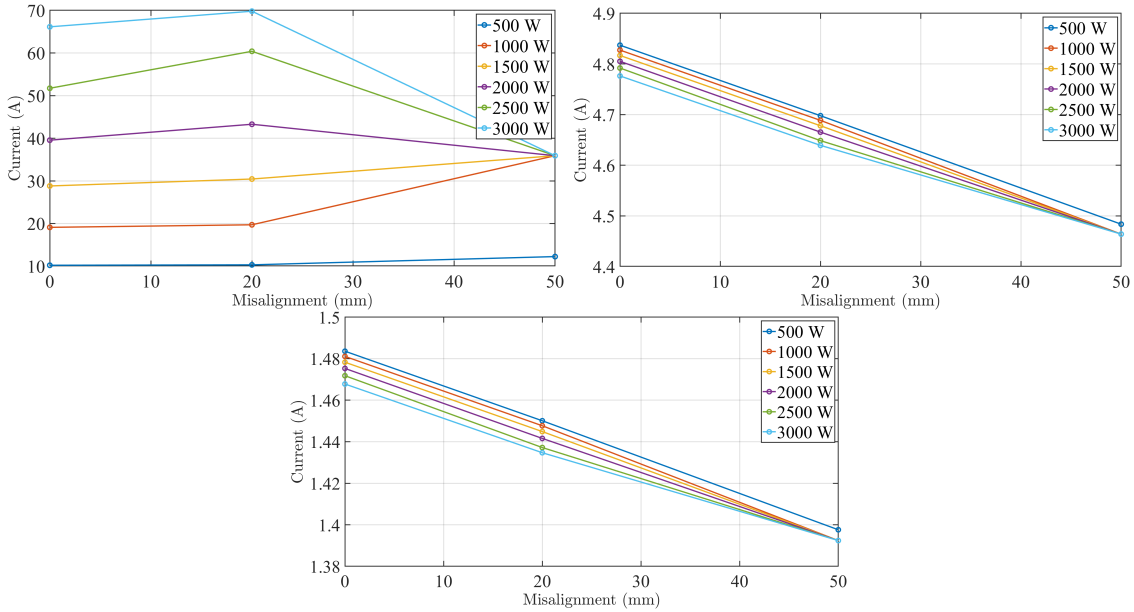

Figure B.8: Amplitude of the fundamental component, third and fifth harmonics of the current i_{in} under misalignment and charging power variations.

B.2.5 Current i_{pri}

Table B.13: Amplitude (in ampere) of the fundamental and higher-order harmonic components of current i_{pri} under charging power variations : $m_x = 0$ and $m_y = 0$

Frequency (Hz)	**500 W**	**1000 W**	**1500 W**	**2000 W**	**2500 W**	**3000 W**
20000	33.20	32.96	32.70	32.41	32.09	31.70
40000	2.22	2.21	2.19	2.18	2.16	2.14
60000	0.63	0.63	0.62	0.62	0.61	0.61
80000	0.30	0.30	0.30	0.30	0.29	0.29
100000	0.18	0.18	0.18	0.17	0.17	0.17
120000	0.12	0.12	0.12	0.11	0.11	0.11
140000	0.08	0.08	0.08	0.08	0.08	0.08
160000	0.06	0.06	0.06	0.06	0.06	0.06

Table B.14: Amplitude (in ampere) of the fundamental and higher-order harmonic components of current i_{pri} under charging power variations : $m_x = 20$ and $m_y = 0$

Frequency (Hz)	**500 W**	**1000 W**	**1500 W**	**2000 W**	**2500 W**	**3000 W**
20000	33.20	32.94	32.66	32.31	31.85	31.60
40000	2.05	2.04	2.02	2.01	1.99	1.97
60000	0.58	0.58	0.58	0.57	0.57	0.56
80000	0.28	0.28	0.28	0.28	0.27	0.27
100000	0.17	0.16	0.16	0.16	0.16	0.16
120000	0.11	0.11	0.11	0.11	0.11	0.11
140000	0.08	0.08	0.08	0.08	0.07	0.07
160000	0.06	0.06	0.06	0.06	0.06	0.06

Table B.15: Amplitude (in ampere) of the fundamental and higher-order harmonic components of current i_{pri} under charging power variations : $m_x = 50$ and $m_y = 0$

Frequency (Hz)	**500 W**	**1000 W**	**1500 W**	**2000 W**	**2500 W**	**3000 W**
20000	33.14	32.51	32.51	32.51	32.51	32.51
40000	1.78	1.76	1.76	1.76	1.76	1.76
60000	0.51	0.51	0.51	0.51	0.51	0.51
80000	0.25	0.24	0.24	0.24	0.24	0.24
100000	0.15	0.14	0.14	0.14	0.14	0.14
120000	0.10	0.10	0.10	0.10	0.10	0.10
140000	0.07	0.07	0.07	0.07	0.07	0.07
160000	0.05	0.05	0.05	0.05	0.05	0.05

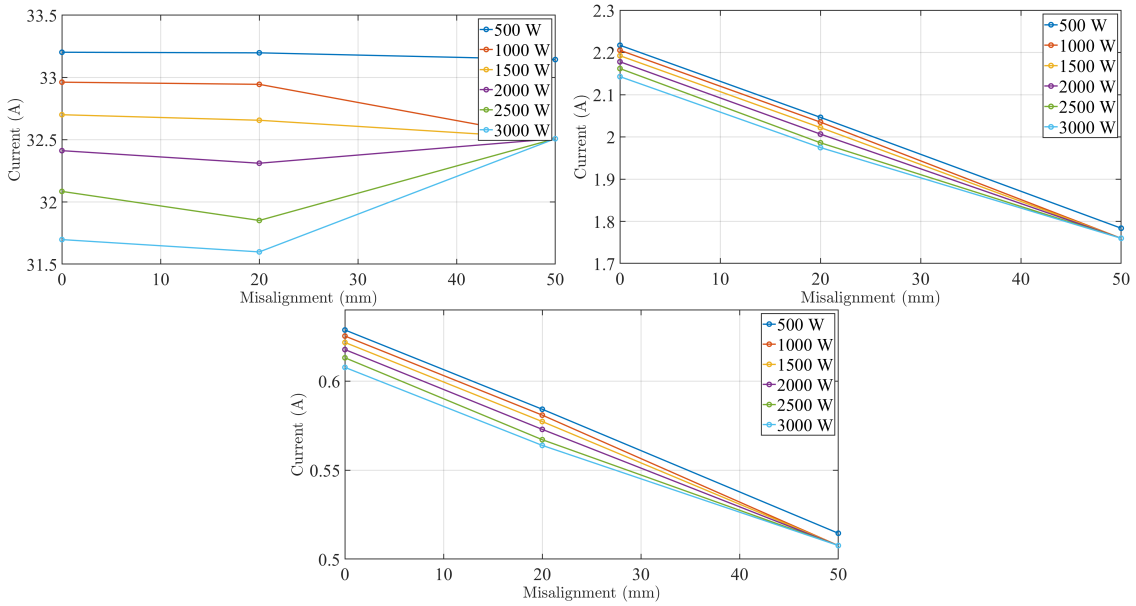

Figure B.9: Amplitude of the fundamental component, third and fifth harmonics of the current i_{pri} under misalignment and charging power variations.

B.2.6 Voltage v_4

Table B.16: Amplitude (in volt) of the fundamental and higher-order harmonic components of voltage v_4 under charging power variations : $m_x = 0$ and $m_y = 0$

Frequency (Hz)	**500 W**	**1000 W**	**1500 W**	**2000 W**	**2500 W**	**3000 W**
20000	127.54	253.60	393.28	548.39	724.50	932.99
40000	25.81	24.97	24.05	23.04	21.89	20.53
60000	13.68	13.22	12.71	12.15	11.52	10.77
80000	9.48	9.16	8.81	8.42	7.97	7.45
100000	7.29	7.04	6.77	6.47	6.12	5.72
120000	5.93	5.73	5.50	5.26	4.98	4.65
140000	5.00	4.83	4.64	4.44	4.20	3.92
160000	4.33	4.18	4.02	3.84	3.63	3.39

Table B.17: Amplitude (in volt) of the fundamental and higher-order harmonic components of voltage v_4 under charging power variations : $m_x = 20$ and $m_y = 0$

Frequency (Hz)	**500 W**	**1000 W**	**1500 W**	**2000 W**	**2500 W**	**3000 W**
20000	151.95	314.42	501.42	725.56	1024.32	1188.48
40000	21.06	20.06	18.93	17.57	15.76	14.77
60000	11.20	10.65	10.02	9.27	8.27	7.72
80000	7.76	7.38	6.94	6.42	5.72	5.33
100000	5.97	5.67	5.33	4.93	4.39	4.09
120000	4.86	4.62	4.34	4.01	3.57	3.33
140000	4.09	3.89	3.66	3.38	3.01	2.81
160000	3.54	3.37	3.17	2.93	2.60	2.43

Table B.18: Amplitude (in volt) of the fundamental and higher-order harmonic components of voltage v_4 under charging power variations : $m_x = 50$ and $m_y = 0$

Frequency (Hz)	**500 W**	**1000 W**	**1500 W**	**2000 W**	**2500 W**	**3000 W**
20000	365.18	1188.30	1188.30	1188.30	1188.30	1188.30
40000	9.00	4.63	4.63	4.63	4.63	4.63
60000	4.78	2.36	2.36	2.36	2.36	2.36
80000	3.31	1.62	1.62	1.62	1.62	1.62
100000	2.55	1.24	1.24	1.24	1.24	1.24
120000	2.07	1.01	1.01	1.01	1.01	1.01
140000	1.74	0.85	0.85	0.85	0.85	0.85
160000	1.51	0.73	0.73	0.73	0.73	0.73

Table B.19: Amplitude (in volt) of the third and fifth harmonics of voltage v_4 under misalignment and charging power variations

	m_x **(mm)**	**500 W**	**1000 W**	**1500 W**	**2000 W**	**2500 W**	**3000 W**
v_4^3	0	25.81	24.97	24.05	23.04	21.89	20.53
	20	21.06	20.06	18.93	17.57	15.76	14.77
	50	9.00	4.63	4.63	4.63	4.63	4.63
v_4^5	0	13.68	13.22	12.71	12.15	11.52	10.77
	20	11.20	10.65	10.02	9.27	8.27	7.72
	50	4.78	2.36	2.36	2.36	2.36	2.36

B.2.7 Voltage v_5

Table B.20: Amplitude (in volt) of the fundamental and higher-order harmonic components of voltage v_5 under charging power variations : $m_x = 0$ and $m_y = 0$

Frequency (Hz)	**500 W**	**1000 W**	**1500 W**	**2000 W**	**2500 W**	**3000 W**
20000	64.45	62.25	59.87	57.23	54.24	50.71
40000	21.48	20.73	19.92	19.03	18.02	16.82
60000	12.89	12.44	11.96	11.42	10.81	10.09
80000	9.21	8.89	8.54	8.16	7.72	7.21
100000	7.16	6.91	6.64	6.35	6.01	5.61
120000	5.86	5.66	5.44	5.19	4.92	4.59
140000	4.96	4.79	4.60	4.40	4.16	3.89
160000	4.30	4.15	3.99	3.81	3.61	3.37

Table B.21: Amplitude (in volt) of the fundamental and higher-order harmonic components of voltage v_5 under charging power variations : $m_x = 20$ and $m_y = 0$

Frequency (Hz)	**500 W**	**1000 W**	**1500 W**	**2000 W**	**2500 W**	**3000 W**
20000	52.81	50.21	47.25	43.71	38.99	36.40
40000	17.59	16.71	15.71	14.51	12.91	12.03
60000	10.55	10.03	9.43	8.70	7.75	7.22
80000	7.54	7.16	6.73	6.22	5.53	5.16
100000	5.86	5.57	5.24	4.84	4.30	4.01
120000	4.80	4.56	4.29	3.96	3.52	3.28
140000	4.06	3.86	3.63	3.35	2.98	2.78
160000	3.52	3.35	3.15	2.91	2.59	2.41

Table B.22: Amplitude (in volt) of the fundamental and higher-order harmonic components of voltage v_5 under charging power variations : $m_x = 50$ and $m_y = 0$

Frequency (Hz)	**500 W**	**1000 W**	**1500 W**	**2000 W**	**2500 W**	**3000 W**
20000	22.61	11.18	11.18	11.18	11.18	11.18
40000	7.51	3.62	3.62	3.62	3.62	3.62
60000	4.50	2.17	2.17	2.17	2.17	2.17
80000	3.22	1.55	1.55	1.55	1.55	1.55
100000	2.50	1.21	1.21	1.21	1.21	1.21
120000	2.04	0.99	0.99	0.99	0.99	0.99
140000	1.73	0.84	0.84	0.84	0.84	0.84
160000	1.50	0.73	0.73	0.73	0.73	0.73

Table B.23: Amplitude of the third and fifth harmonics of voltage v_5 under misalignment and charging power variations

	m_x **(mm)**	**500 W**	**1000 W**	**1500 W**	**2000 W**	**2500 W**	**3000 W**
v_5^{FC}	0	64.45	62.25	59.87	57.23	54.24	50.71
	20	52.81	50.21	47.25	43.71	38.99	36.40
	50	22.61	11.18	11.18	11.18	11.18	11.18
v_5^3	0	21.48	20.73	19.92	19.03	18.02	16.82
	20	17.59	16.71	15.71	14.51	12.91	12.03
	50	7.51	3.62	3.62	3.62	3.62	3.62
v_5^5	0	12.89	12.44	11.96	11.42	10.81	10.09
	20	10.55	10.03	9.43	8.70	7.75	7.22
	50	4.50	2.17	2.17	2.17	2.17	2.17

B.2.8 Current i_{sec}

Table B.24: Amplitude (in ampere) of the fundamental and higher-order harmonic components of current i_{sec} under charging power variations: $m_x = 0$ and $m_y = 0$

Frequency (Hz)	**500 W**	**1000 W**	**1500 W**	**2000 W**	**2500 W**	**3000 W**
20000	16.25	33.23	51.81	72.37	95.68	123.27
40000	1.72	1.68	1.64	1.59	1.53	1.47
60000	0.53	0.51	0.50	0.48	0.47	0.44
80000	0.26	0.25	0.24	0.24	0.23	0.22
100000	0.15	0.15	0.14	0.14	0.13	0.13
120000	0.10	0.1	0.10	0.09	0.09	0.08
140000	4.96	4.79	4.60	4.40	4.16	3.89
160000	4.30	4.15	3.99	3.81	3.61	3.37

Table B.25: Amplitude (in ampere) of the fundamental and higher-order harmonic components of current i_{sec} under charging power variations : $m_x = 20$ and $m_y = 0$

Frequency (Hz)	**500 W**	**1000 W**	**1500 W**	**2000 W**	**2500 W**	**3000 W**
20000	19.79	41.45	66.22	95.87	135.38	157.08
40000	1.37	1.33	1.27	1.21	1.13	1.08
60000	0.42	0.41	0.39	0.37	0.34	0.33
80000	0.21	0.20	0.19	0.18	0.17	0.16
100000	0.12	0.12	0.11	0.11	0.10	0.09
120000	0.08	0.08	0.08	0.07	0.07	0.06
140000	0.06	0.06	0.05	0.05	0.05	0.04
160000	0.04	0.04	0.04	0.04	0.03	0.03

Table B.26: Amplitude (in ampere) of the fundamental and higher-order harmonic components of current i_{sec} under charging power variations : $m_x = 50$ and $m_y = 0$

Frequency (Hz)	**500 W**	**1000 W**	**1500 W**	**2000 W**	**2500 W**	**3000 W**
20000	48.25	157.08	157.08	157.08	157.08	157.08
40000	0.59	0.40	0.40	0.40	0.40	0.40
60000	0.18	0.12	0.12	0.12	0.12	0.12
80000	0.09	0.06	0.06	0.06	0.06	0.06
100000	0.05	0.03	0.03	0.03	0.03	0.03
120000	0.04	0.02	0.02	0.02	0.02	0.02
140000	0.03	0.02	0.02	0.02	0.02	0.02
160000	0.02	0.01	0.01	0.01	0.01	0.01

Table B.27: Amplitude of the 3^{rd} harmonic of current i_{sec} under misalignment and charging power variations

	m_x **(mm)**	**500 W**	**1000 W**	**1500 W**	**2000 W**	**2500 W**	**3000 W**
i^3_{sec}	0	1.72	1.68	1.64	1.59	1.53	1.47
	20	1.37	1.33	1.27	1.21	1.13	1.08
	50	0.59	0.40	0.40	0.40	0.40	0.40

B.2.9 Reactive Power

Table B.28: Amplitude (in volt-amp reactive) of the fundamental and higher-order harmonic components of Reactive Power under charging power variations : $m_x = 0$ and $m_y = 0$

Frequency (Hz)	**500 W**	**1000 W**	**1500 W**	**2000 W**	**2500 W**	**3000 W**
20000	99.36	91.53	83.28	74.50	64.97	54.27
40000	-18.46	-17.41	-16.29	-15.10	-13.81	-12.34
60000	-3.39	-3.19	-2.98	-2.76	-2.51	-2.24
80000	-1.18	-1.11	-1.04	-0.96	-0.88	-0.78
100000	-0.55	-0.51	-0.48	-0.44	-0.40	-0.36
120000	-0.30	-0.28	-0.26	-0.24	-0.22	-0.19
140000	-0.18	-0.17	-0.16	-0.14	-0.13	-0.12
160000	-0.11	-0.11	-0.10	-0.09	-0.08	-0.08

Table B.29: Amplitude (in volt-amp reactive) of the fundamental and higher-order harmonic components of Reactive Power under charging power variations : $m_x = 20$ and $m_y = 0$

Frequency (Hz)	**500 W**	**1000 W**	**1500 W**	**2000 W**	**2500 W**	**3000 W**
20000	69.85	65.16	57.39	48.51	37.36	31.56
40000	-12.08	-11.09	-10.01	-8.79	-7.27	-6.50
60000	-2.23	-2.04	-1.84	-1.61	-1.32	-1.18
80000	-0.78	-0.71	-0.64	-0.56	-0.46	-0.41
100000	-0.36	-0.33	-0.30	-0.26	-0.21	-0.19
120000	-0.20	-0.18	-0.16	-0.14	-0.12	-0.10
140000	-0.12	-0.11	-0.10	-0.08	-0.07	-0.06
160000	-0.08	-0.07	-0.06	-0.05	-0.04	-0.04

Table B.30: Amplitude (in volt-amp reactive) of the fundamental and higher-order harmonic components of Reactive Power under charging power variations : $m_x = 50$ and $m_y = 0$

Frequency (Hz)	**500 W**	**1000 W**	**1500 W**	**2000 W**	**2500 W**	**3000 W**
20000	12.29	4.26	4.26	4.26	4.26	4.26
40000	-2.22	-0.72	-0.72	-0.72	-0.72	-0.72
60000	-0.41	-0.13	-0.13	-0.13	-0.13	-0.13
80000	-0.14	-0.04	-0.04	-0.04	-0.04	-0.04
100000	-0.07	-0.02	-0.02	-0.02	-0.02	-0.02
120000	-0.04	-0.01	-0.01	-0.01	-0.01	-0.01
140000	-0.02	-0.01	-0.01	-0.01	-0.01	-0.01
160000	-0.01	0.00	0.00	0.00	0.00	0.00

Table B.31: Amplitude of 3^{rd} harmonic of reactive power under misalignment and charging power variations

	m_x **(mm)**	**500 W**	**1000 W**	**1500 W**	**2000 W**	**2500 W**	**3000 W**
Q^3	0	-18.46	-17.41	-16.29	-15.10	-13.81	-12.34
	20	-12.09	-11.09	-10.01	-8.79	-7.27	-6.50
	50	-2.24	-0.72	-0.72	-0.72	-0.72	-0.72